ADVANCED CHARGE STORAGE MATERIALS FOR SUPERCAPACITOR APPLICATIONS

ADVANCED CHARGE STORAGE MATERIALS FOR SUPERCAPACITOR APPLICATIONS

By ASEEB MOHAMMUD SYED, B. Eng.

A Thesis Submitted to the School of Graduate Studies in Partial Fulfillment of the Requirements
for the Degree of Master of Applied Science

McMaster University © Copyright by Aseeb M. Syed. April 2019

MASTER OF APPLIED SCIENCE (2019) McMaster University
Department of Materials Science & Engineering Hamilton, Ontario

TITLE: Advanced Materials for Supercapacitor Applications
AUTHOR: Aseeb M. Syed. B.Eng (McMaster University)
SUPERVISOR: Professor Igor Zhitomirsky
NUMBER OF PAGES: 86

LAY ABSTRACT

Supercapacitors (SCs) and batteries are both electrochemical energy storage devices. While batteries excel at storing energy in high volumes, supercapacitors excel in charging (and discharging) at extremely high rates. It is desirable to obtain the best of both worlds in a single device; high energy volume and fast charging speeds. Although such a feat is not out of the realm of theoretical possibility, current projections forecast supercapacitors to compliment battery technologies instead of replacing them. Nonetheless, constant progression in the field of SCs is needed to sustain and proliferate their adoption into emerging markets. Therefore, the aim of this research was to assist in the endeavours to improve current SC technologies from a materials science standpoint.

ABSTRACT

MnO_2 continues to gain traction in the research and development of advanced supercapacitor materials due to its arsenal of advantages, such as high capacitance, low cost, natural abundance, and environmental benignity. However, its low conductivity has hindered its adoption into real-life applications. Compositing MnO_2 with conductive additives has proved to be a promising route for the improvement of its power-energy characteristics. Four novel colloidal techniques were developed for the synthesis of MnO_2-CNT composites with enhanced performance at high active mass loading. One strategy utilized a Schiff-based linkage of dispersants such as 3,4-Dihydroxybenzaldehyde (DHB) and Toluidine Blue O (TDB) to effectively mix and disperse MnO_2 and CNT. Secondly, a co-dispersion technique was also investigated using Gallocyanine to improve dispersion and mixing of MnO_2 and MWCNT. Third, a novel liquid-liquid extraction technique opened new avenues in agglomerate-free processing of individual components, which allowed enhanced electrode performance. Lastly, a morphology-modification strategy was also undertaken by synthesizing MnO_2 nanorods with the use of advanced organic dispersants to control the aspect ratio and composite nanorods with MWCNT.

The second major material investigated was polypyrrole (PPy), a polymer material with high conductivity, ease of synthesis, low-cost, and non-toxicity. However, its low cyclic stability was prevented it from being applied for real-world applications. Certain anionic and aromatic dopants have shown to improve the conductivity and cyclic stability. Therefore, one of the investigations in this work attempted to improve the performance of PPy-CNT composites by use of a novel anionic dopant, Sunset Yellow (SY). For all investigations electrodes with high mass loadings were produced to achieve high areal capacitance, thus ensuring practicality of the techniques.

ACKNOWLEDGMENTS

النَّاسَ يَشْكُرُ لاَ مَنْ اللَّهَ يَشْكُرُ لاَ

Translation: "He who has not thanked the people has not thanked Allah (God)."

-The Prophet Muhammad (peace and blessings be upon him)

The cherished memories and the valuable experience I take away with me would have only been so because of the people who assisted me through this endeavour.

I begin by thanking my mother who has been there since Day 1 of my entrance into this world. Mummy, the hardships and sacrifices I've put you through can be only be truly recognized by Allah and I pray you are rewarded for every iota of effort.

I thank my father who taught me what duty and responsibility meant. Daddy, you were the first teacher and role-model in my childhood. May you be rewarded for the sacrifices and hardships you went through to support your family through everything.

Nashrah, my little sister, thank you for being there as my sweet assistant (and my partner in crime).

To my professor, thank you dearly for your unparalleled patience and for overlooking all the times I inconvenienced with my inept skill and inadequacies (I know there were many times). You are perhaps the most underrated professor in the entire MSE department, and I know all your other students would agree.

To my former and current lab mates: Mustafa Ata, Cameron Wallar, Haoyu Fan, Ri Chen, Ryan Poon, Jordan Milne, Sadman Sakib, and Amanda Clifford. I thank each and every one of you for making my days in the lab lively and teaching me your unique lab tips and tricks. I pray you are all incredibly successful in your careers and have prosperous lives ahead of you.

Victoria Jarvis, thank you for sharing your amazing expertise with XRD with tact and patience.

Marcia Reid, thank you as well for teaching me all the bells and whistles on the TEM. Your amazing skill at teaching it made it my favourite instrument to use for characterization.

Lastly, to my dearest fiancé. Had I not even gained an atom's worth of knowledge out of my master's degree and had only met you, it still would've been worth it. Ten times over.

TABLE OF FIGURES

LIST OF ABBREVIATIONS

EDL	Electrical Double Layer
μF	Microfarads
PAN	Polyacrylonitrile
AC	Activated carbon
CNT	Carbon nanotube
CP	Conducting polymer
MWCNT	Multi-walled carbon nanotube
ESR	Electrochemical series resistance
SSE	Solid state electrolytes
IL	Ionic liquids
ESW	Electrochemical stability window
PVB	Poly(vinyl butyral-covinyl alcohol-co-vinyl acetate
APS	Aluminum persulfate
I_{pc}	Peak height current
EIS	Electrochemical impedance spectroscopy
DHB	3,4-dihydrobenzaldehyde
mfps	Mussel foot proteins
TDB	Toluidine Blue O
DOPA-HCl	Dopamine hydrochloride
FDS	4-Formylbenzene-1,3-disulfonic acid disodium salt hydrate
GC	Gallocyanine
LLE	Liquid-liquid extraction
PELLI	Particle extraction through liquid-liquid interface
HDPA	Hexadecylphosphonic acid
TDA	Tetradecylamine
ODPA	Octadecylphosphonic acid
OHA	Octanohydroxamic acid
CTAB	Cetyltrimethylammonium bromide
SDS	Sodium dodecyl sulfate
LG	Lauryl Gallate
PVB	Pyrocatechol violet
ECR	Eriochrome cyanine
AF	Acid fuchsin
SY	Sunset yellow

TABLE OF CONTENTS

DECLARATION OF ACADEMIC ACHIEVMENT

I, Aseeb Mohammud Syed, declare that the contents of this research were compiled by myself under the supervision of Dr. Igor Zhitomirsky. All research was conducted with his assistance and guidance during the period of May 2017 to April 2019.

The explanation of some theoretical concepts in this research were explained by Dr. Igor Zhitomirsky, Ryan Poon, Mustafa Ata, Ri Chen, Cameron J. Waller, and Haoyu Fan. I received training and technical assistance with TEM imaging by the expertise of Marcia Reid of the Electron Microscopy Facility. For XRD data, I received training and technical assistance by the expertise of Victoria Jarvis of the McMaster Analytical X-Ray Diffraction Facility.

A portion of this research was largely covered in one paper, published in a peer-reviewed journal, with another portion covered in a second paper submitted for publication:

A. M. Syed and I. Zhitomirsky, "New Methods for the Fabrication of Composites for Supercapacitor Electrodes with High Active Mass Loading," *MRS Adv.*, vol. 3, no. 54, pp. 3221–3226, ed 2018. I was also a co-author for the following papers:

A. M. Syed, Z.Z. Wang, and I. Zhitomirsky, "Extractor-free phase transfer of inorganic particles and application for supercapacitors", Materials Letters. (submitted).

I was also the co-author for two other papers which have also been published in peer-reviewed journals:

R. M. E. Silva, R. Poon, J. Milne, A. Syed, and I. Zhitomirsky, "New developments in liquid-liquid extraction, surface modification and agglomerate-free processing of inorganic particles," Adv. Colloid Interface Sci., vol. 261, pp. 15–27, Nov. 2018.

M. S. Ata, R. Poon, A. M. Syed, J. Milne, and I. Zhitomirsky, “New developments in non-covalent surface modification, dispersion and electrophoretic deposition of carbon nanotubes,” Carbon, vol. 130, pp. 584–598, Apr. 2018.

1 Introduction

Engineers and scientists constantly look to the natural world for technological inspiration. The behaviours and structures of plants and animals, as well as the human body are constantly mimicked to reach new technological heights. For example, creatine phosphate is a high-energy compound found in our cells that can rapidly mobilize to help fuel short, explosive efforts. Imagine if we could construct a technological device which could also perform the same function. Well, fortunately, there does exist such a device.

Electrochemical supercapacitors (ESs) are an exciting new field of electrochemical energy storage devices which are facilitating the demand for high-power applications. Their advent has led to applications in start-stop systems, regenerative energy systems, back-up energy for power grids, uninterruptible power systems, and a variety of other applications [1– 2].

In a recent outlook report done by Research and Markets, the supercapacitor market was valued at nearly $850 million in 2017 and is forecasted to hit nearly $5 billion by 2026 [2]. Most of this growth is expected to come from the automotive industry due to the 'electrification' of vehicles. However, the high prices of raw materials and cheaper alternative energy storage devices are hampering the growth of the SC market. Nevertheless, the proliferation of SC technology in automotive applications is expected to bring down manufacturing costs and thus, ease their adoption into other industrial sectors. However, with this drive for SC technology adoption comes the need for constant innovations: from developments of new electrode materials, electrolytes, to novel current collectors and designs – all are being made to facilitate the entrance of SC technology into the industry. This work will primarily deal with electrode materials and their modifications through various colloidal processing techniques.

The three categories of electrode materials for SCs are 1) transition metal oxides 2) polymers and 3) carbon-based materials. Manganese dioxide is one transition metal oxide which has gathered increasing attention due to its natural abundance, low cost, high theoretical capacitance, and environmental benignity [3]. However, its crystal structure, conductivity, and morphology are equally important factors to consider. Each of these factors alone have spawned intensive investigations in attempts to reach optimal performance values.

A polymer material which is also gaining traction is polypyrrole (PPy) for its thermal and environmental stability, high conductivity, ease of synthesis, low-cost, non-toxicity, and flexibility [4]. A potential application which is in-line with current technological forecasts is its applicability in wearable devices [5]. However, a major drawback of PPy is its lackluster cyclic stability. Upon cycling there is volume change which can lead to fatal degradation of the material. Efforts are being made in compositing hierarchical structures with PPy to reduce this effect.

Both MnO_2 and PPy will be comprehensively discussed in the literature review section of this paper. For now, it suffices to say that exploration into these materials will allow fellow researchers to better understand them and open the doors to integrating them into future applications.

2 A Brief History

Before delving into the fundamentals of supercapacitors it would be prudent to first understand the history and fundamental theory of conventional capacitors. The Leyden jar is widely considered to be the first working capacitor and was even used in early designs of the Wimhurst machine [6]. Originally invented by both Pieter van Musschenbroek and Ewald Georg von Kleist (individually) in 1745 the Leyden jar was a simple device used to gather and store electric charges. Figure 1 illustrates a schematic of its construction. The inner and outer surfaces of a glass bottle are wrapped with tin foil, and a metal rod in contact with the inner foil (via a length of wire) protrudes out of the opening of the glass jar. When the external knob is charged positive charges gather on one tin foil piece and negative charges on the other. These charges hold each other in equilibrium until the circuit is closed, upon which a spark is observed. Benjamin Franklin worked with the Leyden Jar for his experiments on electricity and discovered that flat pieces of glass also worked like the jar model. Years later, Michael Faraday made the first practical use of the Leyden jar by storing unused electricity from his experiments.

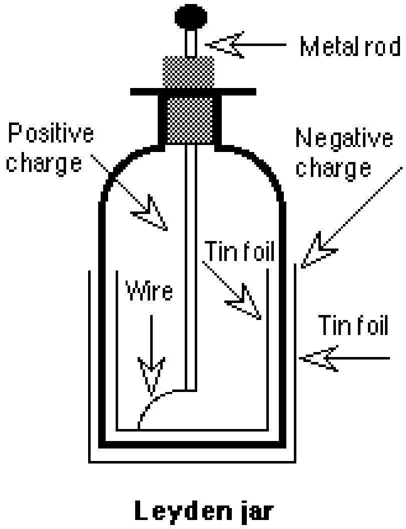

Figure 1. A schematic of a typical Leyden Jar.

The term “capacitor” was first used by Alessandro Volta in 1782, referencing the device's ability to store a higher density of electric charge relative to a normal isolated conductor. Due to confusion among scientists there was a need to harmonize the nomenclature of electrical components. Thus, the term "capacitor" was officially coined and neatly fell in line with "resistor" and "inductor." Not surprisingly, its value came to be called "capacitance".

3 Literature Review

3.1 Capacitors, Batteries, and Supercapacitors

Conventional capacitors are comprised of two conducting plates separated by an insulating dielectric material. Upon the application of an external voltage, positive charges accumulate on one electrode and negative charges on the other. Upon removing the potential, the charges are kept separate by the dielectric material and an inter-electrode potential remains.

The ratio of the stored charge to the potential between the electrodes is termed the capacitance and is in units of Farads (F). Capacitance can also be understood as a quantity reliant upon several factors: the distance D between the electrode plates, the surface area A of the plates, and the permittivity $\varepsilon_0\varepsilon_r$ of the dielectric material. The capacitance is linked to these factors by Equation 1:

$$C = \varepsilon_0\varepsilon_r\frac{A}{D} \qquad \text{Equation 1}$$

The product of the two constants on the right-hand side of Equation 1 gives the permittivity of the dielectric material. Permittivity can be thought of as the ability of a material to "resist" an electric field. Inserting a dielectric material with a high permittivity would prevent opposite charges from coming into contact and thus result in more charge stored on the electrodes. Dielectrics with high permittivity possess a high breakdown voltage – the minimum voltage required to cause a portion of the dielectric to become electrically conductive. This sets a limit on how much voltage one can apply to the capacitor and how much energy may be stored in the capacitor.

The energy stored in a capacitor can be quantitatively understood by taking the integral of Equation 2, where V is the potential across the capacitor plates and dq is an infinitesimal charge that is carried across the plates. The sum of all the "works" that move all infinitesimal charges yields the total energy stored in the capacitor.

$$dW = Vdq \qquad \text{Equation 2}$$

However, a complication arises from the fact that the voltage across the plates is a function of charge. (With each addition of elemental dq the required voltage would need to be increased to oppose the built-in potential.) Therefore, Equation 2 can be rewritten as Equation 3:

$$dW = \frac{q\,dq}{C} \qquad \text{Equation 3}$$

Taking the integral of Equation 3 yields Equation 4, where Q is the total accumulated charge:

$$W(Q) = \int_0^Q \frac{q\,dQ}{C} = \frac{Q^2}{2C} \qquad \text{Equation 4}$$

Since capacitance is simply charge, Q, divided by potential, V, Equation 4 may be rewritten (Equation 5):

$$W = \frac{Q^2}{2C} = \frac{QV}{2} = \frac{CV^2}{2} \qquad \text{Equation 5}$$

The maximum power of a supercapacitor can also be derived by considering the voltage drop across the capacitor's own internal resistance. The derivation yields Equation 6:

$$P_{max} = \frac{V_{max}^2}{4R_{internal}} \qquad \text{Equation 6}$$

Equation 5 and Equation 6 show that improving the energy and power characteristics fundamentally requires either increasing the capacitance, increasing the voltage window, or decreasing the internal resistance.

Two key attributes of any electrochemical energy storage device are the power density and the energy density. These densities may be calculated using either *quantity per unit mass* or *quantity per unit volume*. Figure 2 showcases a Ragone plot which is a plot that compares the energy and power density performances of various energy-storage devices. Capacitors are fundamentally energy storage devices. However, unlike batteries they do not have significant latency during charge and discharge cycles (which gives them their increased power density values). This can be attributed to the fact that the energy storage mechanism of batteries and ESs are intrinsically different. For batteries, chemical inter-conversions of the electrode material occur with accompanying phase changes. These phase changes are responsible for the reduced recyclability of batteries. In contrast, supercapacitors do not undergo substantial phase changes during operation. Instead, they only exhibit state changes and electron transfers granting them higher power density values.

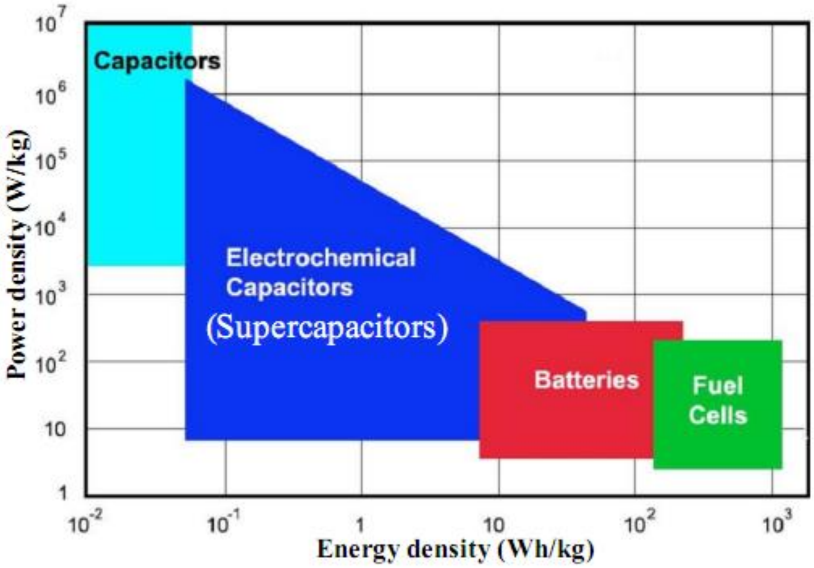

Figure 2. Ragone plotting. Source: Ref. [7]

3.2 The Electrical Double Layer

Typical energy densities of ESs are characteristically higher than that of conventional capacitors due to their exploitation of the electrical double layer (EDL). ESs consist of two electrodes separated by an electrolyte. Upon the application of a potential, ions in the electrolyte solution accumulate at the surface of the charged electrode leading to the formation of an EDL. Since this is a surface-restricted phenomenon the charges stored via this mechanism are largely due from the surface area of the electrode in contact with the electrolyte. Furthermore, double layer capacitance occurs purely through electrostatic forces which allow for high power density values.

The simple yet innovative concept of the EDL allows for the multi-fold increase in the capacitance from the conventional to the supercapacitor type. As seen in Figure 3, the electrical

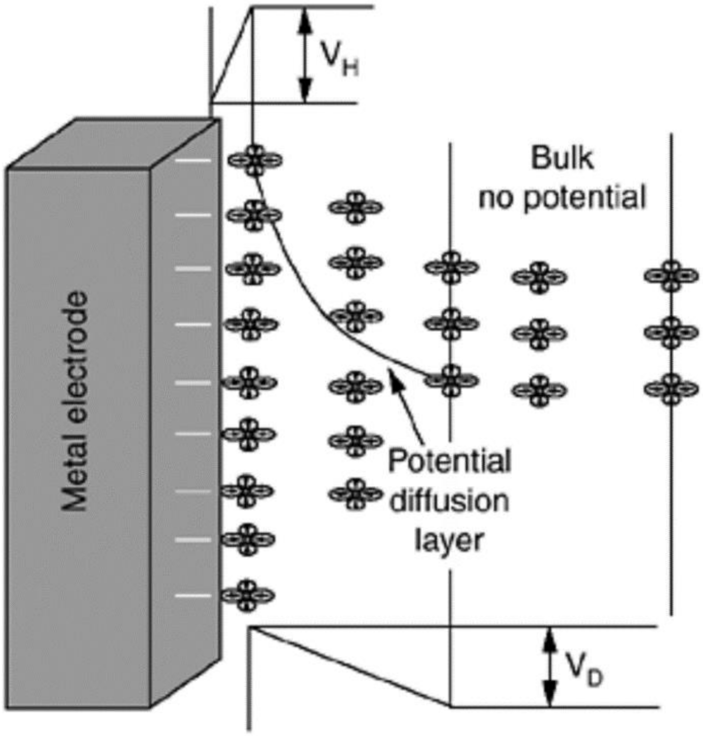

Figure 3. Immersion of a metal electrode into an aqueous media giving rise to the Helmholtz and Gouy-Chapman potentials. Source: Ref. [8]

double layer is established by inserting a metal electrode into an electrolyte solution of solvated cations and anions. Upon submersion, the electrons within the metal migrate towards the surface due to the detection of solvated species in the electrolyte solution. This leads to the disruption in the neutrality of the solution. The first molecules to migrate from the electrolyte are the water molecules which form an H_2O plane adjacent to the surface of the electrode. Thereafter, a plane of solvated cations forms next to the H_2O plane giving rise to the Helmholtz potential, V_H (from charge separation of electrons and cations). Subsequently, the high concentration of solvated cations leads to a concentration gradient extending into the bulk of the solution giving rise to the Gouy-Chapman potential, V_D. Both, V_D and V_H result in capacitances C_D and C_H, respectively. The magnitude of the double-layer capacitance is given by the approximation in Equation 7 where C is the capacitance of the double layer, ε is the dielectric constant of the electrolyte, δ is the distance from the surface of the electrode to the center of the solvated cations, and dS is an elemental surface area term. The magnitude of the capacitance formed from this double layer can be on the order of microfarads (μF) – a substantial increase from conventional capacitors which typically range between picofarads and nanofarads. Moreover, if high surface area materials are used (e.g. carbon-based materials (1000 m^2/g)), then the gravimetric capacitance can reach upwards of 1000 F/g.

$$C = \frac{\varepsilon}{4\pi\delta}\int dS \qquad \text{Equation 7}$$

3.3 Pseudocapacitance

In addition to the double layer capacitance, supercapacitors can also exhibit pseudocapacitance through the application of an active material layer onto the electrode surface.

This active material layer can undergo fast, reversible faradaic reactions which allows for a substantial increase in capacitance through the reaction [9]:

$$M^{n+} + S + ne^- \leftrightarrow SM \qquad \text{Equation 8}$$

where M is a metal species and S is a surface lattice site. Alternatively, the adsorbed ionic species on the electrode surface may also experience redox reactions through the following reaction:

$$Adsorbed\ species + \ ne^- \leftrightarrow Reduced\ species \qquad \text{Equation 9}$$

The reactions seen in Equation 8 and Equation 9 demonstrate the effect of negative charges accumulating on the electrode surface due to the flow of electrons. It is important to note that the reactions from the active material must be reversible; there can be no degradation of either reactant or product, as this is what fundamentally distinguishes pseudocapacitive behaviour from that of batteries.

3.3 Manganese Dioxide

There has been growing interest in utilizing transition metal oxides for supercapacitor materials [10]. Ruthenium oxides (RuO_2), although widely considered as the "gold standard" for supercapacitors, are restricted for high-end applications (e.g., space applications) due to their high cost and toxicity. However, a cheaper and environmentally friendly alternative exists: MnO_2. As mentioned previously, it exhibits high theoretical capacitance (1370 F g^{-1}), low toxicity, low cost, and natural abundance. Both RuO_2 and MnO_2 are observed to utilize the solid-state diffusion mechanism. However, for the case of MnO_2 only a fraction of the material is measured to be electroactive for a given electrode, which is to say that diffusion of bulk cations may not be as fast as is seen in RuO_2. This observation leads to the assumption that only the surface layer of

MnO_2 is responsible for the charge storage. However, there is currently no consensus among researchers on exactly what charge-storage process takes place. The III/IV oxidation state change is what fundamentally leads to the charge storage, but there are two proposed mechanisms as how to this takes place. The first is the *intercalation* mechanism [11] seen in Equation 10 and Equation 11:

$$MnO_2 + H^+ + e^- \leftrightarrow MnOOH \qquad \text{Equation 10}$$

or

$$MnO_2 + C^+ + e^- \leftrightarrow MnOOC \qquad \text{Equation 11}$$

where protons (H^+) or alkali metal cations (C^+) intercalate upon oxidation and deintercalate upon reduction. The second mechanism [12] is based on the *surface adsorption* of electrolyte cations, as seen in Equation 12:

$$(MnO_2)_{surface} + C^+ + e^- \leftrightarrow MnO_2^- C^+ \qquad \text{Equation 12}$$

where C^+ can be an alkali metal cation such as, H^+, Li^+, and $K^=$. Aside from the charge storage mechanisms the performance of MnO_2-based electrodes is dependant on a multitude of factors such as, morphology, crystal structure, and conductivity. These factors will be discussed in the following sections.

3.3.1 Crystal Structure

MnO_2 possesses several crystal structures such as, α, β, γ, δ, and λ-MnO_2. Figure 4 illustrates each of these crystal structures. The distinguishing attribute of these crystal structures is their unique tunnel structures. Brousse et. al [13] were the first to report the size of the tunnel to be deterministic of the capacitance of MnO_2. They discovered that 1D α -MnO_2 (4.6 A) and 2D δ-MnO2 (7 A) tunnel sizes were suitable for rapid insertion of hydrated K^+ cations (3 A),

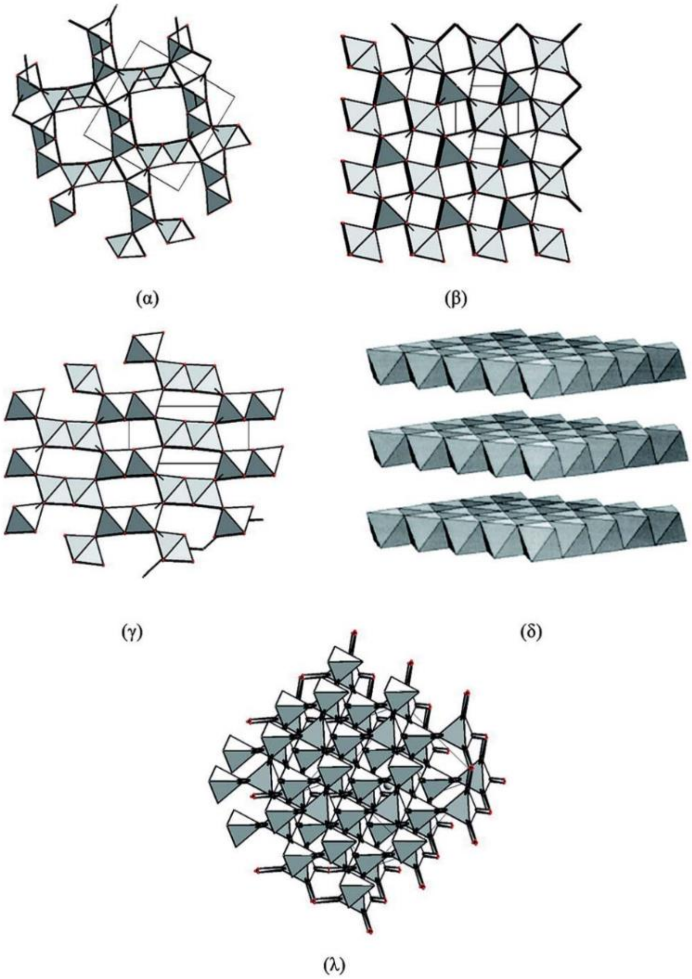

Figure 4. Crystal structures of α, β, γ, δ, and λ-MnO_2. Source: Ref. [14]

which gave way to relatively high capacitance values of 110 F g^{-1}. However, 1D tunnel structures of λ and β -MnO_2 provided only a surface pseudocapacitance of 110 μF cm^{-2}. This can be explained by the fact that their tunnel sizes are smaller than the hydrated K^+ cations, thus limiting the diffusion process. The 3D tunnel structures of λ-MnO_2 offered partial cationic diffusion, exhibiting some intermediate behavior between 2D birnessite and 1D tunnel structures. The results of their investigations suggest that the more "open" the structure the more easily an alkali cation can insert/de-insert into the crystal structure. Munichandraiah et. al. [14] also confirmed that the specific capacitance measured for MnO_2 electrodes is highly dependant on the crystallographic structure and, in fact, decreases in the following order: $\alpha = \delta > \gamma > \lambda > \beta$.

However, there are unique cases in which a larger tunnel size may be detrimental to the pseudocapacitive performance, as seen in the case of solvated Ni ions inside Ni-todorokite – a structure which possesses a relatively large tunneling structure [15]. In this situation, what is expected is a high specific capacitance due to the large 3x3 channel size. However, due to the high stability of solvated Ni ions inside the channel, ionic diffusion is hindered through the cage. This implies that the crystal structure is not solely indicative of high capacitance. Rather, it is important to optimize the interplay between ionic and electronic conductivities alongside the crystal structure itself.

3.3.2 Morphology

The morphology of the material can also have a correspondence with the specific capacitance. Different morphologies yield different surface areas, area-to-volume ratios, and aspect ratios. Specific surface area values can range between 20 to more than 200 $m^2 g^{-1}$ thus creating a substantial difference in capacitive performance across morphology-types. Researchers have been able to develop unique morphologies for MnO_2 such as, nanorods, nanowires, nanobelts, nanotubes, nano-urchins, nanospheres, and thin films [3]. Nanorods and nanowires (Figure 5) are one-dimensional morphologies and allow for short diffusion lengths for ion and electron transfer. Wu et. al [16] synthesized nanorods and nanowires with diameters of 15-35 nm and 8-16 nm, respectively. Electrochemical results showed that the nanowires displayed a higher specific capacitance (350 F g^{-1}) compared to the nanorods (243 F g^{-1}). They attributed these results to the fact that the nanowires had smaller diameters thus allowing for a larger number of active sites and shorter diffusion lengths.

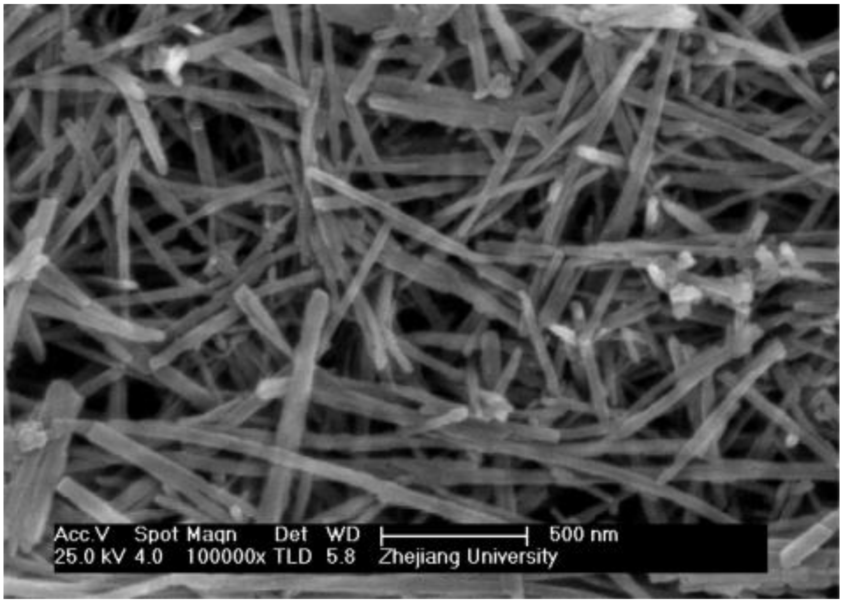

Figure 5. SEM image of pure MnO_2 nanowires. Source: Ref. [17]

Other morphology types include MnO_2 nanotubes and nanobelts (Figure 6) [18–19]. In addition to offering high surface area and short, conductive pathways for ions these morphologies can also accommodate large volume changes during charge-discharge cycles, thereby allowing for greater electrode stability. For their nanobelt electrodes, Li et. al [19] reported 91.3% retention after 5000 cycles while Huang et. al [18] reported 90.4% retention after

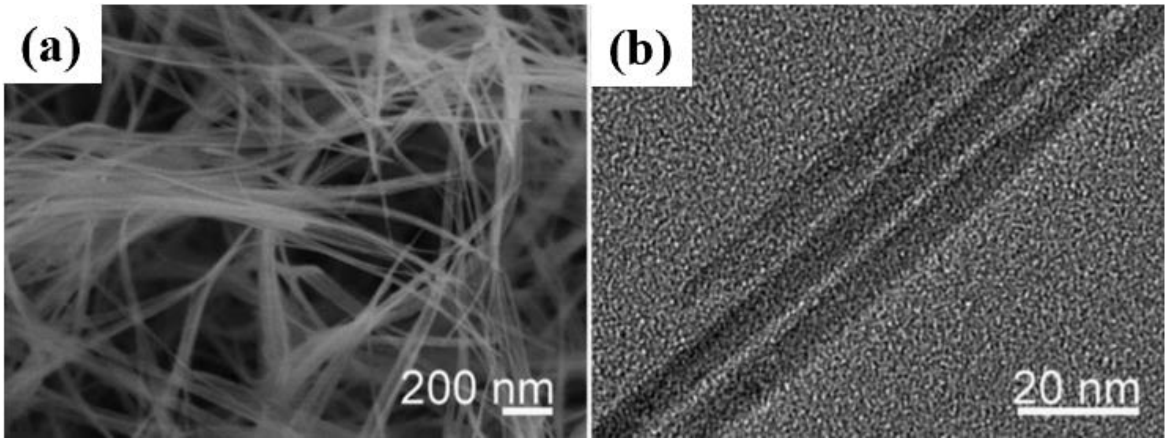

Figure 6. (a) SEM image of MnO_2 nanobelts (b) TEM image. Source: Ref. [19]

3000 cycles for their nanotube-based electrodes.

Xu et. al [20] were able to synthesize α-MnO_2 nanospheres and nano-urchins (Figure 7) via a hydrothermal process without the use of any template or organic surfactant. These morphologies possessed a loose mesoporous cluster structure consisting of thin plates or nanowires and exhibited enhanced rate capacity and cyclability. After 350 charge-discharge cycles the capacitance diminished to 89% suggesting minor microstructural changes in the MnO_2 material.

The fourth type of morphology is a thin film. Since one of the proposed charge-discharge mechanisms of MnO_2 is based on surface adsorption of MnO_2 a thin-film morphology would allow for high areal capacitance and high utilization rate of the MnO_2 material. Park et. al [21] achieved an areal capacitance of 52.55 mF cm^{-2} , along with superior structural integrity and adhesiveness of the film to the current collector. Nanopillar arrays (Figure 8) and porous structures have also been utilized as unique morphology types. Yu et. al [22] showed that the surface area of their MnO_2-decorated polyacrylonitrile (PAN) nanopillar array was 4.5 times greater compared to that of the thin film morphology and possessed improved structural stability

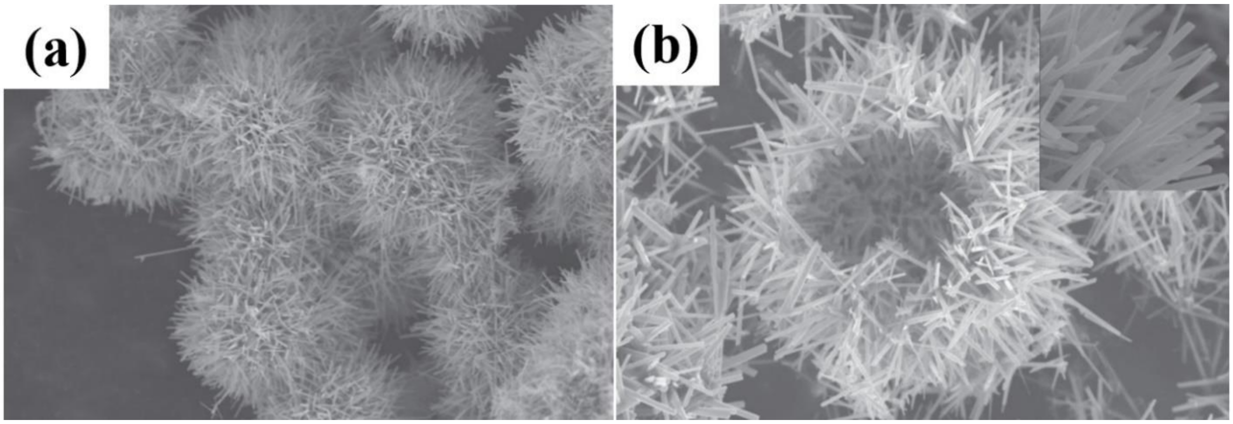

Figure 7. (a) (b) SEM images of MnO_2 nanourchins.

during intercalation and deintercalation. This yielded better utilization of the material, higher specific capacitance, better charge-discharge behaviour and greater cyclic stability.

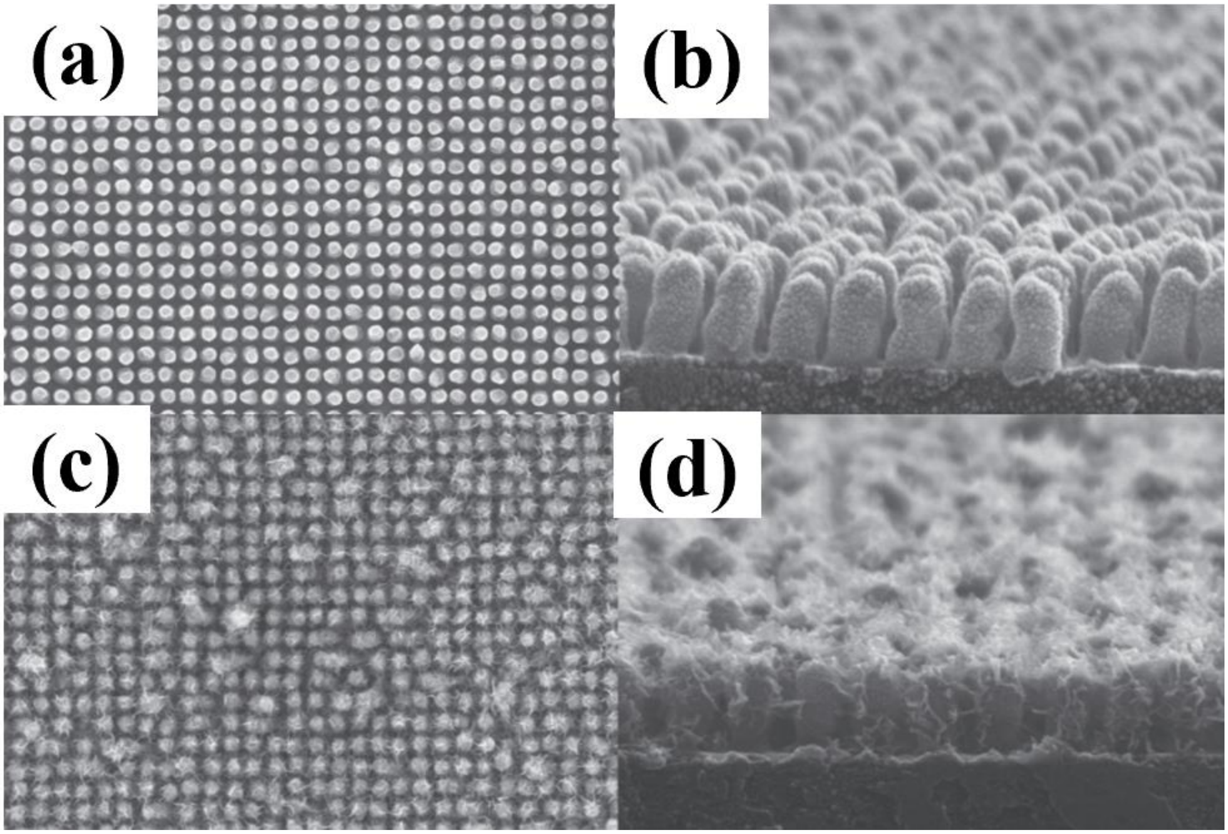

Figure 8. SEM images showing (a) top view of PAN nanopillars (b) side view (c) top-view of MnO_2-decorated PAN nanopillars and (d) side view.

Nanoporous structures [23] have also been gaining traction due to their remarkable surface area and high utilization of material which reduces the dead volume.

In summary, the aim in investigating these morphologies is centered around increasing surface area, utilizing more of the MnO_2 material, and reducing the diffusion lengths for electrons and ions. These optimizations translate to higher specific capacitance values, high charge-discharge rates, better structural stability, and increased cyclic stability. Table 2 compares the capacitance of the morphologies discussed in this section.

Table 2. Comparison of capacitance values for various MnO_2 morphologies.

Morphology	**Capacitance**	**Reference**
Nanowires	350 F g^{-1}	[16]
Nanorods	243 F g^{-1}	[16]
Nanobelts	91 F g^{-1}	[19]
Nanotubes	365 F g^{-1}	[18]
Nanospheres/nanourchins	167 F g^{-1}	[20]
Nanopillars	603 F g^{-1}	[22]

3.3.3 Conductivity

As with any electrochemical energy storage device the conductivity is a key component in the performance of the device. The electrical conductivity is a vital factor which determines the flow of electrons in and out of the electrode. As the rate of charge-discharge increases the resistance of the electrode exaggerates – especially for materials with low conductivity, as is the case with MnO_2 (10^{-5} to 10^{-6} S cm^{-1}). To combat this, MnO_2 can either be doped with other metal elements such as, Cu, Ni, and Fe, or it can be composited with conductive additives such as graphene and carbon nanotubes.

In the case of doping, the exploitation of defects has proven to greatly increase the conductivity and charge-storage capability. Hashem et al. [24] investigated the use of Al, Cu, and Mg doping elements and discovered that Al-doped MnO_2 gave the lowest resistance, the best capacity retention, and recharge efficiency. In addition, all three doping elements provided increased thermal stability. Wang et. al [25] utilized Mo to dope their MnO_2 and prepared supercapacitor devices with an asymmetric setup (activated carbon (AC) as the negative electrode and AC/Mo-doped MnO_2 as the positive electrode). They discovered that 15 mol% Mo-doped MnO_2 was the optimal composition to reduce the resistance, however the conductivity of their doped MnO_2 did not match that of the activated carbon.

The use of Zn as a doping element was also investigated by Poonguzhali et. al [26]. The charge transfer resistance of the MnO_2:Zn (0.125 M) electrode was measured at 109.2 Ω, while the pure MnO_2 electrode was measured at 275 Ω. This low electron transfer resistance of the Zn-doped MnO_2 led to enhanced electrochemical performance.

In the case of Co, hierarchical spheres of Co-doped MnO_2 were prepared by Tang et. al [27]. They measured a specific capacitance of 350 F g^{-1} at a current density of 0.1 A g^{-1} for the spheres with a Co/Mn ratio of 0.5%, while the undoped MnO_2 with a similar hierarchical spherical structure was measured at about 168 F g^{-1}.

Conductive additives are an alternative solution to improving the conductivity of MnO_2 electrodes. Efforts are being made in depositing or synthesizing MnO_2 onto conductive porous substrates (e.g. graphene) via chemical deposition, thermal deposition, and electrochemical deposition [28–29]. Yu et. al [30] reported that 3D conductive wrapping of graphene/MnO_2 nanostructures with carbon nanotubes (CNTs) or a conducting polymer (CP) substantially increased the specific capacitance by ~20% and ~45%, respectively, with gravimetric capacitance values as high as about 380 F/g. Their composites also exhibited cyclic performance with >95% retention over 3000 cycles. Ternary composites of MnO_2, CNTs, and polymers have also been studied. Hou et. al [31] synthesized a composite with MnO_2, CNT, and PEDOT-PSS – a conductive polymer that serves as a binding agent and dispersant. Their composite was able to sustain a cyclic stability of 99% for 1000 cycles, as well as 85% retention of specific capacitance as the current density was increased from 5 to 25 mA cm^{-2}.

In conclusion, both the addition of certain doping elements and the use of conductive additives are promising methods to achieve high-performance MnO_2-based electrodes and devices.

3.4 Polypyrrole

Conducting polymers are the second main category of electrode materials for ESs. Popular examples of CPs are polypyrrole, polyaniline, and polythiophene. Along with offering large theoretical capacitance, good electrical conductivity, and environmental stability, CPs have two key advantages over their transition metal oxide counterparts: ease of large-scale production and low cost [32]. Their main drawback, however, is their poor cyclic stability which stems from the continuous swelling/shrinking of their chains during charge-discharge cycles. To combat this, some researchers have designed composites of metal oxide-CPs and CP-carbon materials to improve the electrochemical performance [33–37].

3.5 Conductive Additives

Although MnO_2 films exhibit supercapacitance values of ~700 F g^{-1} [11], [38], the poor conductivity of MnO_2 diminishes the overall performance as the thickness of the film is increased. To mitigate this issue conductive additives are composited with MnO_2, such as graphene, carbon nanotubes, carbon fibers, and carbon black [39–41]. This strategy results in an increased capacitance by facilitating charge transport from redox sites to the external circuit [42–44]. It is important to note that the making of such composites axiomatically leads to a decrease in the fraction of the capacitive material. Therefore, it is vital that the amount of conductive additive is optimized to avoid any excessive decrease in the overall capacitive performance.

The growing interest in using carbon nanotubes as the conductive additive is due to its low percolation threshold and its high conductivity. When the volume fraction of the conductive additive in a matrix is relatively low the conductivity remains close to that of the pure matrix. As the volume fraction of the conductive additive is gradually increased there comes a point where the conductivity of the composite suddenly increases by many orders of magnitude. This critical point of volume fraction is termed the percolation threshold. Although, there are many factors which dictate the percolation threshold such as processing technique and the type of matrix. A major factor is the aspect ratio of the conductive additive. Materials with high aspect ratios and small form-factors possess lower percolation thresholds, as seen with carbon nanotubes (aspect ratio of 100-10,000) [45].

The choice of processing technique is just as important as the choice of the conductive additive. Two different processing techniques utilizing the same conductive additive can yield differing results in electrode performance. For example, in one investigation [46] a composite of amorphous MnO_2 with CNTs was prepared by chemical precipitation of manganese oxide from $KMnO_4$ and $Mn(OAc)_2 \cdot 4H_2O$ water solutions in the presence of CNTs. Capacitance values reached 204.8 F g^{-1} in 1 M Li(Ac)-1 M $MgSO_4$ solutions, but the cyclic stability was comparatively lower than what was achieved by other composites [46]. In contrast, Xie et. al employed a similar in-situ coating technique to prepare MnO_2-MWCNT (multi-walled carbon nanotube) composites [47] and achieved a capacitance of 250 F g^{-1}. However, this technique presented difficulty in controlling the amount of MnO_2, as well as preventing degradation of the carbon nanotube surfaces upon reduction of the $KMnO_4$ precursor [48]. New dispersion and mixing strategies have been developed to avoid these drawbacks as seen in the work of Wallar et. al [49]. Utilizing the Schiff base linkage mechanism, they were able to synthesize composites with a retention of 66% at a scan rate of 100 mV s^{-1} and an areal capacitance of 4.4 F cm^{-2} at a scan rate of 2 mV s^{-1}. The Schiff base linkage mechanism, as well as other colloidal suspension techniques will be comprehensively discussed in later sections.

3.6 Current Collectors

The choice of current collector plays an important role in the performance of supercapacitors. Generally, it serves three functions: (1) to act as a physical support to hold the active material in place inside the cell; (2) absorb mechanical stresses caused by external forces or volume changes of active materials during cycling; (3) to carry the electric current in/out of the electrode. During the fabrication stage of the supercapacitor electrode the composite slurry is applied to the current collector. It is preferable to use current collectors with high porosity and large pore size to allow for easy access of the composite slurry because this allows for high mass loading of the composite [50]. Ideal characteristics for current collectors include the following: chemical stability in aqueous electrolytes; electrochemical stability during the charging-discharging process; low density; high conductivity; low costs; and good processability to form porous structures.

As seen in Equation 6, the power of the device is dependant on how low the resistance is kept. Thus, the contact resistance between the current collector and the active material must be kept low. One group achieved this by electrochemically etched away their aluminum foil current collector to create pits 10-15 microns in depth which increased the specific surface area. Then they applied a conductive carbonaceous material onto an aluminum current collector via a sol-gel route. The resistance of the electrode dropped due to the continuous interface between the collector and the active material.

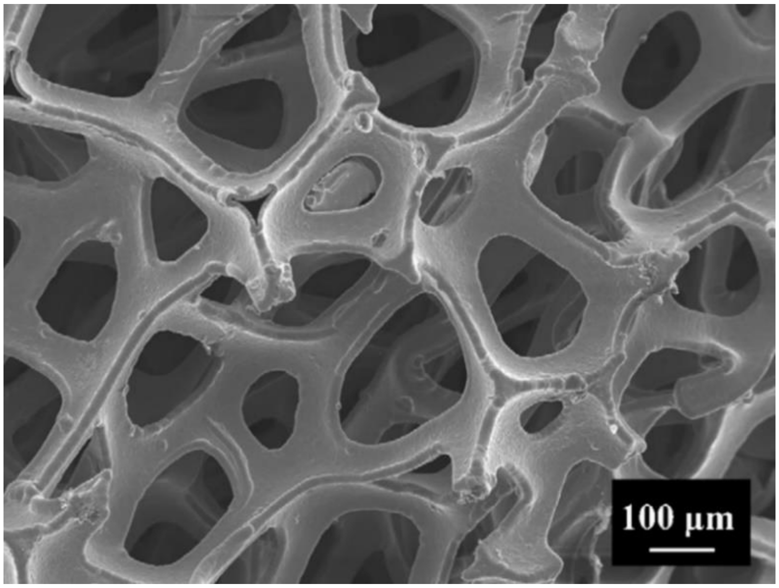

Figure 9. SEM image of nickel foam. Source: Ref. [57]

Along with aluminum, carbon-based materials are attractive choices for current collectors as they do not corrode in aqueous electrolytes and are also flexible. Furthermore, carbon nanofoam papers and Co_3O_4 nanowire array current collectors could potentially even contribute to the capacitance for some ESs [52–53]. For the investigations carried out in this work Ni foam was the current collector of choice. Nickel foam has proven [54–56] to be a promising material for current collectors due to its easy processability, ability to hold high amounts of electroactive material, good conductivity, and mechanical strength. Figure 9 displays an SEM image of Ni foam detailing its high porosity and large pore size. This allows for effective impregnation of the composite slurry into the porous structure. Increasing the foam porosity can reduce the conductivity of the overall electrode [47], but utilizing CNT allows for secondary conductive webs within the nickel foam, thereby counteracting the losses.

The *R* ratio is another factor of consideration for the fabrication of SC electrodes. It is the ratio of the mass of the active material to the mass of the current collector. It is ideal to have a large *R* ratio since more of the device's mass is contributing to the capacitance. If it were the other way around then the mass of the current collector, which does not contribute to the capacitance, would make up more of the device's mass thus resulting in deadweight.

3.5 Mass Loading

The mass loading is a critical parameter which allows researchers to quantitatively measure the practicality of the fabricated electrode. It is effectively the amount of active material that is applied onto the current collector. Mass loadings can range from less than a microgram to tens of milligrams per centimeter square. Though, with smaller mass loadings come 'exaggerated' specific capacitance values. The reason for this is that the electrolytic species can diffuse more easily when there is less material to diffuse through since diffusion lengths are small. In addition, fewer electrolyte species are needed to ensure all the active sites are activated during charging and discharging. Oppositely, at high mass loading the electrolyte species must diffuse through more material since diffusion lengths are increased. Furthermore, additional electrolyte must be used to ensure ions are able to penetrate through the channels. Consequently, the specific capacitance tends to drop as mass loading is increased. For example, nanoporous carbon electrodes can exhibit a drop in capacitance by 2-3 times when the mass loading is increased [58]. In addition, the electrical conductivity is decreased and the series resistance in increased.

Many studies which showcase exceptional capacitive performance often use mass loadings of less than 1 mg cm^{-2}. The primary issue for many investigations is the limited supporting surface area and non-uniform porous structure of the conductive substrates that are employed. Regardless, practical applications dictate that mass loadings be at least 10 mg cm^{-2} [59]. Furthermore, what is imperative in reporting electrode performance is the areal or volumetric capacitance and not just the gravimetric capacitance [59], as the form factor is a crucial component in the design of end-applications.

3.6 Electrolytes

The electrolyte is a fundamental component in the construction of a supercapacitor device. It's function in a supercapacitor device is of two-fold: 1) interconnect the positive and negative electrodes and 2) facilitate charge transport between the electrodes. The choice of electrolyte is heavily deterministic of the device's power and energy characteristics due to its influence on the maximum applied voltage (refer to Equation 5 and Equation 6). Generally, the nature of any electrolyte is considered by the following [12]: the ion type and size; the ion concentration and solvent; the interaction between the ion and solvent; the interaction between

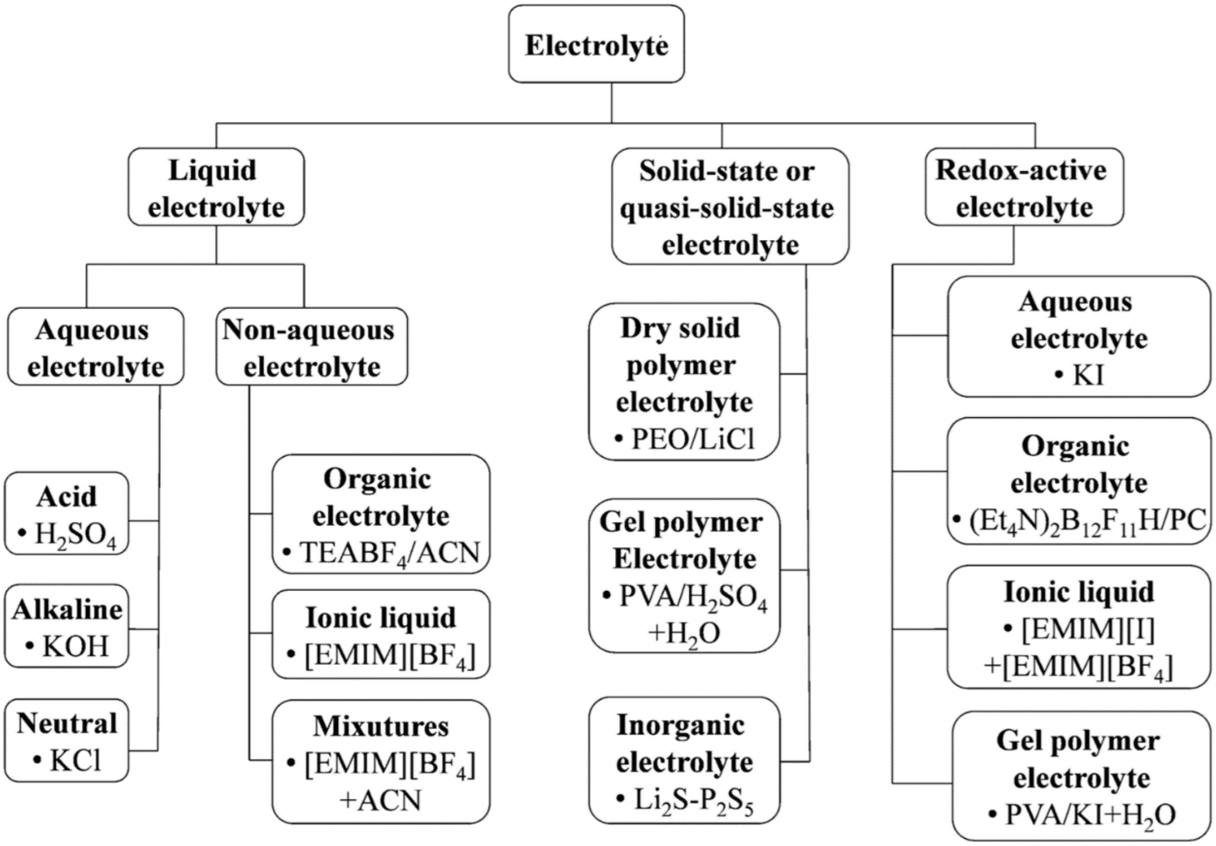

Figure 10. Family tree of electrolytes for electrochemical supercapacitors.

the electrolyte and the electrode materials. Ideal characteristics for electrolyte applications are good ionic conductivity, high thermal stability, wide voltage window, low toxicity, low cost, low resistivity, and high electrochemical stability. As seen in Figure 10 there are 3 main categories, each with their sub-categories of electrolytes that have been developed over the years. Zhong et. al [60] provide a comprehensive review of recent research and development efforts made in all categories of electrolytes for ESs.

Each category of electrolyte comes with its own set of advantages and disadvantages. Aqueous and organic electrolytes are two sub-categories under the broader category of liquid electrolytes. While aqueous electrolytes possess relatively high ionic conductivity and capacitance their narrow voltage window limits their energy density. In contrast, organic electrolytes suffer from low ionic conductivities but offer much wider voltage windows. Solid-state electrolytes alleviate the leakage problem which plagues many supercapacitor designs, but their ionic conductivity is relatively low.

Table 1 provides a comparison of the advantages and disadvantages of organic and aqueous electrolytes.

Due to their low cost and ease of synthesis aqueous electrolytes for ECs have received more attention in research and development efforts than organic electrolytes [60]. However, many commercial applications currently utilize organic electrolytes. The reason for this may be due to the current market demand revolving around high energy density performance for ESs – a characteristic which is met by large operating voltage windows. Aqueous electrolytes are restricted to narrow voltage windows due to the breakdown voltage of the solvent being water. Oxygen evolution can occur at the positive electrode at only 1.23 V [61] and this can pose safety risks and significant drops in performance. As a safety factor the high limit of the operating voltage is restricted to 1.0 V [62] or even lower. A key benefit aqueous electrolytes offer is their high ionic conductivity. This lowers a device's electrochemical series resistance (ESR), which ultimately leads to enhanced power delivery. Fundamentally, it is the conductivity and mobility of the electrolyte which affects the supercapacitor's performance. The mobility is essentially that part of the conductivity that is independent of concentration [63]. But, both terms depend on the charge of the ion, its solvated radius, and the viscosity of the solvent [63].

In contrast, organic electrolytes offer wider voltage windows and are compatible with cheaper current collectors and packaging materials. However, in some cases the wider voltage window can cause degradation of the oxide material in the electrode [64–65]. Furthermore, ESs constructed with organic electrolytes come with higher costs, smaller specific capacitance, lower conductivity, and safety concerns related to the flammability and toxicity. Organic electrolytes are also sensitive to oxygen and moisture; even trace amounts can seriously degrade performance and exacerbate self-discharge issues [62]. Controlling the synthesis environment requires complicated purification and assembly procedures (requiring expensive equipment) thereby hindering many potential research and development efforts. Nevertheless, according to one market forecast [66] aqueous and organic electrolytes will be the top two competitors for ES devices for the foreseeable future. Currently, organic electrolytes are dominating the product lines for major ES market shareholders such as Maxwell, Nesscap, and Panasonic.

Table 1. A detailed performance comparison between aqueous and organic electrolytes.

Types		Disadvantages
Aqueous (e.g. H_2SO_4, KOH, Na_2SO_4)	• High ionic conductivity • Low cost • Non-flammability • Non-corrosiveness • Safe • Compatibility in air and O_2	• Small voltage window • May accelerates degradation of components • May modify oxide electrodes • High self-discharge

	• Small hydrated cations • Good wettability • Wide operating temperature	
Organic (e.g. acetonitrile, propylene carbonate)	• Large voltage window • Electrostatic phenomena • No chemical modification of electrode • Excellent reversibility • Low self-discharge • Low degradation of components	• Complex synthesis • Costly • Usually flammable • Low ionic conductivity • High toxicity • Large ion size • Poor impregnation of electrode pores

Solid-state and quasi-solid-state electrolytes (SSEs) have begun to receive more attention as markets for portable, micro, wearable, and printable electronics gain traction. SSEs have the primary advantage of alleviating the leakage problem seen in liquid-based electrolytes, as well as simplifying the packaging and fabrication process of supercapacitor and battery devices. With recent catastrophic market failures [67] seen with liquid electrolytes SSEs may become more of an attractive alternative. In fact, one forecast report [68] predicts the market for SSE-based devices to reach over $25 billion by 2029.

To date, SSE development has largely focused on polymer electrolytes. Two sub-categories under polymer electrolytes are solid-polymer and gel-polymer; the former offers greater safety but poor ionic conductivity, whereas the latter offers higher ionic conductivity. Both sub-categories can sustain high operating voltage windows (~4 V), allowing for high power and energy densities. Gel-polymer electrolytes, however, use organic solvents which are environmentally hazardous. Consequently, recent efforts have gone into substituting organic solvents with water [69]. Nevertheless, the overarching category of solid electrolytes have already been tested with EDLCs, pseudocapacitors, and hybrid ESs – all with different materials.

Ionic liquids (ILs) (also known as room-temperature molten salts) are defined as salts composed of an asymmetric mix of organic cations and inorganic (or organic) anions. The unique combination of cations and anions is what gives rise to the low melting point characteristic. Other positive characteristics include negligible volatility, flame retardancy, moderate viscosity, high polarity, thermal and chemical stability, high ionic conductivity, and wide voltage windows. However, research and development efforts in ionic liquids are only beginning to expand, leaving many challenges incomplete [70]. The main challenge is to ensure a high voltage window can be maintained with a high ionic conductivity while assuring good wettability of the electrode pores by the ionic liquid. Furthermore, current EDLC designs employing ILs are restricted to operate at lower voltage windows than what is offered by ILs. This is because the potential of discharged carbon electrodes is usually far from the mid-point of the IL’s electrochemical stability window (ESW). Upon charging, both electrodes experience the same potential excursion. Consequently, V_{max} is restricted by the electrode that first reaches the ESW limit [71].

4 Problem Statement

Currently, the true capacitive potential of MnO_2 can only be actualized when thin-film fabrication techniques are used. Since thin films are restricted to relatively low mass loading values (typically less than 1 mg cm^{-2}) this introduce the problem of practicality. Past studies [59] have stressed the importance of fabricating supercapacitor electrodes with high active mass loading and *R* ratios.

Since increasing the mass loading on thin-films causes severe performance degradation and loss of optimization alternative techniques must be explored. Colloidal suspension techniques can allow for high and practical mass loading values; however, they are limited from reaching the true capacitive potential of MnO_2. The reason for this is partly due to the synthesis method of MnO_2 particles. They are typically synthesized separately in an aqueous solution, while the conductive additives (MWCNT) are dispersed in an organic solvent. As a result, the MnO_2 particles must be dried and re-dispersed into the MWCNT solution to allow for proper mixing. However, upon drying the MnO_2 particles agglomerate due to the reduction in the particle surface area and condensation of the surface OH groups. This leads to a significant drop in the capacitive performance.

The hydrothermal synthesis method is technique for preparing 1D MnO_2 nanorods with unique physical and electrochemical properties. However, poor dispersion and mixing of the nanorods can lower their surface area and lower the electrochemical performance. There are many organic additives and/or templates which can successfully control the nucleation, growth, alignment, dispersion, and mixing of inorganic materials, but limited literature exists in understanding this effect specifically on MnO_2 nanorods.

Polypyrrole is another SC material undergoing intensive research due to its ease of synthesis, inherent fast redox switching, high conductivity, mechanical flexibility, and environmentally benignity. However, since electrochemically inert counter-ion dopants are typically employed during synthesis the attainable specific capacity is relatively low and impractical for SC applications. Another problem for PPy ES is its poor cyclic stability. Poor cyclic stability is a result of the swelling and shrinking of the films which is due to the highly mobile dopants that are typically employed for PPy synthesis.

A strategy to combat both these problems is to dope PPy with large electrochemically active anionic dopants. Such dopants can contribute to the quantity of charge stored.

Furthermore, their large size reduces their mobility during charging/discharging and reduces the amount of swelling or shrinking possible. Additionally, anionic dopants with multiple charged groups can be linked to different polymer macromolecules to increase the interchain mobility of charge carriers, thereby boosting conductivity. [72]

5 Objectives

The long-term objective of this investigation was to develop MnO_2 and PPy-based composites for the fabrication of advanced supercapacitor electrodes with high capacitance, good capacitive retention at high scan rates, along with high mass loading values (> 10 mg cm^{-2}). In the case of MnO_2 reaching this long-term objective required the development of novel colloidal and morphology modification techniques to improve the dispersion of MWCNT and MnO_2, as well as their inter-mixing. In the case of PPy the objective was to investigate novel anionic dopants as a strategy to improve the cyclic stability and electrochemical performance of PPy electrodes.

6 Experimental Procedure

6.1 Electrode Fabrication

The composite (under investigation) is measured out to the desired amount and is transferred to a mortar. A 3 g L^{-1} Poly(vinyl butyral-covinyl alcohol-co-vinyl acetate) (PVB) binder in ethanol solution is added to the mortar such that the composite powder occupies 97% of the total mass. The mixture is finely ground with a pestle to achieve a homogenous slurry and is then applied to a Ni foam piece over a 1 cm^2 area. After the slurry has dried the foam piece is pressed to a desired thickness. Following this, a hole that is just large enough for a 0.5 mm diameter strand of copper wire is punched through the other end of the Ni foam piece. A strand of copper wire is fed through a 10-inch long glass tube and is kinked on one end to form a hook for insertion of the Ni foam piece. The kinked copper wire end is inserted through the hole of the Ni foam and the kink is pressed down flat against the Ni foam, after which it is soldered down with Pb-Sn solder wire. The unoccupied area of the Ni-foam is then covered with Gorilla epoxy glue to prevent it from skewing the electrochemical testing results.

6.2 Preparation of MnO2 Particles using Ethanol

A common technique to synthesize MnO_2 particles is to use $KMnO_4$ as a precursor with a primary, secondary, or tertiary C_2–C_5 alcohol as the reducing agent. For our investigations, ethanol was the primary choice of alcohol as it allows for a high S_{BET} area for the particles. Upon dissociation of $KMnO_4$ in water it can be assumed that a significant fraction of the permanganate ions will be directly reduced to form MnO_2 with the addition of ethanol, as seen in Equation 13.

$$MnO_4^- + 4H^+ 3e^- = MnO_2 + 2H_2O \qquad \text{Equation 13}$$

6.3 MnO2-MWCNT Composite Synthesis via Schiff-base Linkage

In a typical synthesis procedure 0.2 g of $KMnO_4$ is added to a beaker of 100 mL of water. The solution is magnetically stirred for approximately 5 minutes before the addition of 50 mL of ethanol, upon which the beaker is continuously stirred for 3 hours to yield 0.11 g of MnO_2. Following this 0.011 g (10 wt% MnO_2) of the complexing agent (under investigation) is added to the beaker and stirred for 24 hours. A separate beaker with 50 mL of water and 0.276 g of MWCNT is ultrasonicated for 30 minutes. The mass of MWCNT is such that the mass ratio of CNT:MnO_2 is 1:4 as this specific ratio was found to be optimal according to a past study [57]. The specific dye is added to the CNT beaker in a 1:1 ratio of CNT:dye and undergoes another ultrasonication sequence for 30 minutes. The CNT-dye suspension is added to the MnO_2-complexing agent suspension, stirred for 30 minutes and then ultrasonicated for another 30 minutes to ensure all constituent materials are thoroughly mixed. The final suspension is filtered through a vacuum filtration pump using 1 μm filter paper and ethanol as a flushing solvent to wash away any excess dye. The resulting slurry is transferred to a plastic tray and oven-dried at approximately 60^oC for 1 day to yield the final composite.

6.4 MnO_2-MWCNT Composite Synthesis via co-dispersion

In a typical synthesis procedure 0.2 g of $KMnO_4$ is added to a beaker of 100 mL of water. The solution is magnetically stirred for approximately 5 minutes before the addition of 50 mL of ethanol, upon which the suspension is continuously stirred for 3 hours to yield 0.11 g of MnO_2. In a separate beaker, 0.276 g of MWCNT is added to 50 mL of water and ultrasonicated for 30 minutes. Thereafter, 0.011 g (10 wt% MnO_2) of GC dye is added to the CNT suspension and is ultrasonicated for 30 minutes. The CNT-GC suspension is added to the MnO_2 beaker and stirred for 18 hours to allow enough time for the CNT and MnO_2 to adsorb via the co-dispersant. The final suspension is filtered through a vacuum filtration pump using 1 μm filter paper and ethanol as a flushing solvent. The resulting slurry is transferred to a plastic tray and then oven-dried at approximately 60^oC for 1 day to yield the final composite.

6.5 MnO_2-MWCNT Composite Synthesis via Liquid-Liquid Extraction

In a typical procedure 273 mg of $KMnO_4$ is added to 50 mL of water and magnetically stirred for 10 minutes, after which 10 mL of ethanol is added to initiate the reduction process. After stirring the water-ethanol-MnO_2 mixture for 3 hours 20 mL of undecanal is added to extract the MnO_2 particles out of the aqueous phase. In a separate beaker, 37.5 mg of MWCNT is added to 50 mL of water and ultrasonicated for 2 hours. Thereafter, the MWCNT suspension is added to the extracted MnO_2 beaker and the mixture is stirred for 1 hour. The mixture is then transferred to a vacuum filtration pump. Ethanol is used to flush out any excess undecanal, leaving behind the MnO_2-CNT composite in a slurry form. The slurry is left to air dry at room temperature for 1 day to yield the final composite.

6.6 MnO_2 Nanorods-MWCNT Composite Synthesis via Hydrothermal Method

A typical procedure for the synthesis of MnO_2 nanorods-MWCNT composites involves mixing 20 mmol of $KMnO_4$ and 30 mmol of $MnSO_4 \cdot H_2O$ in a beaker of 160 mL of water. The solution is magnetically stirred for 30 minutes after which it is transferred to an autoclave to undergo a hydrothermal treatment at 140^{o}C for 12 hours. In a separate beaker, MWCNTs and the dispersant (under investigation) are added with water such that the mass ratio of CNT:MnO_2 is 1:4 and the CNT:dispersant ratio is 2:1. Upon completion of the hydrothermal treatment the nanorods are poured out of the autoclave and into a beaker to be pH-adjusted to neutral with a KOH solution. The CNT suspension is added to the beaker of neutral-pH MnO_2 nanorods and the mixture undergoes a sequence of 30 minutes stirring and 30 minutes ultrasonicating. The composite is transferred to a vacuum filtration pump and washed with water and ethanol, then subsequently dried in a furnace at 60^{o}C for 1 day to yield the final composite.

6.7 Polypyrrole-MWCNT Composite Synthesis via Chemical Polymerization

In a typical procedure a specified quantity of pyrrole is micro-pipetted into a beaker and stored in a fridge at 4^{o}C. In a separate beaker, ammonium persulfate (APS) is added to 50 mL of water such that the molar ratio of APS:pyrrole is 3:1. In another beaker the dopant (under investigation) and MWCNTs are added to 100 mL of water and ultrasonicated such that: the molar ratio of dopant:pyrrole is 1:10; the molar ratio of dopant:CNT is 1:2; and the mass ratio of CNT:pyrrole is 1:4. Both beakers are kept in an ice bath to bring down the temperature to 4^oC. Once the temperature stabilizes the pyrrole is added to the dopant solution. This is immediately followed by the addition of the APS solution. The resulting mixture is magnetically stirred for approximately a day. However, for the first 4 hours of this sequence the solution is maintained at 4^oC. Afterwards, the suspension is transferred to a vacuum filtration pump and is filtered with water and ethanol to wash away any excess dopant. The resulting slurry is dried in a furnace at 60^oC for 1 day to yield the final composite.

6.8 Materials Characterization

6.8.1 Crystallinity

X-ray diffraction (XRD) data were collected using the McMaster Analytical X-Ray Diffraction Facility’s powder diffractometer (Nicolet I2, monochromatized CuK_α radiation) at a scanning speed of 0.5 min^{-1}.

6.8.2 Morphology

The morphological characterization of the MnO_2 samples was done by a JEOL JEM 1200 EX TEMSCAN transmission electron microscope (JEOL, Peabody, MA, USA) operating at an accelerating voltage of 80 kV. Sample preparation was done by micro-pipetting a drop from the MnO_2 aqueous suspension (under investigation) onto a TEM grid and leaving it to air dry.

6.9 Electrochemical Testing

6.9.1 Cyclic Voltammetry

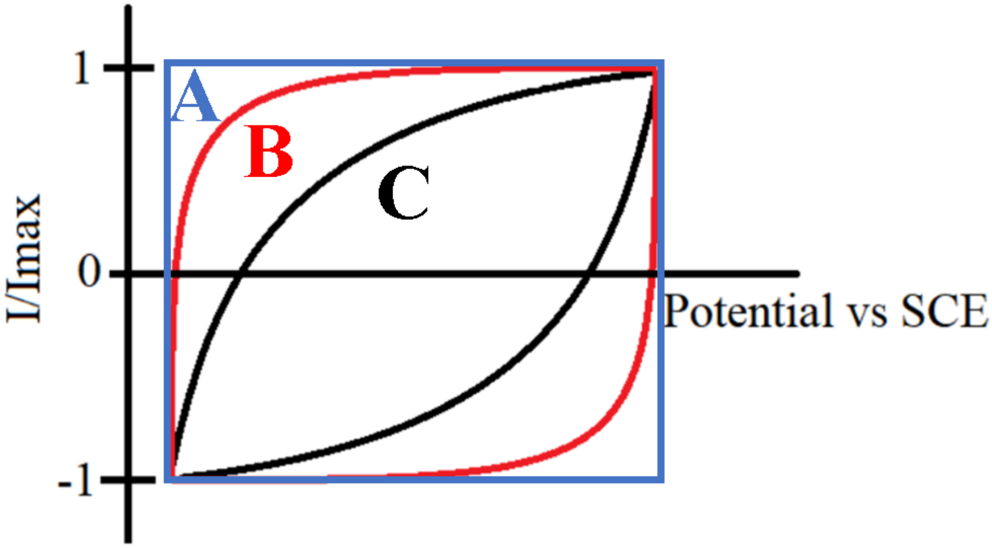

Figure 11. Shapes of cyclic voltammograms for **A** ideal capacitor and **B** supercapacitor at low scan rates and **C** high scan rates. Source: Ref. [73]

In a cyclic voltammetry scan a potential ramp is applied to the working electrode by increasing the potential to a limit and then reversing the scan back to the initial potential. The generated graph is called a voltammogram. The capacitance (measured in Farads) can be extracted by dividing the integrated area of the voltammogram by the product of the voltage window and scan rate, as seen in Equation 14:

$$C = \frac{1}{2(V_{max} - V_{min})v} \int_{V_{min}}^{V_{max}} I(V)dV \qquad \text{Equation 14}$$

The rate at which the scan is applied determines the *scan rate*. Curve C in Figure 11 is a typical voltammogram observed at high scan rates. They are smaller in area and are more curved due to the lagged kinetic effects of the electrolytic species. In curve B of Figure 11 the voltammogram is larger in area and closer to the theoretical box shape of an ideal capacitor (curve A in Figure

11). This is due to slower kinetic effects at lower scan rates which allow more electrolytic species to penetrate the electrode pores, thereby generating a higher capacitance.

For the investigations in this work cyclic voltammetry tests were conducted with a 3-electrode system (with Pt gauze as the counter electrode and a SCE for the reference electrode) using 0.5 M Na_2SO_4 electrolyte. Scan rates were varied at 2, 5, 10, 20, 50, and 100 mV s^{-1}. The potential was swept between 0 and 0.9 V for the MnO_2-MWCNT systems and between -0.5 and 0.4 V for the polypyrrole-MWCNT systems.

6.8.2 Impedance Spectroscopy

The term *impedance* refers to the frequency-dependent resistance to current flow of a circuit element, such as a capacitor. The impedance is measured by applying a potential with a characteristics sinusoidal wave function of a specific frequency and measuring the current response. The frequency of the wave function is changed for a certain range and the current responses are measured to gather the relevant data. Electrochemical impedance spectroscopy (EIS) is theoretically complex compared to single-frequency measurements or DC measurements. The benefit of EIS is that it provides more information such as: distinguishing between two or more electrochemical reactions taking place; identifying diffusion-limited reactions; information on the capacitive behaviour of the system; and information on the electron transfer rate of the reactions. Furthermore, the real and imaginary components of the complex capacitance, C_s' and C_s'', can be differentially calculated from the impedance data. These calculations of capacitance are different from the integral calculation of capacitance obtained from CV data. In the EIS method the differential capacitance is calculated using an alternating current with an amplitude of 5 mV and depends on the change in frequency, whereas in the CV method the integral capacitance depends on the scan rate.

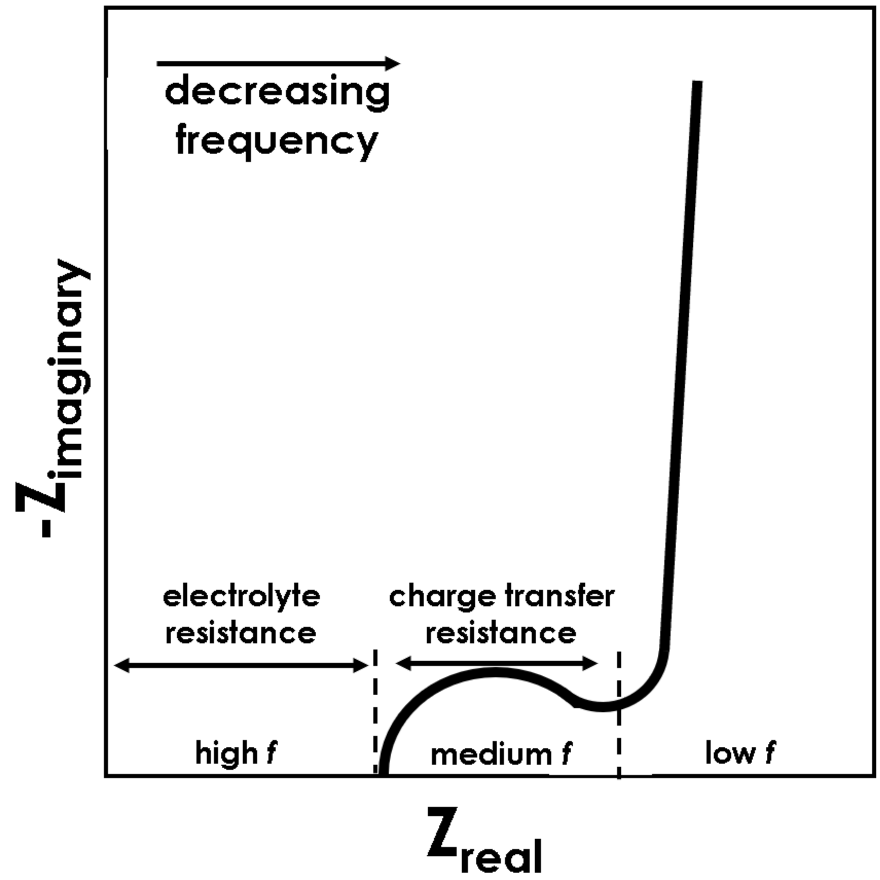

Figure 12. Plot of typical Nyquist plot acquired through EIS testing of supercapacitor electrodes.

For typical investigations in this work the alternating current measurements of complex impedance $Z^* = Z' - iZ''$ were performed in the frequency range of 10 mHz - 100 kHz at a signal amplitude of 5 mV. The real and imaginary components of the complex differential capacitance were calculated from the impedance data as $C_S' = Z''/\omega|Z|^2$ and $C_S'' = Z'/\omega|Z|^2$, respectively, where $\omega = 2\pi f$ (f is frequency). By separating the complex capacitance into its real and imaginary components, the associated maxima seen typically in C_s'' plots can be correlated with the effect that the pore sizes have on the penetration of the solvated cations in the electrolyte. In addition, the associated frequency at this maximum can be used to calculate the time constant – a parameter which is described as the dielectric relaxation time of the electrode.

The EIS data can also be used to construct a Nyquist plot (Figure 12) which is a plot of the negative of the imaginary component versus the real component of the complex impedance. Since the full physical interpretation of this plot can be quite extensive only relevant information will be discussed. The first segment is at high frequencies; the second segment at medium frequencies; the third at low frequencies. The point that marks the beginning of the semicircle is attributed to the bulk electrolyte resistance, the electrode resistance, and the contact resistance between the electrode and the current collector [74]. The diameter of the semicircle contained within the medium frequency range is assigned to the electrolyte resistance in the pores of the electrode and the charge transfer resistance [74]. The vertical line seen in the low frequency range is attributed to the to the dominant capacitive behaviour of the electric double layer formed at the electrode/electrolyte interface [74].

6.8.3 Galvanostatic Charge-Discharge

In contrast to cyclic voltammetry, galvanostatic charge-discharge tests operate by controlling the current density and measuring the potential versus time response. Important characteristics such as cyclic stability, capacitance, energy density, and power density can be extracted from the charge-discharge test data. The specific capacitance is calculated with Equation 15:

$$C = \frac{It}{m\Delta V} \qquad \text{Equation 15}$$

Energy and power densities can be calculated from Equation 16 and Equation 17, respectively:

$$S_E = \frac{I\Delta t(V_{max} - V_{min})}{2m} \qquad \text{Equation 16}$$

$$S_P = \frac{I(V_{max} - V_{min})}{2m} \qquad \text{Equation 17}$$

where I is the current, t is the time taken for discharging, m is the mass loading, V_{max} is the maximum voltage of the potential window, and V_{min} is the minimum voltage of the potential window.

7 Results and Discussion

7.1 Schiff-base Linkage Approach for the Synthesis of MnO_2-MWCNT Composites

7.1.1 Background

In the case of MnO_2-MWCNT composites the agglomeration problem (formulated in *Section 4 Problem Statement)* can be avoided if the MWCNT and MnO_2 are both mixed and dispersed in solutions. This can be achieved using colloidal suspension techniques: Schiff-base linking, co-dispersion, and liquid-liquid extraction (LLE). This section and the next two sections will discuss each of these techniques.

The Schiff base linkage mechanism provides an efficient way to mix MnO_2 particles and MWCNTs by creating a "bridge" between the constituent components. In a Schiff base reaction, the electrophilic carbon atoms of aldehydes are targets of nucleophilic attack by amine groups. This reaction yields a Schiff base by replacing the C=O double bond from the aldehyde with a C=N double bond [75]. Therefore, the Schiff base reaction requires two molecules: one which possesses an aldehyde group and can readily adsorb onto the surfaces of MnO_2 particles, and another which possesses an amine group and can readily adsorb onto the surfaces of MWCNT.

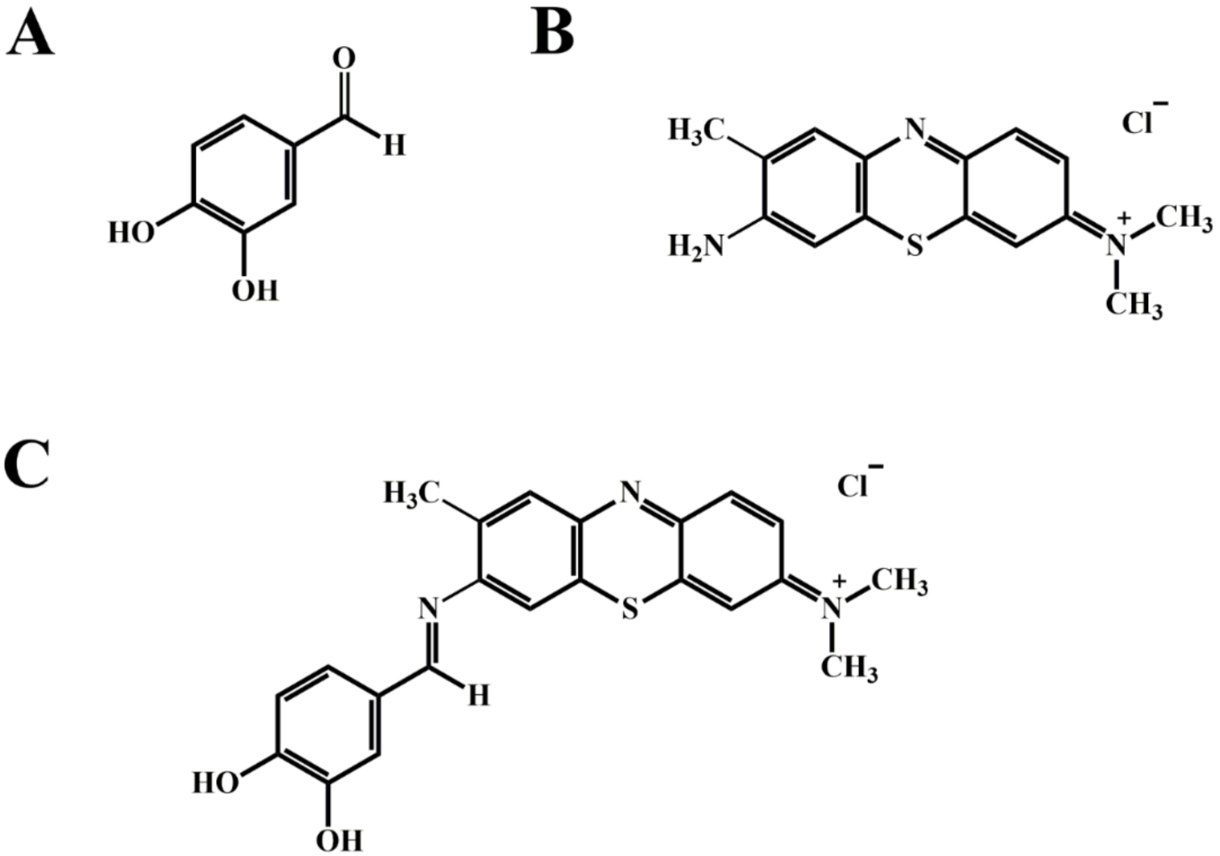

Figure 13. Chemical structures of **A** DHB **B** TDB and **C** Schiff-base product after aldehyde-amine reaction between DHB and TDB.

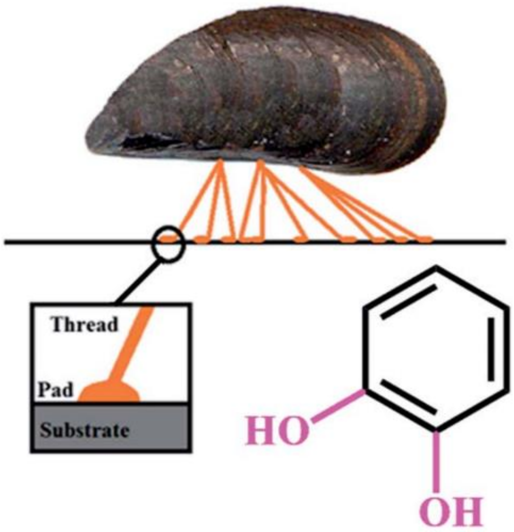

Figure 14. Schematic of mussel adsorption and chemical structure of a catechol ligand. Source: Ref. [77].

One aldehyde used in this work was 3,4-dihydrobenzaldehyde (DHB) (Figure 13A). The use of this aldehyde was inspired by dopamine – a molecule which facilitates bio-adhesion for underwater animals, such as mussels and barnacle. These animals produce mussel foot proteins (mfps) which allow them to adhere to wet, rocky underwater surfaces with immense strengths (Figure 14) [76]. The mfps have a high content of catecholic amino acids which possess a functional group called a catechol ligand (the double hydroxyl groups found on adjacent carbon atoms of one of the aromatic rings). These ligands are powerful complexing agents; previous investigations have shown that members from the catechol family can strongly adsorb onto the surfaces of oxide particles [77].

One of the CNT dispersants used in this work was Toluidine Blue O (TDB) (Figure 13B). This molecule contains an amine group, aromatic rings, as well as a positive charge. Each of these entities serve a unique purpose: the aromatic rings facilitate bonding onto the CNTs through π–π interactions [78]; the amine group reacts to form the Schiff base (Figure 13C); and the positive charge on the nitrogen atoms facilitates electrostatic dispersion of the MWCNT.

7.1.2 Characterization

As seen in Figure 15A the sizes of the synthesized particles are between 30-50 nm and are nearly uniform in morphology. The XRD pattern see in Figure 15B indicates that the sample contains the birnessite and amorphous phases of MnO_2. The peak broadening may be attributed to the small particle sizes. However, the samples also contained an amorphous phase.

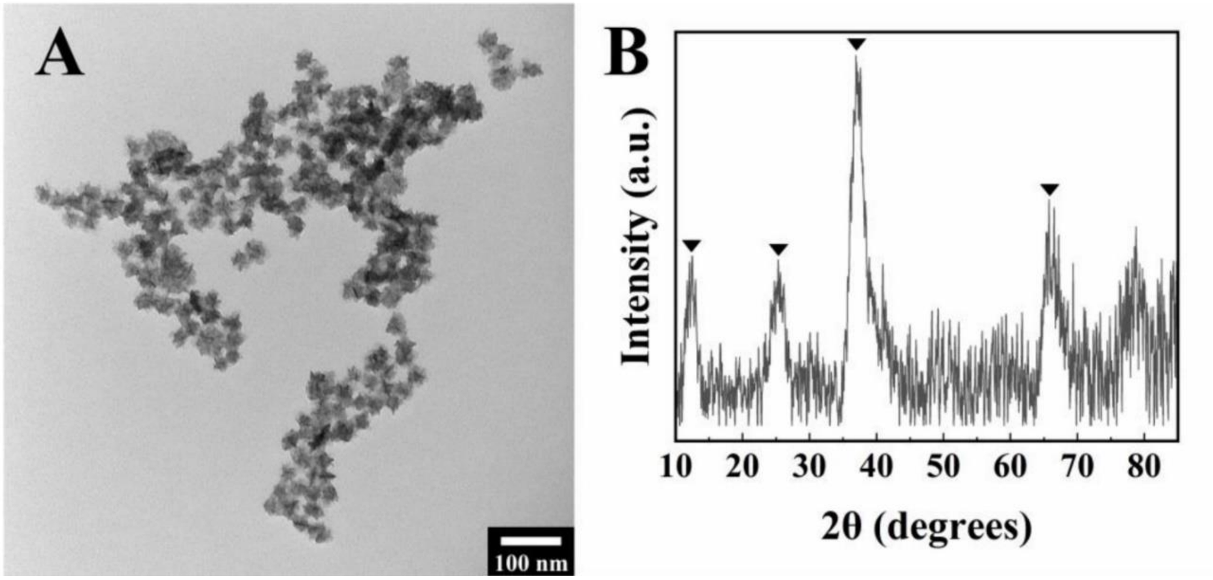

Figure 15. **A** TEM image of synthesized MnO_2 particles and **B** XRD pattern of MnO_2 (▼- JCPDS 87-1497).

7.1.3 Electrochemical Testing

Initially, an electrode with 30 mg cm^{-2} mass loading and 0.5 mm current collector thickness (referred to as E-30 henceforth) was prepared and tested to establish the baseline performance of DHB and TDB. Figure 16A shows near-ideal box shapes for CV tests for E-30 at 2 and 20 mV s^{-1} scan rates. Figure 16B shows the measured gravimetric and areal capacitance values to be 142.7 F g^{-1} and 4.3 F cm^{-2}, respectively, at a scan rate of 2 mV s^{-1}. These values gradually decreased as scan rate increased which was due to diffusion limitations of the electrolyte ions into the pores of the active material. Real and imaginary components of the complex capacitance, as well as the Nyquist plot for E-30 can be seen in Figure 17A. The Nyquist plot represented a near ideal 90° vertical line. The frequency dependencies of the real and (Figure 17B) and imaginary (Figure 17C) components of the complex capacitance plots showed a relaxation-type dispersion [79], as seen by the decline in C_s’ with increasing frequency and a maximum in the frequency dependence of C_s’’.

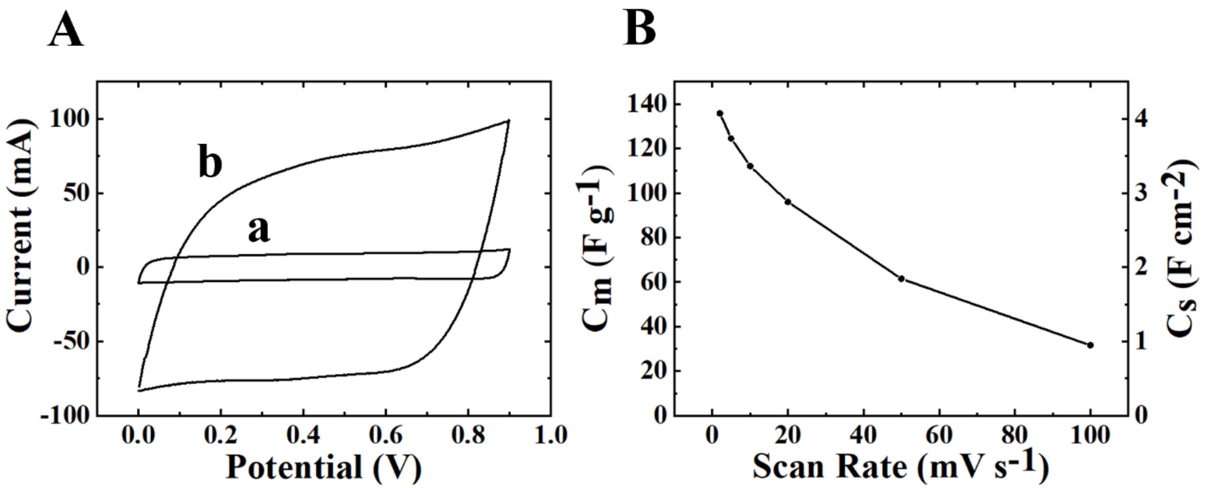

Figure 16. **A** Cyclic voltammetry at *a* 2 and *b* 20 mV s^{-1} and **B** dependencies of C_S and C_m on scan rate for MnO_2-MWCNT electrode prepared with DHB-TDB with 30 mg cm^{-2} mass loading.

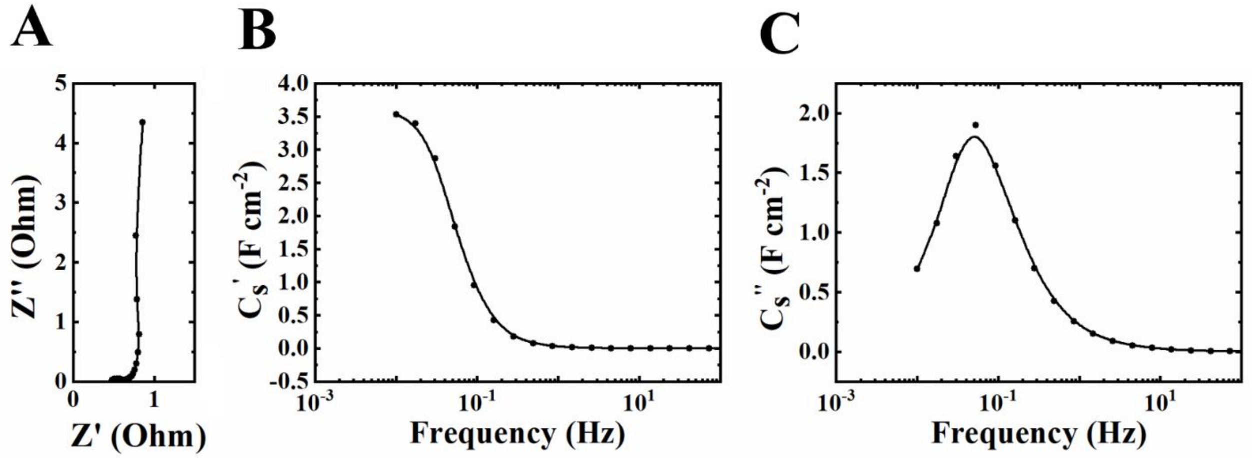

Figure 17. **A** Nyquist plot of complex impedance, **B** $C_S{}'$ and **C** $C_S{}''$ versus frequency for MnO_2-MWCNT electrode prepared with DHB-TDB with 30 mg cm^{-2} mass loading.

It is worthwhile to mention that the capacitance calculated from integrating the CV data depends on scan rate, whereas differential capacitance, C_s', depends on frequency (since an AC signal with an amplitude of 5 mV is applied). When comparing C_s and C_s' for the same time scales the C_s values are typically higher than C_s' values. (In fact, this will be the case for all the following investigation in this work as well.) The difference in differential and integral capacitances is attributed to several factors discussed in literature [80–82], such as physical heterogeneity of the electrode, poor access of ions to redox sites at low voltages, and other factors.

After testing the E-30 three more electrodes were made with the same composite by varying the mass loading to 35, 40 and 45 mg cm^{-2} (referred to as E-35, E-40, and E-45, respectively). This was done to study the impact of the mass loading on the performance of the electrode. The thickness of the current collector was varied appropriately to accommodate the mass loading for each electrode. The higher the mass loading the greater the thickness was to allow for efficient packing of the composite material within the pores of the Ni foam current

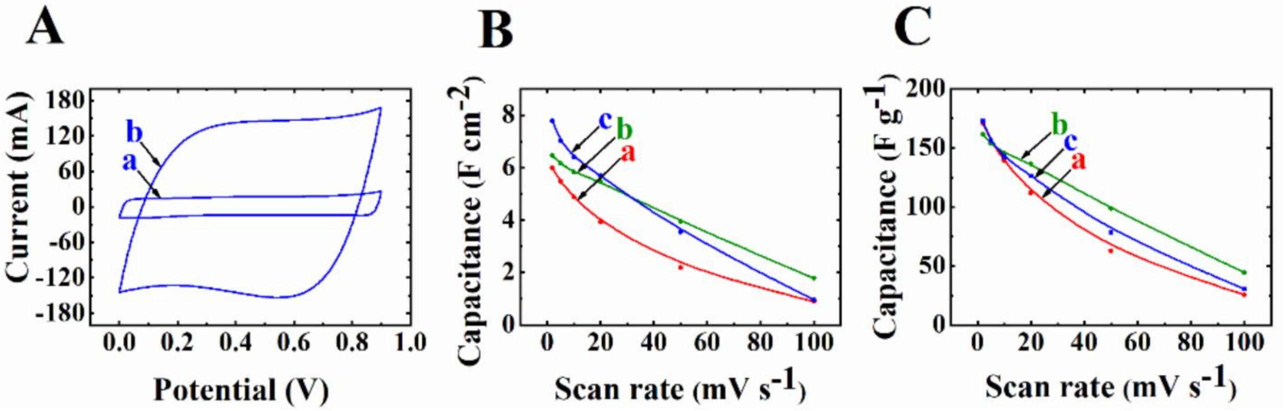

Figure 18. **A** Cyclic voltammetry at 2 and 20 mV s^{-1} for electrodes of 45 mg cm^{-2} mass loading and dependencies of **B** C_S and **C** C_m on scan rate for electrodes with mass loadings of *a* 35, *b* 40 and *c* 45 mg cm^{-2}.

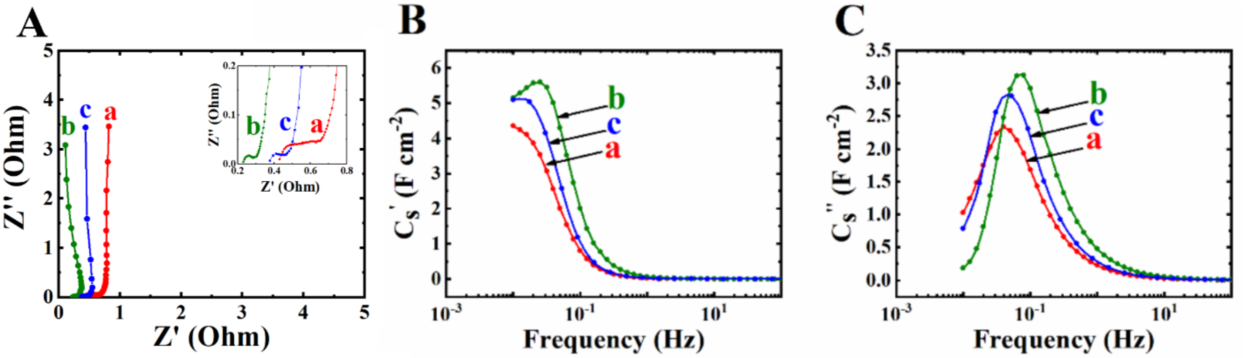

Figure 19. **A** Nyquist plots of complex impedance **B** C_S' and **C** C_S'' versus frequency for electrodes prepared with DHB-TDB composites with mass loadings of *a* 35, *b* 40 and *c* 45 mg cm^{-2}.

collector. Figure 18A shows the CV test results at 2 and 20 mV s^{-1} for E-45 to be nearly the ideal box shape. Figure 18B shows the areal capacitance dependence on scan rate for E-35, E-40, and E-45. The increase in the mass loading resulted in increased C_s at low scan rates. E-40 exhibited the highest capacitive retention compared to E-35 and E-45, whereas E-45 exhibited the highest areal capacitance of 7.8 F cm^{-2}. The poor capacitance retention of E-45 can be explained by considering the effect of the current collector thickness; the greater the thickness the more material can be packed since the pore sizes within the current collector are relatively large. It is suggested that the thickness was not optimal for E-45 which is to say that the amount of material packed was greater than what the pores of the current collector could facilitate. Figure 18C shows the gravimetric capacitance dependence on scan rate. The gravimetric capacitance was the highest for E-45 at a scan rate of 2 mV s^{-1}, whereas the gravimetric capacitive retention for E-40 was the highest out of all the electrodes. Figure 19A shows the Nyquist plots for all three electrodes. All three electrodes display low resistance and good capacitive behaviour as seen from their near 90^{o} vertical lines with the least resistance seen in E-40. The inset in Figure 19A shows that E-40 possess the lowest charge transfer resistance, as well as the lowest electrolyte resistance. Figure 19B and Figure 19C show the frequency dependencies of the capacitance to be attributed to a relaxation-type dispersion [79]. E-40 possessed the highest maximum capacitance from the impedance testing, but the relaxation frequency (the frequency at the maximum) did not change significantly between the three electrodes. E-35 exhibited the highest resistance as seen in its Nyquist plot (Figure 19A) which correlated with it having the lowest complex capacitance.

For another portion of this investigation, dopamine hydrochloride (DOPA-HCl) and 4-Formylbenzene-1,3-disulfonic acid disodium salt hydrate (FDS) were used to acquire the

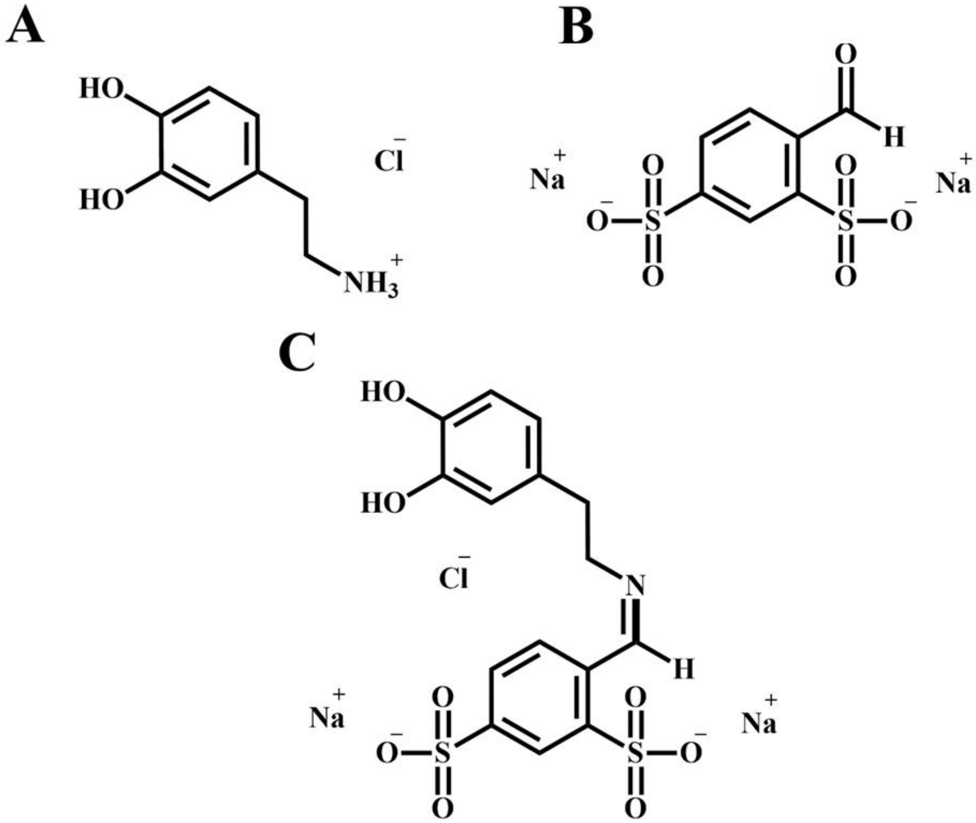

Figure 20. Chemical structures of **A** DOPA-HCl **B** FDS and **C** Schiff-base product after amine-aldehyde reaction between DOPA-HCl and FDS.

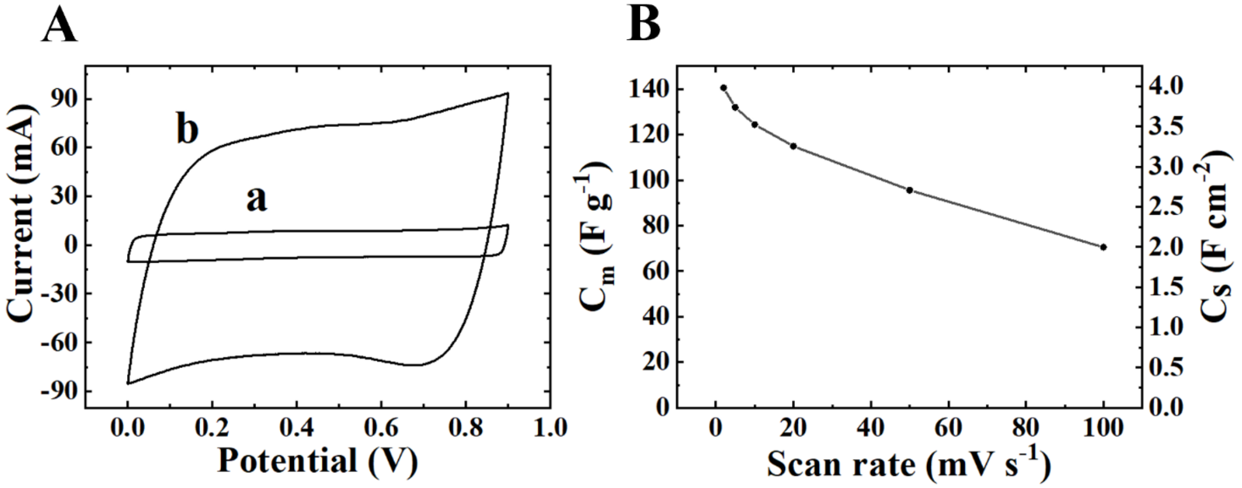

Figure 21. **A** CV testing at (a) 2 mV s^{-1} and (b) 20 mV s^{-} of electrode for composite prepared with DOPA-HCl and FDS with 30 mg cm^{-2} mass loading **B** gravimetric and areal dependence on scan rate.

Schiff-base imine product. Their chemical structures seen in Figure 20A and Figure 20B are similar to the structures of DHB and TDB. DOPA-HCl was used for modification of MnO_2. Its adsorption involved bonding of the catechol group to the Mn atoms on the particle surfaces. FDS is an aldehyde molecule which was adsorbed on the MWCNT by π-π interactions. The amino group of DOPA-HCl and the aldehyde group of FDS reacted in a Schiff-base reaction to form an imine (Figure 20C). This promoted the heterocoagulation and improved mixing of MnO_2 and MWCNT. Furthermore, the charge-to-mass ratio of FDS is greater than TDB which was theorized to improve CNT dispersion and thus the capacitive performance. An electrode was fabricated with the same 30 mg cm^{-2} mass loading and 0.5 mm current collector thickness to

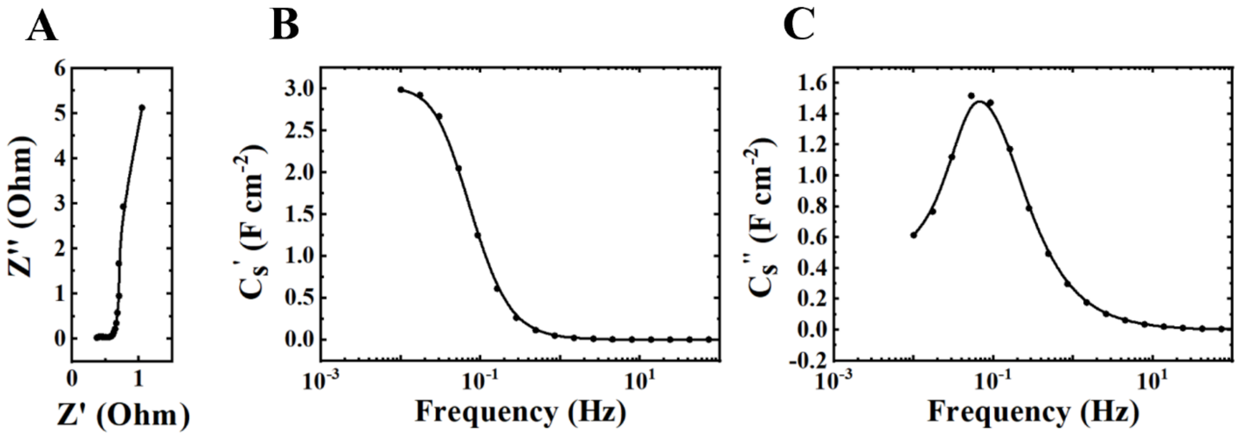

Figure 22. **A** Nyquist plot of electrode for composite prepared with DOPA-HCl and FDS with 30 mg cm^{-2} mass loading **B** C_s' and **C** C_s'' versus frequency.

compare the performance of the two pairs of materials. Figure 21A shows the CV curves for this electrode at scans of 2 and 20 mV s^{-1}. As was the case with the electrodes prepared with DHB-TDB the voltammograms are nearly rectangular in shape indicating good capacitive behaviour. However, the capacitive retention for the DOPA·HCl-FDS (seen in Figure 21B) electrode is higher; the electrode prepared with DOPA·HCl-FDS retained a capacitance of ~2.0 F cm^{-2} compared to ~1.0 F cm^{-2} from the one prepared with DHB-TDB.

Figure 22A shows the Nyquist plot constructed from the impedance testing for the DOPA·HCl-FDS electrode. The imaginary component of the impedance reaches a maximum of 5 ohms as compared to 4.5 ohms for the previous electrode. The real and imaginary components of the complex impedance (Figure 22B and Figure 22C, respectively) showed a relaxation-type behavior, albeit with a lower maximum seen in C_s'' – approximately 1.6 F cm^{-2}.

An asymmetrical device was constructed with MnO_2-MWCNT as the positive electrode (31 mg mass loading over a 1.5 cm^2 current collector area) and an activated carbon-carbon black (51.7 mg mass loading over a 3 cm^2 current collector area) negative electrode. The MnO_2-CNT composite used for the fabrication of this device was prepared using TDB as the CNT dispersant and DHB as the MnO_2 complexing agent. This device was made primarily to gain experience in device fabrication, but also to test the performance of TDB and DHB when used in the complete fabrication of a device.

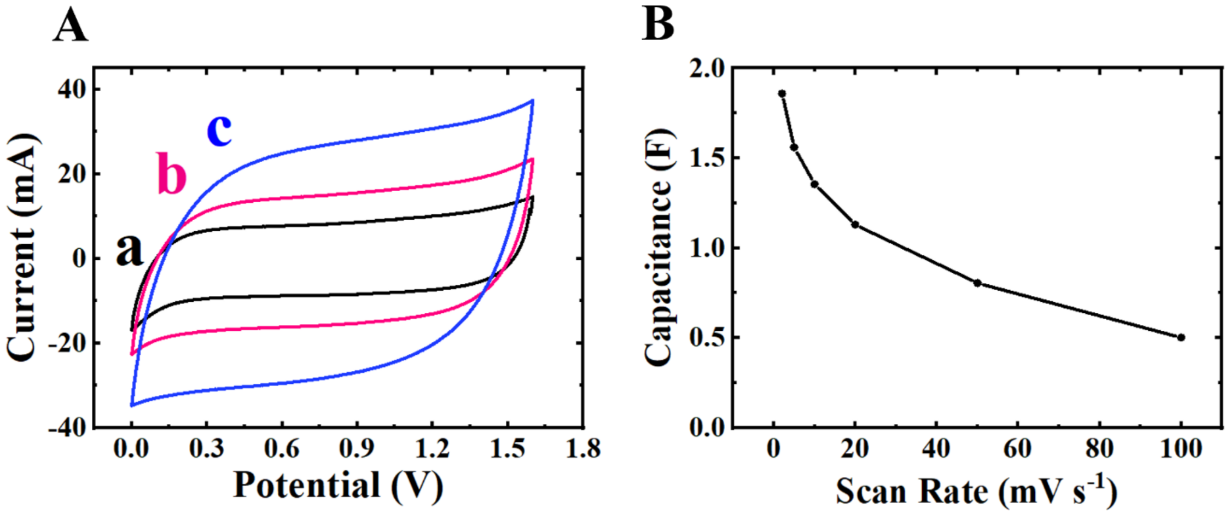

Figure 23. **A** CVs at scan rates of a 5 mV s^{-1}, b 10 mV s^{-1}, and c 20 mV s^{-1} and **B** capacitance versus scan rate for asymmetric device prepared with MnO_2-MWCNT composite for positive electrode and activated carbon-carbon black for negative electrode.

Figure 23A show the CV curves at scan rates 5, 10 and 20 mV s^{-1} for a 1.6 V voltage window are close to the ideal box shape and increase in current with increasing scan rate indicating good capacitive behaviour. The capacitance was 1.86 F (Figure 23B) at a scan rate of 2 mV s^{-2} and decreased to 0.5 F at 100 mV s^{-1} yielding a retention of 27%. The charge-discharge curves seen in Figure 24A were of symmetric, triangular shape for a voltage window of 1.6 V. The capacitance, calculated from the discharge data (Figure 24B), decreased from 2.0 to 1.8 F with increasing discharge current from 3 to 10 mA.

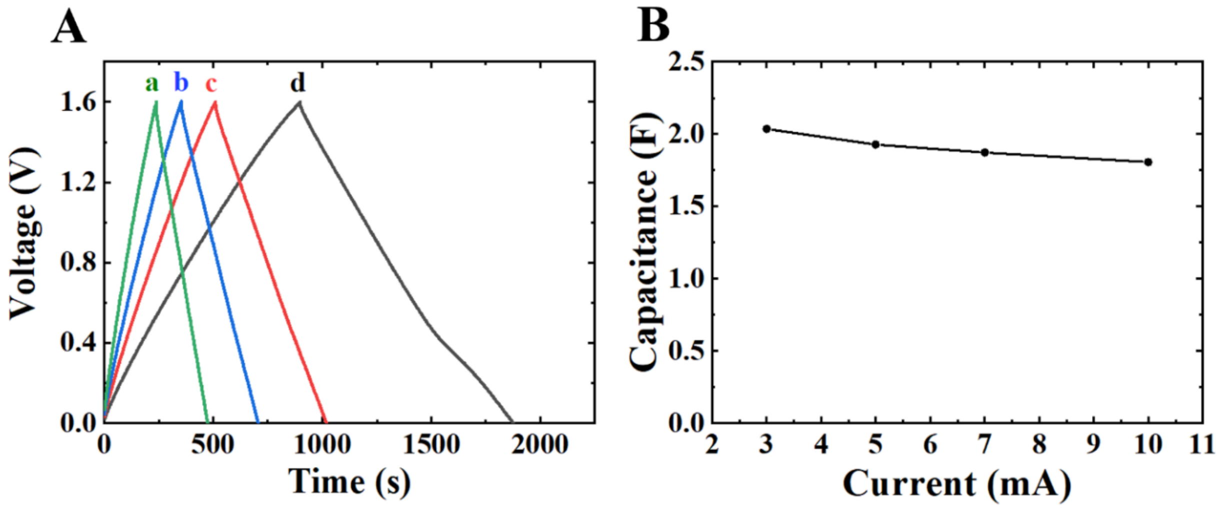

Figure 24. **A** Charge-discharge behaviour at currents of *a* 9 mA, *b* 7 mA, *c* 5 mA, and *d* 3 mA **B** Capacitance versus discharge current plot constructed from charge-discharge data for asymmetric device prepared with MnO_2-MWCNT composite for positive electrode and activated carbon-carbon black for negative electrode.

7.1.4 Conclusion

MnO_2-MWCNT electrodes with 30-45 mg cm^2 mass loading were prepared using DHB and TDB dispersants. The aromatic rings of TDB governed its adsorption onto the MWCNTs via π- π stacking, while the catechol ligand of DHB allowed for effective adsorption onto the MnO_2 particles surfaces. The aldehyde group of DHB bonded with the amine group of TDB to form a Schiff-base, thereby facilitating good mixing. The electrodes were tested with cyclic voltammetry and EIS. E-45 displayed the highest areal capacitance of 7.8 F cm^{-2} at a scan rate of 2 mV s^{-1} along with low electrode resistance. An asymmetric device with a MnO_2-MWCNT positive electrode prepared with DHB-TDB and an activated carbon-carbon black negative electrode was tested with CV and charge-discharge testing. The device held a retention of 27% up to 100 mV s^{-1} for CV testing and 90% retention up to 10 mA current for charge-discharge testing.

A separate electrode with 30 mg cm^{-2} mass loading was prepared with a composite of DOPA-HCl and FDS as the MnO_2 and MWCNT dispersants, respectively. The electrode displayed better capacitance retention but increased impedance in the imaginary component of the Nyquist plot. The composite materials used in this investigation are promising candidates for future SC applications.

7.2 Co-dispersion Approach (MnO_2-MWCNT)

7.2.1 Background

The co-dispersion approach is unlike the Schiff base linkage mechanism in that a single molecule provides a dual role for both constituents (MnO_2 and MWCNT) simultaneously. The co-dispersant used for this work was gallocyanine (GC). As seen in its molecular structure in Figure 25 GC possesses three aromatic rings, a positive charge, and a catechol ligand. The molecular structure of GC has the unique ability of being able to serve three functions simultaneously: (1) It adsorbs onto the surfaces of MWCNTs with its aromatic rings through π–π interactions; (2) its positive charge impart like-charges on the MWCNTs to facilitate electrostatic dispersion; (3) its catechol ligand adsorbs onto the surfaces of the MnO_2 particles and charges them to facilitate dispersion. Functions (1) and (2) jointly contribute to a process referred to as the "unzipping" mechanism [83,84]. During this unzipping process small gaps form at the bundle ends of undispersed MWCNTs, thereby allowing for the insertion of small organic dyes (such as TDB or GC) which can diffuse along the length of the bundled MWCNTs and unzip them. The electrostatic dispersion facilitates this unzipping and maintains the separation distance between individual MWCNTs.

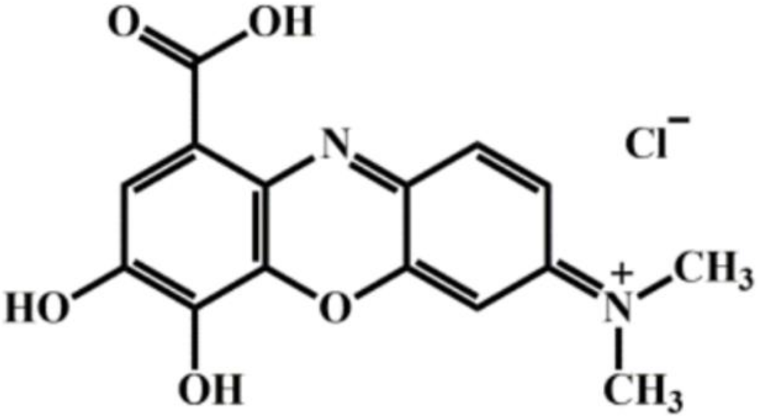

Figure 25. Chemical structure of co-dispersant gallocyanine (GC).

7.2.2 Characterization

The MnO_2 particles used for this investigation were identical to those used for the Schiff-base mechanism (please refer to Section 7.1.2 Characterization).

7.2.3 Electrochemical Testing

A MnO_2-MWCNT electrode with 30 mg cm^{-2} mass loading was prepared with GC as a co-dispersant. Cyclic voltammetry and EIS testing were conducted to test its electrochemical performance. Figure 26A shows CV results at 2 and 20 mV s^{-1}. The near-rectangular voltammograms exhibit mirror image cathodic and anodic parts suggesting ideal capacitive behavior of the electrode. Figure 26B shows the scan rate dependence on the areal and gravimetric capacitance. Starting at 2 mV s^{-1} the gravimetric and areal capacitances were 135.7 F g^{-1} and 4.2 F cm^{-2}, respectively. These values gradually declined with increasing scan rate due to the decreased diffusion of electrolyte species into the pores of the active material. In addition, the capacitive retention was calculated to be 23% at a scan rate of 100 mV s^{-1}. Figure 27A shows the Nyquist plot attained with EIS testing and the slope of its vertical line is nearly 90° indicating capacitive behaviour. The real (Figure 27B) and imaginary (Figure 27C) components of complex differential capacitance were calculated from the impedance data.

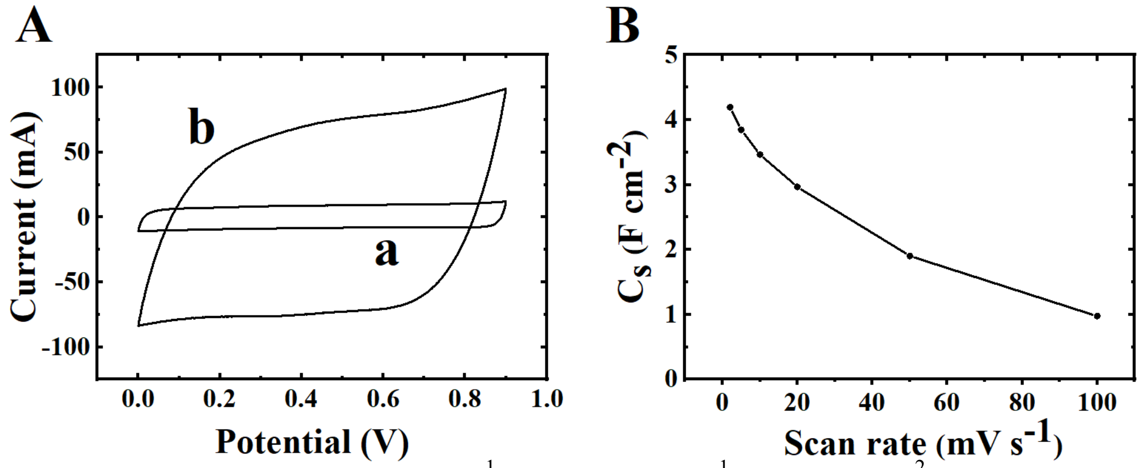

Figure 26. **A** CV testing at (a) 2 mV s^{-1} and (b) 20 mV s^{-1} for 30 mg cm^{-2} mass loading electrode prepared using co-dispersion approach with GC **B** gravimetric and areal dependence on scan rate.

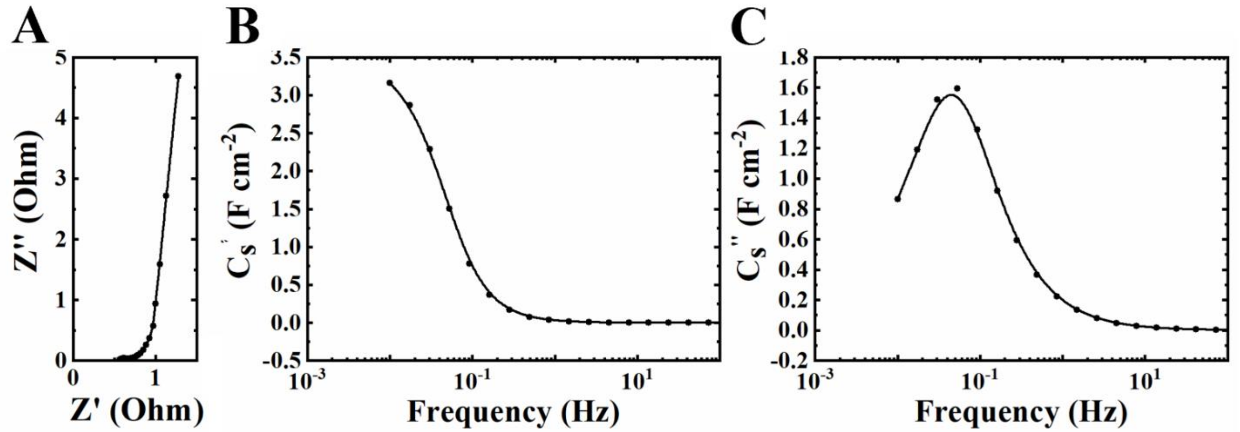

Figure 27. **A** Nyquist plot of electrode with 30 mg cm^{-2} mass loading prepared using co-dispersion approach with GC. **B** C_s' and **C** C_s'' versus frequency.

The frequency dependencies of the capacitance showed a relaxation-type dispersion, as indicated from the decline in capacitance in the real part, C_s', and the corresponding relaxation maxima seen in the imaginary part, C_s''.

7.2.4 Conclusion

Gallocyanine was employed as a co-dispersant for the dual role of adsorbing onto the surfaces of MnO_2 particles and MWCNTs to facilitate good mixing and dispersion. A 30 mg cm^{-2} electrode was fabricated and tested with CV and EIS. The highest areal capacitance was 4.2 F cm^{-2} at a scan rate of 2 mV s^{-1}. The capacitive retention at 100 mV s^{-1} scan rate was recorded to be 23%. The slope of the Nyquist plot was nearly 90° which indicated good capacitive behaviour and low resistance (R=Z') was obtained. The results of the analysis of impedance data, coupled with CV data indicated that good electrochemical performance was achieved at high mass loading.

7.3 Liquid-Liquid Extraction Approach (MnO_2-MWCNT)

7.3.1 Background

Particle extraction through liquid-liquid interface (PELLI) is another colloidal technique used to avoid the agglomeration problem of MnO_2. In typical PELLI techniques the MnO_2 particles are synthesized in an aqueous solution followed by the addition of an immiscible organic solvent. Extractor molecules are then dissolved in the organic solvent orienting themselves accordingly at the interface due to their hydrophobic tails and hydrophilic heads. The surfactant molecules change the surface properties of the particles from hydrophilic to hydrophobic, thereby providing the wetting of the particles by the organic phase. Upon agitation

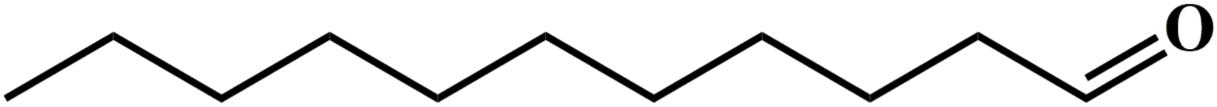

Figure 28. Molecular structure of undecanal.

of the solution the particles extract out from the aqueous phase and transfer into the organic phase. This extraction technique works for metals, oxides, hydroxides, and quantum dots [85–88].

The novelty in the PELLI investigation for this work is that a single material (undecanal) was used to serve as the particle-receiving medium, as well as the vehicle for particle phase transfer. This dual-role nature of undecanal (UD) eliminated the need for long-chain extractor molecules which need to be removed from the organic phase post-extraction. The molecular structure of UD (Figure 28) possesses an aryl group, as well as an aldehyde group at the end of its 11-carbon chain. UD was able to extract MWCNTs through adsorption of its aryl group onto

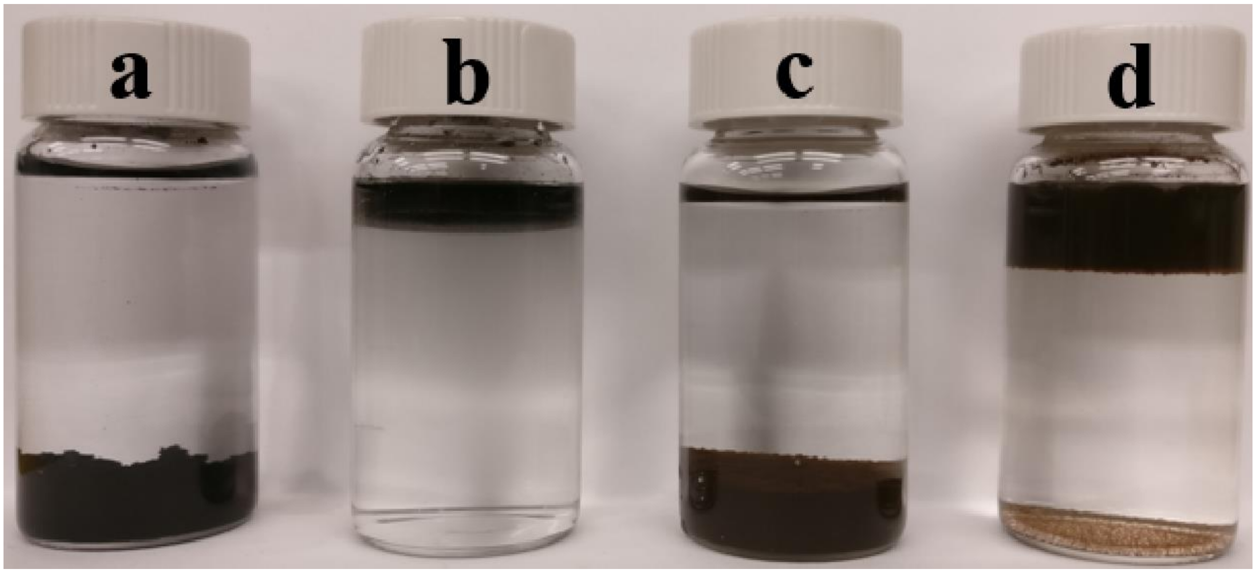

Figure 29. **a** unextracted MWCNTs in an aqueous suspension **b** bottom-up extraction of MWCNTs with undecanal **c** unextracted MnO_2 particles in an aqueous suspension **d** bottom-up extraction of MnO_2 particles with undecanal.

the hydrophobic walls of MWCNT (Figure 29a and Figure 29b). UD was also found to extract MnO_2 particles (Figure 29c and Figure 29d). It is suggested that its adsorption onto MnO_2 particles was induced by the interaction of the aldehyde oxygen atom. Specifically, the lone pair of this carbonyl oxygen may have allowed for effective coordination between the oxide surface and the aldehyde, as has been the case with Zn and Ti oxides [89–90]. Alternatively, the adsorption of the aldehyde could have also been based on H-bonding involving OH groups on the oxide particle surfaces [91].

7.3.3 Electrochemical Testing

A MnO_2-MWCNT electrode with 40 mg cm^{-2} mass loading was fabricated using undecanal with the modified LLE (liquid-liquid extraction) technique. CV, EIS, and galvanostatic charge-discharge testing was conducted. Figure 30A shows the CV test results at 2, 5, and 10 mV s^{-1} to be near ideal-box shape. Figure 30B displays the capacitances which were calculated from the CV test data at different scan rates. There is a gradual decrease in the

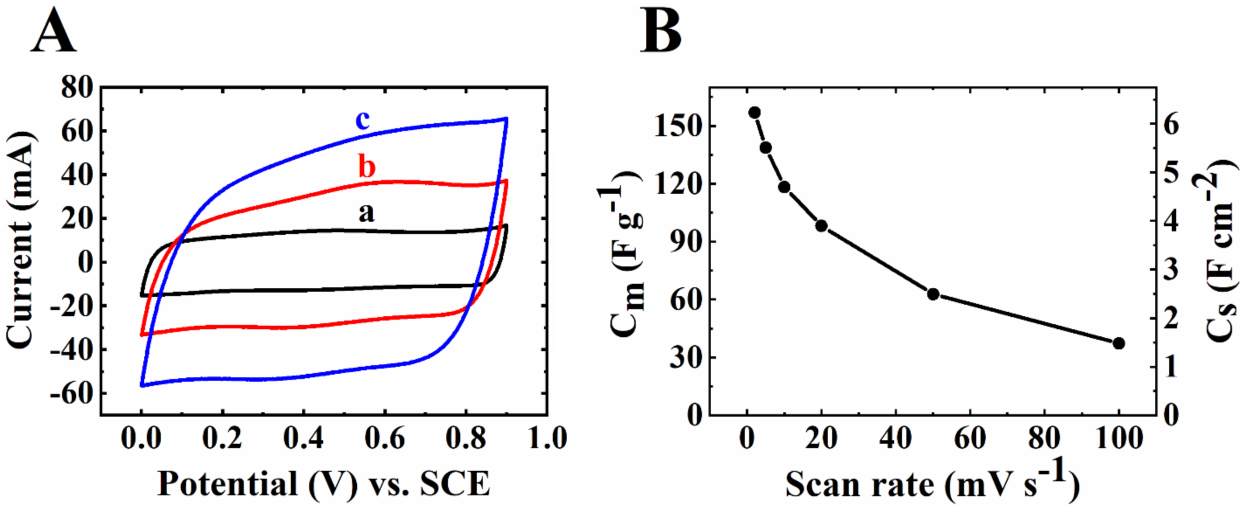

Figure 30. **A** CV data at scan rate of *a* 2, *b* 5, and *c* 10 mV s^{-1} and **B** mass and areal capacitance versus scan rate for MnO_2-MWCNT electrode with 40 mg cm^{-2} mass loading prepared with UD and modified LLE technique.

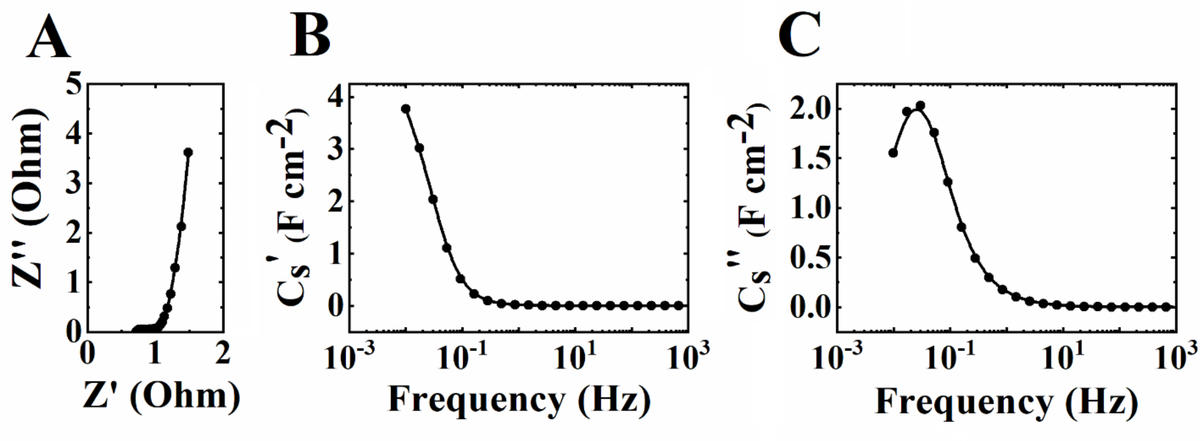

Figure 31. **A** Nyquist plot of complex impedance and **B**, **C** Frequency dependencies of C'$_S$ and C"$_S$ calculated from the impedance data for MnO_2-MWCNT electrode with 40 mg cm^{-2} mass loading prepared with UD and modified LLE technique.

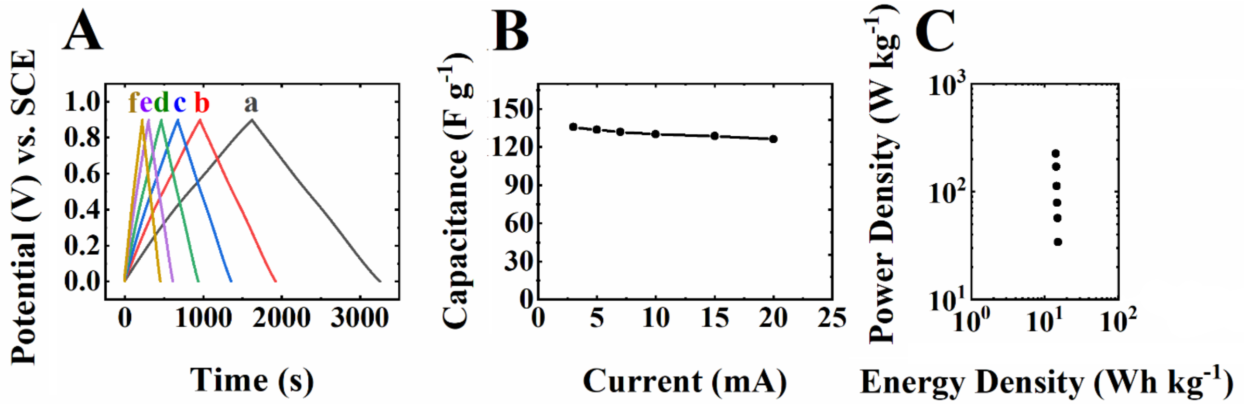

Figure 32. **A** Charge-discharge behaviour at currents of *a* 3 *b* 5 *c* 7 *d* 10 *e* 15 and *f* 20 mA **B** capacitance versus current and **C** Ragone plot constructed from charge-discharge test data for MnO_2-MWCNT electrode with 40 mg cm^{-2} mass loading prepared using UD with modified LLE technique.

gravimetric/areal capacitance with increased scan rate indicating diffusion limitations of the electrolyte species within the porous structure of the composite. However, a gravimetric capacitance of 157 F g^{-1} and an areal capacitance of 6.3 F cm^{-2} was achieved at 2 mV s^{-1}. These values are comparable to what was achieved with the Schiff-base and co-dispersion approaches using electrodes of the same mass loading. Figure 31A shows the Nyquist plot obtained from EIS data; the vertical segment is close to the ideal 90° indicating capacitive behaviour and low resistance. Figure 31B and Figure 31C show real and imaginary components of the complex capacitance, respectively. A gradual decline in C_s' with increasing frequency and a maximum in C_s'' indicates a relaxation-type dispersion. Figure 32A illustrates the charge-discharge data; the curves were of the desired symmetrical triangular shape in the voltage window of 0-0.9 V. Figure 32B shows the capacitance plot calculated from the charge- discharge data; the gravimetric capacitance dropped from 136 to 126 F g^{-1} with increasing currents from 3 to 20 mA. A Ragone plot (Figure 32C) was also constructed from the charge-discharge data. The highest obtained energy density was 15.3 Wh kg^{-1} at a power density of 33.8 W kg^{-1} and the highest obtained power density was 225 W kg^{-1} at an energy density of 14.2 Wh kg^{-1}.

7.3.4 Conclusion

A MnO_2-MWCNT electrode with a mass loading of 40 mg cm^{-2} was prepared using a conceptually new LLE technique. UD served as both the extracting agent and the receiving solvent, thereby eliminating the need for long-chain extractor molecules. Gravimetric and areal capacitances of 157 F g^{-1} and 6.2 F cm^{-2} were achieved at a scan rate of 2 mV s^{-1}. Charge-discharge test data showed good symmetrical, triangular shapes and the calculated capacitance fell 7% with increasing current from 3 to 20 mA. The discovery of this novel material opens an unexplored field of dual-role materials for developments in PELLI investigations and SC applications.

7.4 Comparison of electrodes developed by Schiff-base, co-dispersion, and Liquid-Liquid Extraction Techniques

It would now benefit to compare all three colloidal processing techniques developed for the fabrication of MnO_2-MWCNT composites. Note, since two pairs of materials were investigated for the Schiff-base technique (DOPA·HCl-FDS and DHB-TDB) only DHB-TDB will be selected since the purpose of this section is to compare the colloidal techniques – not materials within each technique. As a reminder for the reader, the dye/extractor for each of these techniques were: DHB-TDB for Schiff-base (referred to as E-SB); GC for co-dispersion (E-CD); and UD for LLE (E-LLE). The compared electrodes each had a mass loading of 40 mg cm^{-2} for the purposes of consistency.

Figure 33A illustrates a comparison of the CV test results at 20 mV s^{-1} for E-LLE, E-CD, and E-SB. The voltammograms for E-LLE are the smallest in size yielding an areal capacitance of 3.9 F cm^{-2}, compared to 5.5 and 4.9 F cm^{-2} achieved E-SB and E-CD, respectively. Figure 33Bshows a comparison of the scan rate dependence on gravimetric and areal capacitance for E-LLE, E-CD, and E-SB. The best capacitive retention was achieved by E-SB – exhibiting a capacitive retention of 27%.

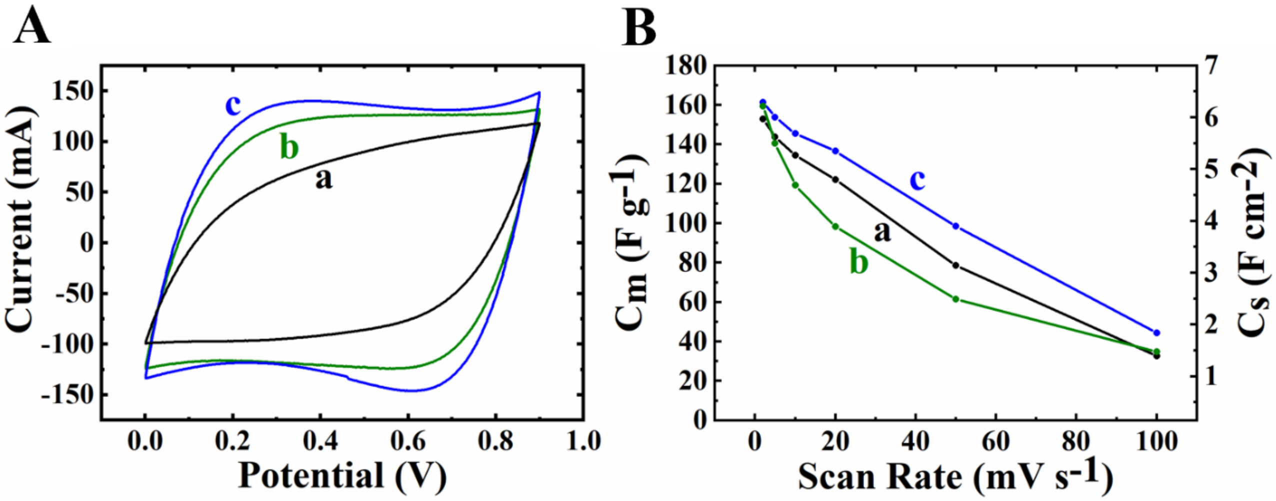

Figure 33. **A** CV tests at 20 mV s^{-1} scan rate and **B** dependence of gravimetric and areal capacitance for *a* E-LLE, *b* E-CD, and *c* E-SB.

Figure 34A shows the Nyquist plots obtained through EIS data for E-LLE, E-CD, and E-SB. E-LLE exhibited the highest real and imaginary impedance, whereas the E-SB exhibited the lowest real and imaginary impedance. The real and imaginary components of complex differential capacitance for E-LLE, E-CD, and E-SB is displayed in Figure 34B and Figure 34C, respectively. The decline in C_s' for the E-LLE starts at an earlier frequency compared to the other two electrodes. Accordingly, its relaxation frequency at the maximum C_s'' value is also the lowest out of the three electrodes (seen in Figure 34C). In contrast, the real and imaginary complex capacitance curves for E-SB are the best in performance out of the three electrodes. Its relaxation frequency was the greatest indicating that it had the shortest time constant.

In summary, E-SB displayed overall better electrochemical performance compared to E-CD and E-LLE. However, this comparison does not attempt to broadly categorize the superiority of either of the three colloidal techniques. Rather, the approach combined *with* the specific material is what is being compared. That is to say that although the co-dispersion approach with DHB-TDB is seen to perform better, it can be only be said when compared to the co-dispersion approach *with* GC and the LLE technique *with* UD.

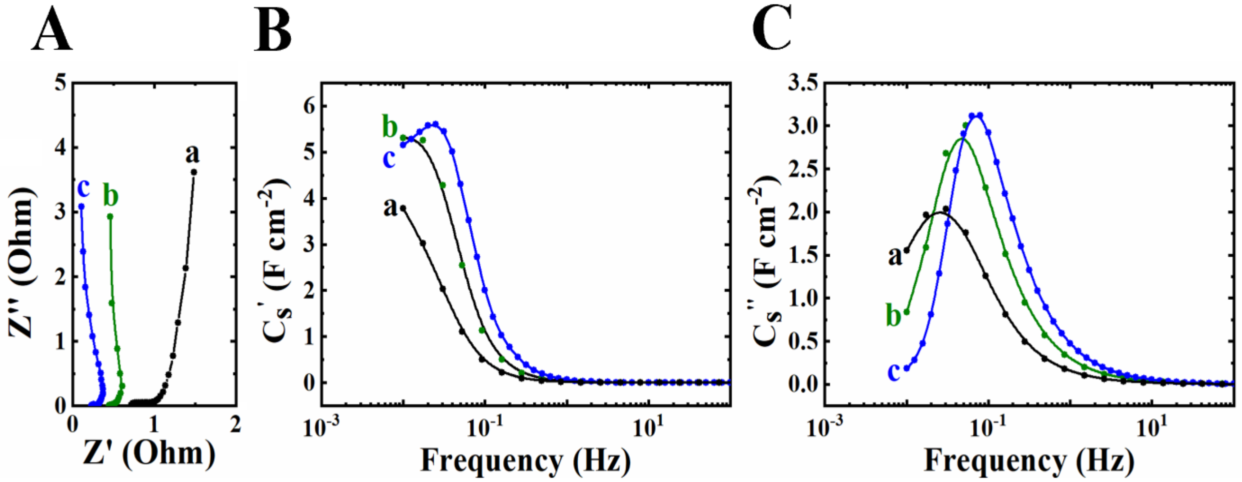

Figure 34. **A** Nyquist plot of complex impedance for electrodes of 40 mg cm^{-2} mass loading prepared with (a) modified LLE technique using UD (b) co-dispersion using GV and (c) Schiff-base linkage using DHB and TDB.

E-LLE gave the lowest performance, but as stated earlier, the discovery of UD opens the doors to an entirely new realm of materials exhibiting a dual-natured role (as extractor and receiving solvent) for PELLI techniques. Nevertheless, the aim of investigating each of these techniques with novel materials was the same: develop MnO_2-MWCNT composites for the fabrication of advanced supercapacitor electrodes with high capacitance, good capacitive retention at high scan rates, along with high mass loading values (> 10 mg cm^{-2}).

7.5 Morphology Modification Approach (MnO_2-MWCNT)

7.5.1 Background

One-dimensional metal oxide nanostructures have gained interest due to their potential in the development of electrochemical energy storage devices, solar energy storage and transmission devices, sensors, and optoelectronics [92]. Synthesizing these 1D nanostructures have been successful through additive-free methods such as, the reflux route [93], the wet chemical method [94], thermal decomposition, and hydrothermal synthesis [95]. However, current literature lacks an understanding of how advanced dispersants can facilitate the performance of 1D morphologies – namely, in SC applications.

Poor dispersion of 1D nanostructure can lower their surface area and weaken their electrochemical performance. There are many organic additives and/or templates which can successfully control the nucleation, growth, alignment, and dispersion of inorganic materials, but limited literature exists in understanding this effect in the context of nanomorphologies – particularly MnO_2 nanorods.

For this work, a novel hydrothermal method was developed to fabricate crystalline and dispersed MnO_2 nanorods composited with MWCNTs using lauryl gallate (LG), TDB, and GC. For the first portion, LG was used as a co-dispersant for MnO_2 nanorods and MWCNTs. LG brings several functional properties making it a useful material for many applications. LG is known to be a dispersant [96–97] and capping agent [98] for use in colloidal processing techniques. It also possesses certain biological characteristics such as anticancer, antioxidant, antifungal, and antibacterial properties [99–102] . The unique molecular structure of LG (Figure 35) contains phenolic OH groups which allow for catecholate-type bonding with the surfaces of inorganic nanoparticles [77]. In addition, previous work [103] has shown that the hydrocarbon tail of LG can allow for its adsorption onto MWCNTs.

For the second portion, TDB (Figure 13A) and GC (Figure 25) were employed as dispersants. Electrodes of 30 mg cm^{-2} mass loading were fabricated from the composites (referred to as E-TDB and E-GC for TDB and GC, respectively). As mentioned in the previous sections, TDB forms a Schiff base with DHB. However, TDB by itself may also adsorb onto the surfaces of the nanorods since NH_2 groups (which it possesses) can form stable chelates with transition metal oxides [104–105]. GC – like LG – is a co-dispersant for MWCNTs and MnO_2 and was also studied for this part of the investigation to see if it could offer better dispersion electrochemical performance over the Schiff-base method.

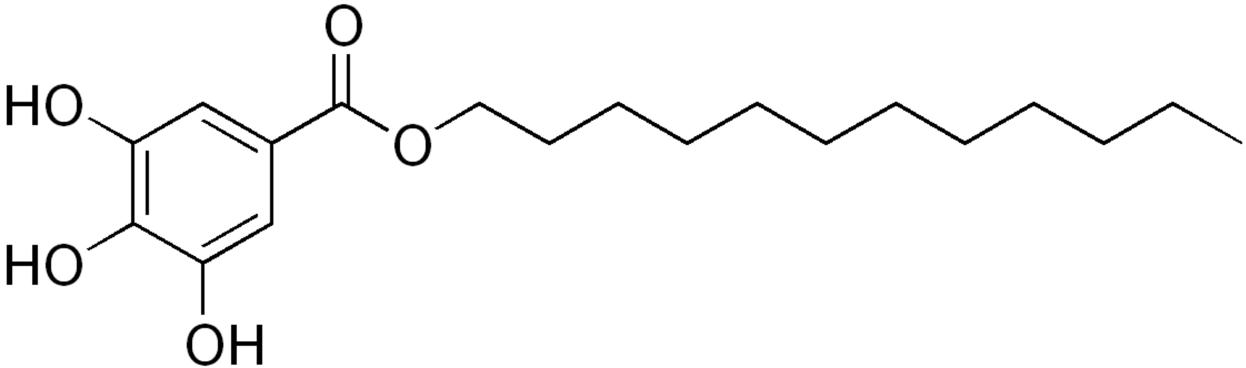

Figure 35. Molecular structure of LG.

7.5.2 Characterization

Initially, MnO_2 nanorod structures were synthesized without the addition of any additives to obtain a reference sample (Figure 36A). As expected, large amounts of agglomeration were evident. Figure 36B shows the sample of MnO_2 nanorod structures which were obtained by adding LG dispersant during synthesis. There was no noticeable difference in the dispersion or the sizes of the nanorods between these two samples. Figure 36C and Figure 36D show the

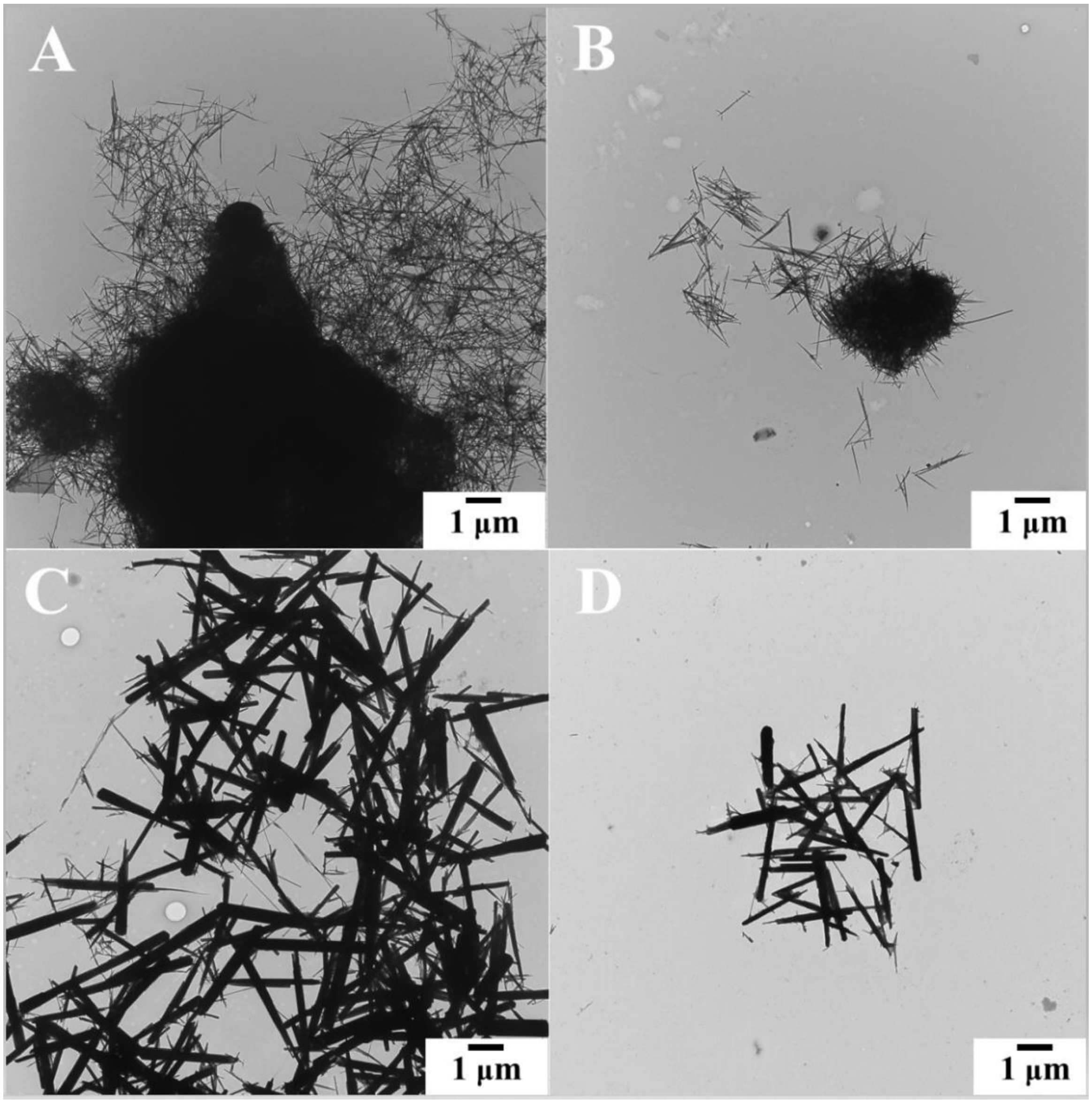

Figure 36. TEM images at 10,000X magnification of MnO_2 nanorods prepared with **A** no additive **B** LG **C** TDB and **D** GC.

nanorods prepared with the addition of TDB and GC dispersant, respectively. In both these cases the aspect ratio of the nanorods was largely increased and the dispersion was enhanced. Although, the decreased aspect ratio was opposite to what was expected. To comprehend this, it is suggested that the TDB molecules adsorbed equally on all planes of the MnO_2 which led to equal growth in all directions. In contrast, some molecules preferentially adsorb onto specific planes of the particles leading to preferential growth in one direction thereby increasing the aspect ratio.

7.5.3 Electrochemical Testing

An electrode (referred to as E-LG) with 30 mg cm^{-2} mass loading was fabricated using LG as a dispersant for the MnO_2-MWCNT composite. CV and EIS testing were conducted to study the electrochemical performance of this electrode. The CV curves obtained at 2 and 20 mV s^{-1} are displayed in Figure 37A. They show near-ideal box shapes which can be attributed to high intrinsic electrical conductivity and good kinetic reversibility. Figure 37B shows the scan rate dependence on the gravimetric and areal capacitance. The gravimetric capacitance was measured

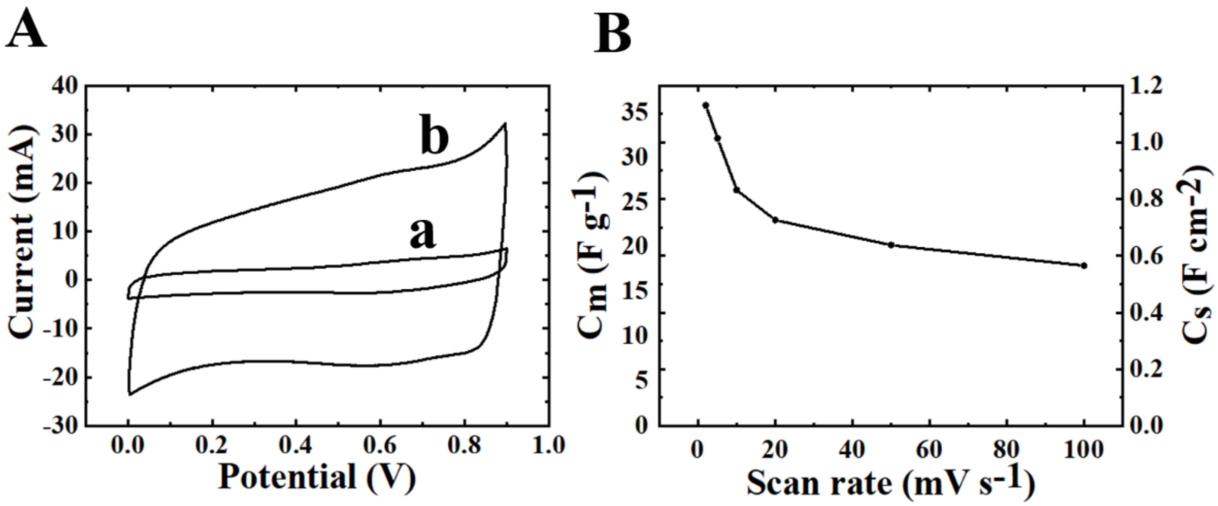

Figure 37. **A** CV curves for scan rates *a* 2 and *b* 20 mV s^{-1} and **B** gravimetric and areal capacitance dependence on scan rate for E-LG.

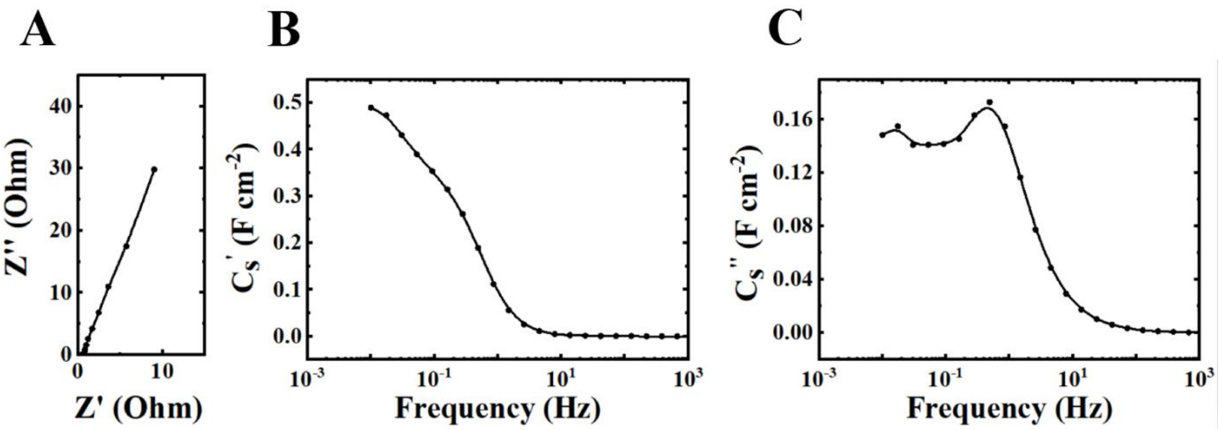

Figure 38. **A** Nyquist plot of complex impedance and frequency dependencies of **B** C_s' and **C** C_s'' calculated from the impedance data for E-LG.

at 35.7 F g^{-1} at 2 mV s^{-1} and 17.5 F g^{-1} at 100 mV s^{-1} yielding a relatively high retention of 50%. The gradual decrease in the capacitance can be attributed to the intercalation/de-intercalation of the electrolyte species in and out of the electrode. At lower scan rates, the electrolyte species can access the outer surfaces of the electrode and the interior cavities thus yielding a high capacitance. But, at higher scan rates they can only access the outer surfaces of the electrode thus yielding a lower capacitance. EIS data was used to construct the Nyquist plot displayed in Figure 38A. The relatively high electrode resistance could be due to poor mixing between the MWCNT and MnO_2 nanorods. Though, the slope of the vertical segment is greater than 45° indicating that the diffusion of the electrolyte ions is not rate-limiting. The real (Figure 38B) and imaginary (Figure 38C) components of complex capacitance were calculated from the EIS data and are seen to be relatively low. However, the relaxation frequency of the maximum C_s'' value is greater than what was achieved for electrodes of the other investigated approaches. It is desirable to have the relaxation frequency to be as high as possible as it is characteristic of the time constant, that is, how fast the system can charge/discharge.

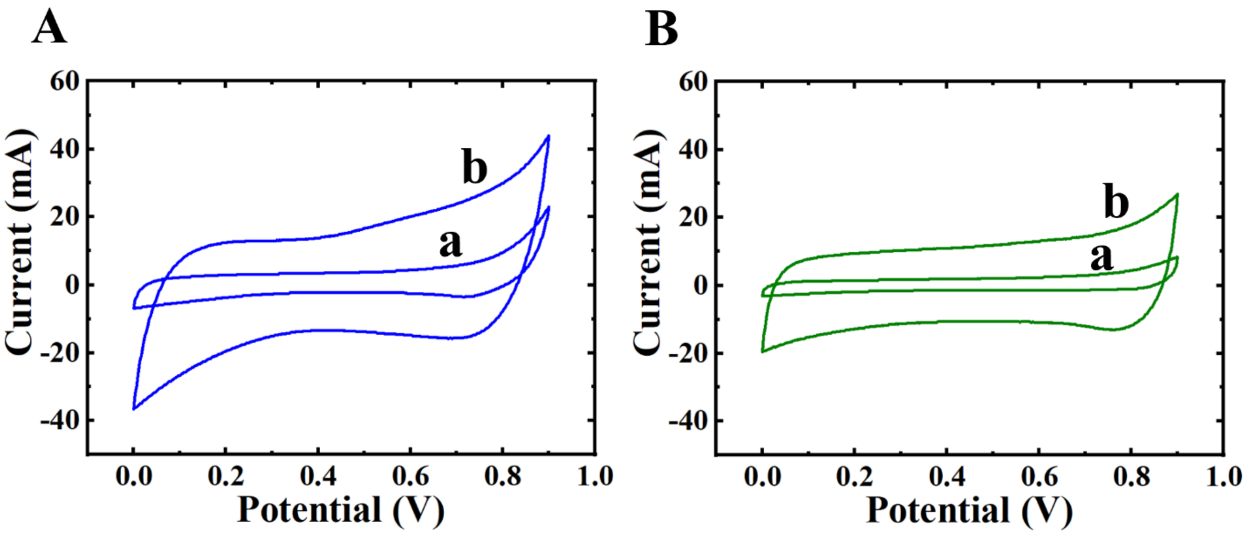

Figure 39. CV curves for **A** E-TDB **B** E-GC at *a* 2 and *b* 20 mV s^{-1}.

For the second portion of this investigation, DHB/TDB (Figure 13A) and GC (Figure 25) were employed as dispersants. Electrodes of 30 mg cm^{-2} mass loading were fabricated from their respective composites (referred to as E-TDB and E-GC for TDB and GC, respectively). As mentioned in the previous sections, TDB forms a Schiff base with DHB which allows the 'bridging' between MnO_2 and MWCNT. However, TDB may also adsorb onto the surfaces of the nanorods since the NH_2 group can form stable by itself chelates with transition metal oxides [104–105].

Electrodes with 30 mg cm^{-2} mass loading were prepared and tested. Figure 39A and Figure 39B show voltammograms at 2 and 20 mV s^{-1} for E-TDB and E-GC, respectively. The size of the voltammogram for E-TDB is larger indicating increased capacitive performance over E-GC. At 2 mV s^{-1} E-TDB possessed a higher capacitance value of about 70 F g^{-1} – twice as much as what is achieved by E-GC (~35 F g^{-1}) for the same scan rate. Figure 40A shows the Nyquist plots constructed from EIS data for E-GC and E-TDB. The slope of the Nyquist plot for E-GC is greater than 45° (even more so than what is achieved by E-TDB) indicating that

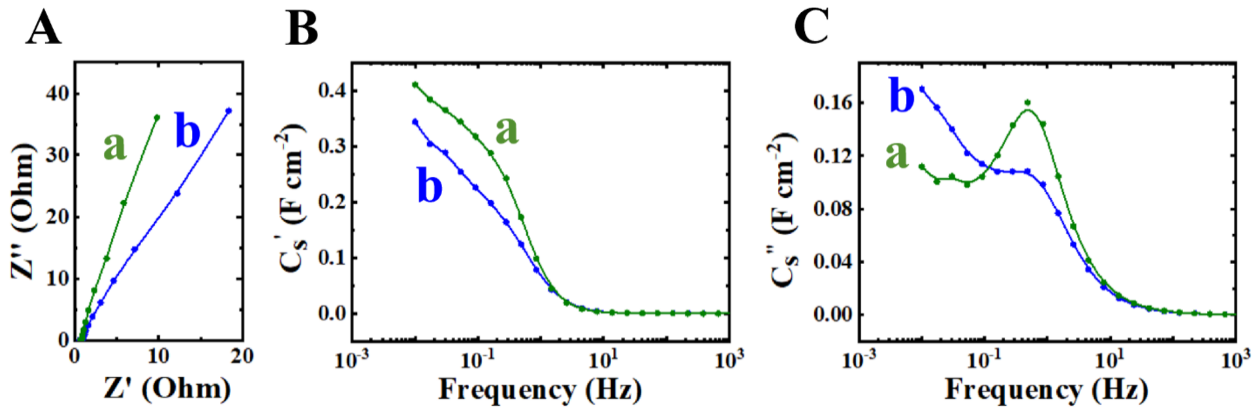

Figure 40. **A** Nyquist plot of complex impedance for *a* E-GC and *b* E-TDB and frequency dependencies of **B** C_s' and **C** C_s'' calculated from the impedance data.

diffusion limitations are not as present. This translates to electrolyte ions readily diffusing in and out of the electrode. Therefore, even at high scan rates the diffusion effects would not (significantly) hamper the capacitive performance, as further proven by the greater retention achieved by E-GC. The real (Figure 40B) and imaginary (Figure 40C) components of complex differential capacitance were obtained from EIS for E-TDB and E-GC. The relaxation frequencies for both electrodes are nearly a full magnitude higher than what was achieved with their MnO_2 nanoparticles counterparts

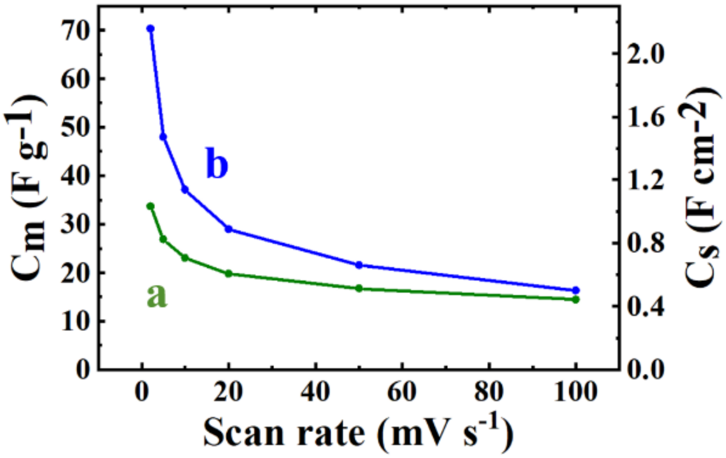

Figure 41. Gravimetric and areal capacitance dependence on scan rate for *a* E-GC and *b* E-TDB.

Figure 41 shows the scan rate dependence of areal and gravimetric capacitance for E-TDB and E-GC. E-TDB clearly achieved a higher capacitance at 2 mV s^{-1} over E-GC. However, its capacitance suffered a large drop as the scan rate was increased yielding a retention of 23%. This was not the case for E-GC; the retention was calculated to be 43%. Since mass transport kinetics dominate at higher scan rates, it may be an indication that the nanorod-CNT structure of E-GC was more porous. This facilitated enhanced diffusion of the electrolyte species within the pores of E-GC, but not as much for E-TDB.

7.5.4 Conclusion

MnO_2 nanorods were synthesized via a hydrothermal method and composited with MWCNTs with the assistance of organic dispersing agents, LG, TDB, and GC. For all electrodes, the maximum value of C_s'' was observed to be shifted more to the right (towards higher frequencies) indicating low time constants. The areal capacitance values at 2 mV s^{-1} for E-LG, E-GC, and E-TDB were 1.1, 0.9 and 2.2 F cm^{-2}, respectively. Although E-LG and E-GC performed poorer at this scan rate than what was achieved by E-TDB their capacitive retention values at 100 mV s^{-1} were twice as high (50% and 43% for E-LG and E-GC, respectively). These numbers are promising, especially since these composites were only a proof-of-concept. This work paves the way to understanding how organic dispersants effect the synthesis of MnO_2 nanorods and their performance in SC applications.

7.6 Capacitive Properties of Polypyrrole Electrodes Prepared by Chemical Polymerization Approach (PPy-MWCNT)

7.6.1 Background

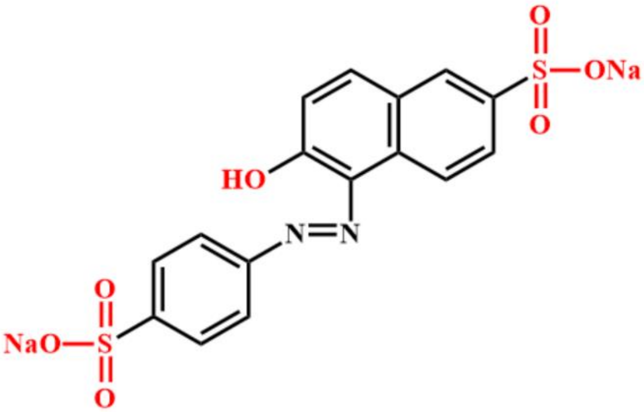

Figure 42. Molecular structure of SY.

There has been growing interest in the use of advanced dopants for PPy polymerization. The size, structure, and charge-to-mass ratio of dopants have a strong relationship with the electrical conductivity of PPy. Certain dopants are also highly influential on the PPy microstructure, voltage window, electrochemical performance, and cyclic stability. Aromatic anionic dopants are a unique class of dopants which can enhance electrical conductivity by improving pyrrole ring orientation [106]. Investigation of these dopants from the chromotropic acid family have shown that a high charge-to-mass ratio allows for smaller particle size, reduced agglomeration, higher capacitance, as well as improved cyclic stability for PPy electrodes [107]. In addition, the use of high-mass, immobile dopants increase the cyclic stability due to their limited intercalation/de-intercalation into the porous structure. Pyrocatechol violet was the choice of MWCNT dispersant and Sunset Yellow (SY) for the PPy dopant. The aromatic rings and the OH^- functional group on SY (Figure 42) can serve to facilitate dispersion of MWCNTs, and its sulfonic groups can participate in the doping of a single pyrrole molecule (Figure 43A) or two different polymer chains (Figure 43B). For the latter case the dopant enhances the interchain mobility of the charge carriers, thereby improving the electrical conductivity of the PPy material [106]. Figure 43C showcases the charge and discharge mechanism of PPy. During discharge the

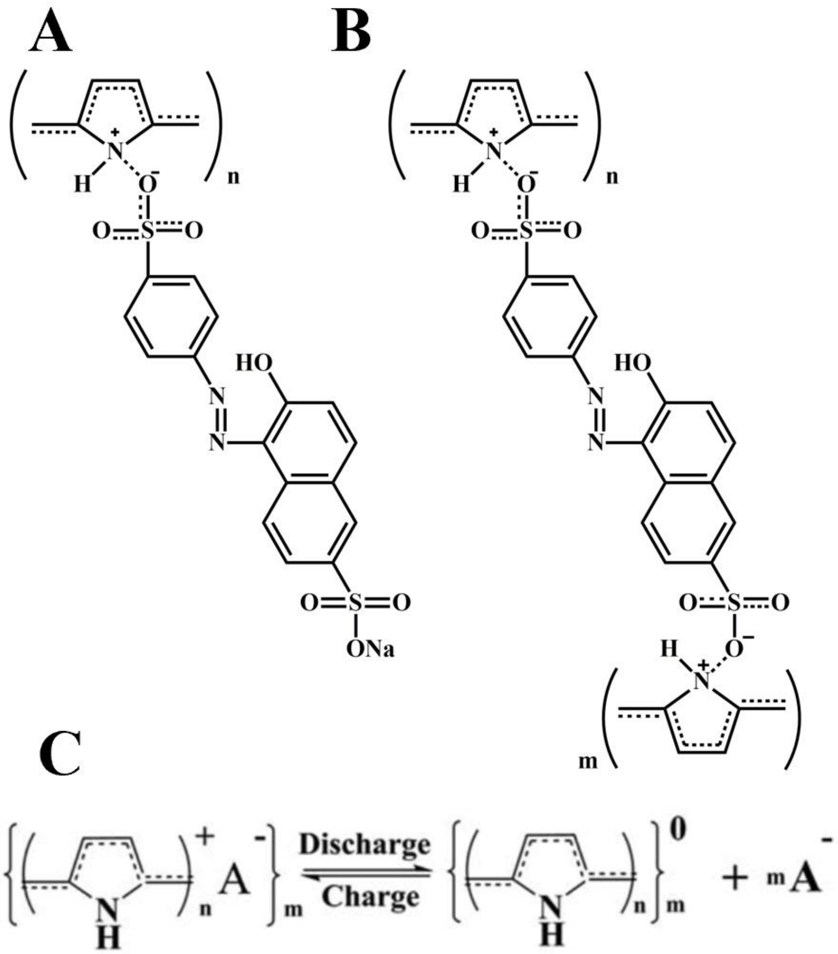

Figure 43. SY doping of PPy in **A** the same chain **B** in different polymer chains, and **C** the charge-discharge mechanism of SY-doped PPy. A = SY and/or SO_4^{2-}.

PPy reduces (is de-doped) to its neutral state by unchaining the incorporated anions A^- (for undoped PPy $A^- = SO_4^2$). SY would also improve the charge storage of PPy since the dopant ions can be released during the reduction phase [108–109] and the anions could migrate back to the polymers during the charge process.

7.6.2 Electrochemical Testing

Three electrodes of identical mass loadings (~35 mg cm^{-2}) were fabricated and tested with the SY-doped PPy-MWCNT composite: (1) the first composite was tested in Na_2SO_4

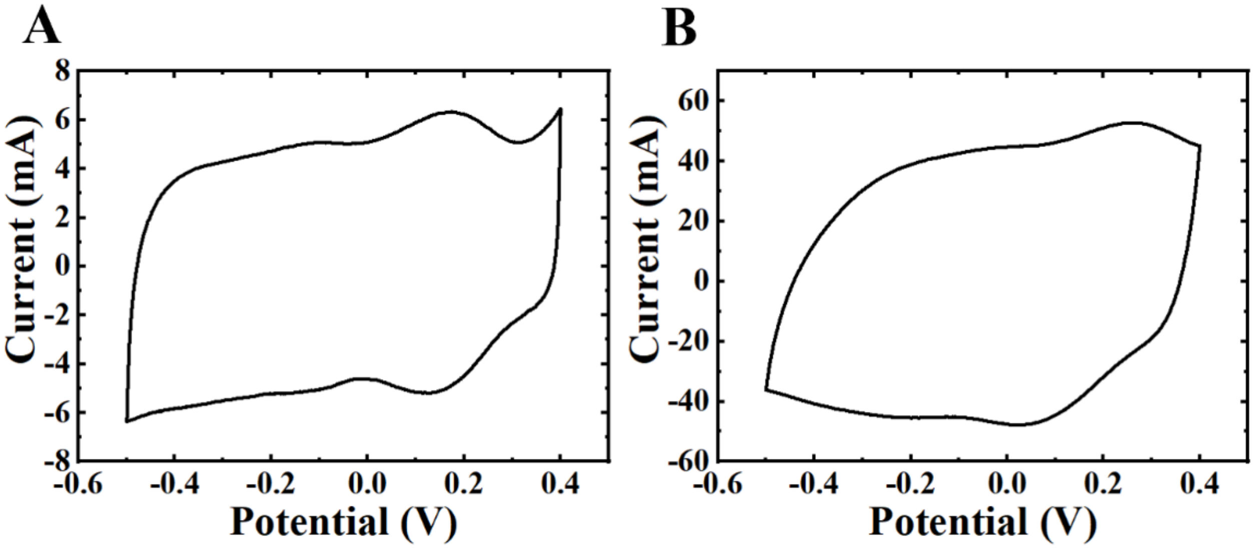

Figure 44. CV curves for E1 at scan rate of **A** 2 mV s^{-1} and **B** 20 mV s^{-1}.

electrolyte; (2) the second composite was tested in $Al_2(SO_4)_3$ electrolyte to study electrolyte effects on this composite; (3) the third composite was also tested in $Al_2(SO_4)_3$ electrolyte but with a shifted voltage window. (These three electrodes are referred to as E1, E2, and E3 henceforth.) Cyclic voltammetry and EIS tests were conducted to gather electrochemical performance data. Figure 44A and Figure 44B show CV curves at 2 and 20 mV s^{-1},

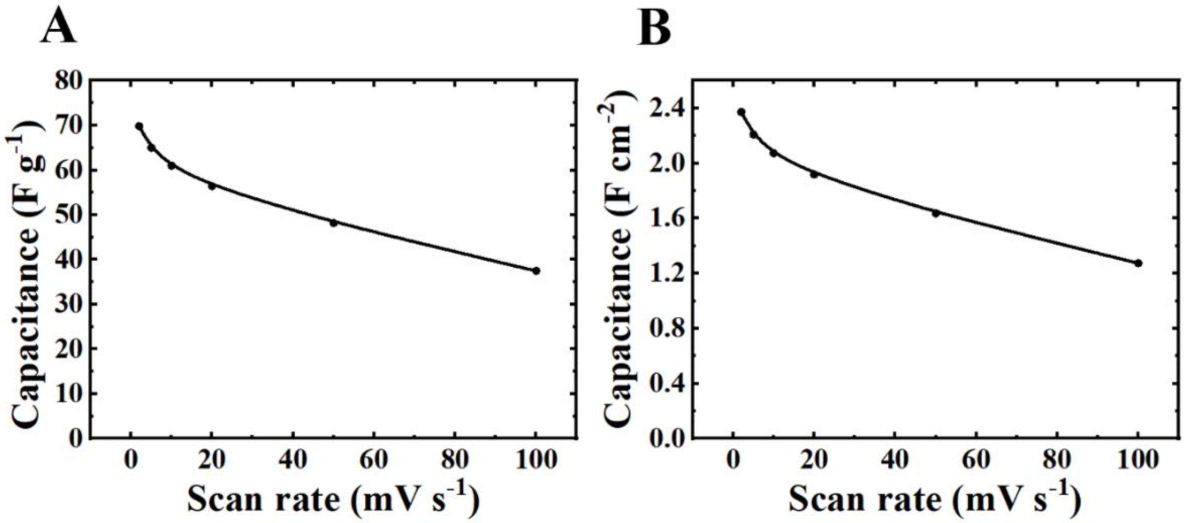

Figure 45. **A** Areal and **B** gravimetric capacitance dependence on scan rate for E1.

respectively, for E1. In Figure 44A, the peaks seen at 0.1 V indicates redox reactions taking place within the composite material. However, these peaks are not as visible in the 20 mV s^{-1} scan (Figure 44B) due to diffusion limitation of the electrolyte species at the increased scan rate.

Figure 45A and Figure 45B shows the gravimetric and areal capacitance dependence on scan rate, respectively. The capacitance was measured to be 2.4 F cm^{-2} (69.8 F g^{-1}) at 2 mV s^{-1} and dropped to 1.3 F cm^{-2} (37.5 F g^{-1}) at 100 mV s^{-1}, yielding a 54% retention.

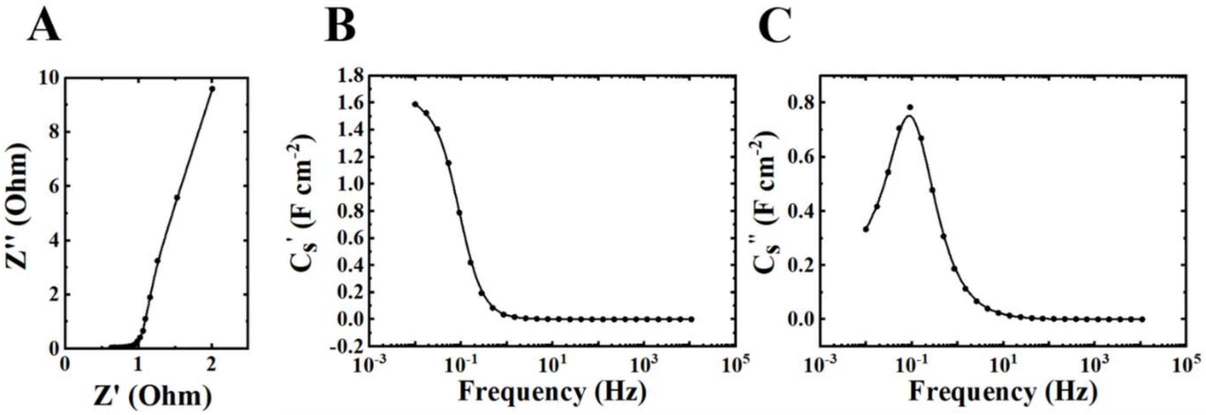

Figure 46. **A** Nyquist plot of complex impedance and frequency dependencies of **B** C's and **C** C"s calculated from the impedance data of E1.

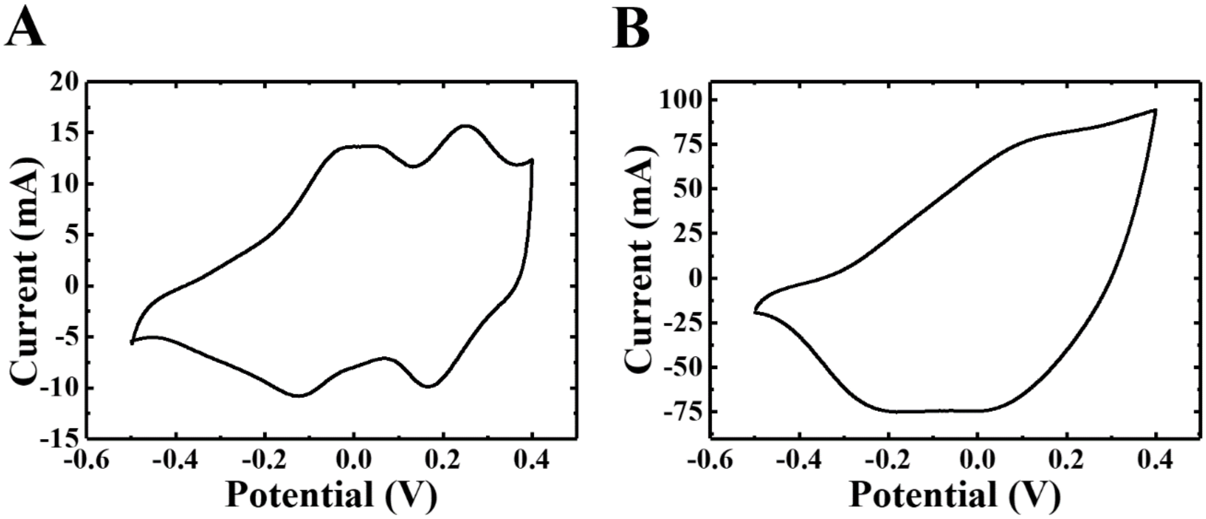

Figure 47. CV curves for E2 at scan rate of **A** 2 mV s^{-1} and **B** 20 mV s^{-1}.

Figure 46A is the Nyquist plot constructed from the impedance data of E1. It shows a deviation away from the ideal 90° slope with a relatively high imaginary component of ~10 ohms. Figure 46B and Figure 46C show the frequency dependencies of the complex capacitance to exhibit relaxation-type dispersion.

Figure 47A and Figure 47B show the CV curves of E2 attained for scan rates 2 and 20 mV s^{-1}, respectively. Redox peaks are observed at -0.2 and 0.2 V (in the discharge portion) indicating increased activity with the composite material and the $Al_2(SO_4)_3$ electrolyte. But again, the peaks are flattened out in the 20 mV s^{-1} scan due to the limited diffusion of the electrolyte species at higher scan rates. In addition, the sharp narrowing of the voltammograms seen at -0.5 V implies that it would be advantageous to shift the voltage window to the right to avoid the narrow region.

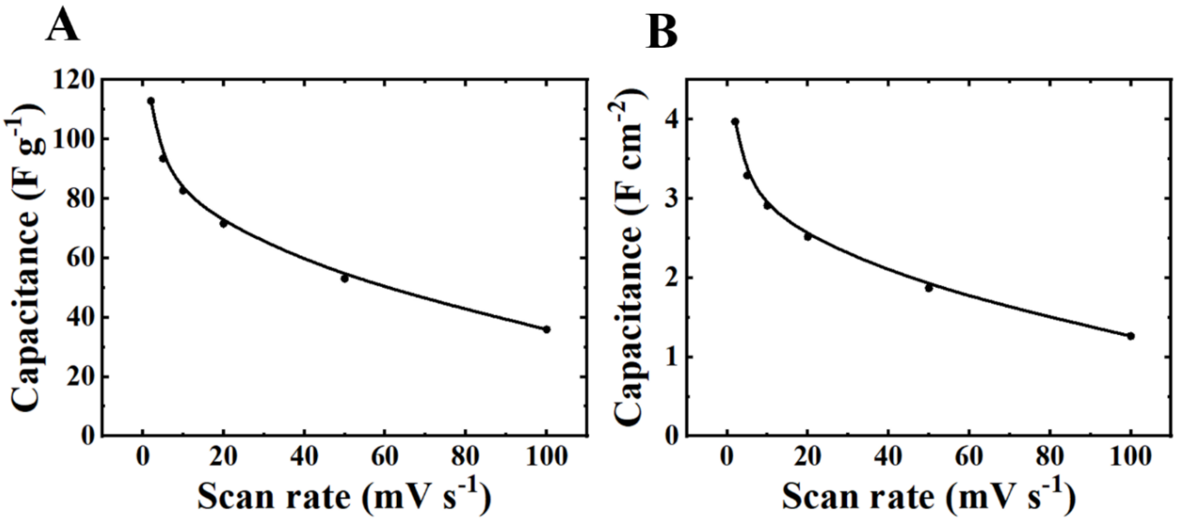

Figure 48. Scan rate dependence on **A** Areal and **B** gravimetric capacitance for E2.

Figure 48A and Figure 48B are the gravimetric and areal capacitance dependences on scan rate, respectively. E2 had poorer capacitive retention at higher scan rates compared to E1 – 32% for E2 versus 54% for E1 at 100 mV s^{-1}. This may be attributed to the larger hydration shell of Al^{3+} ions which may have pronounced mass transfer diffusion limitation at higher scan rates. However, at low scan rates we see that E2 achieved higher capacitance values compared to E1 - 70 F g^{-1} and 2.4 F cm^{-2} for E1 versus 113 F g^{-1} and 4.0 F cm^{-2} for E2 at 2 mV s^{-1}. This could be attributed to the higher charge of the Al^{3+} ions which would have allowed for a stronger electrical force with the potential ramp, and thus greater penetration into the pores of electrode. Thus, the gravimetric and areal capacitance values for – 70 F g^{-1} and 2.4 F cm^{-2} for E1 versus 113 F g^{-1} and 4.0 F cm^{-2} for E2.

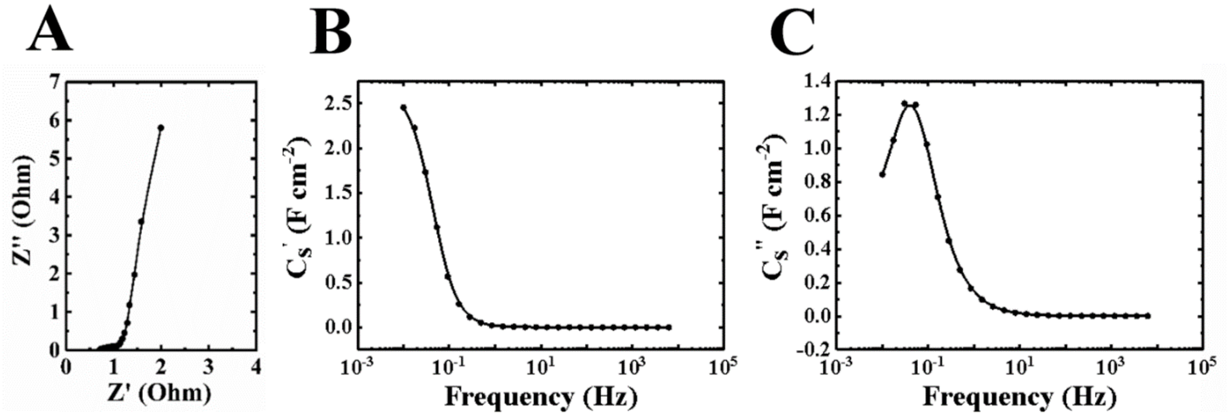

Figure 49. **A** Nyquist plot of complex impedance and frequency dependencies of **B** C's and **C** C"s calculated from the impedance data of E2.

Figure 49A displays the Nyquist plot constructed from the impedance data; it exhibits a slight deviation away from the ideal 90° slope indicating a small level of diffusional resistance. Furthermore, the imaginary component of the impedance is reduced to ~6 ohms. Figure 49B and Figure 49C shows the frequency dependencies of the complex capacitance and it exhibits the typical relaxation-type dispersion. The C_s' and C_s'' values for E2 are recorded to be higher than what was attained with E1– 2.5 and 1.3 F cm^{-2} versus 1.6 and 0.8 F cm^{-2}, respectively. The differences in the electrochemical characteristics for E1 and E2 may be attributed to the differences in the electrolytes. A major difference is the radius of the solvation sphere for the

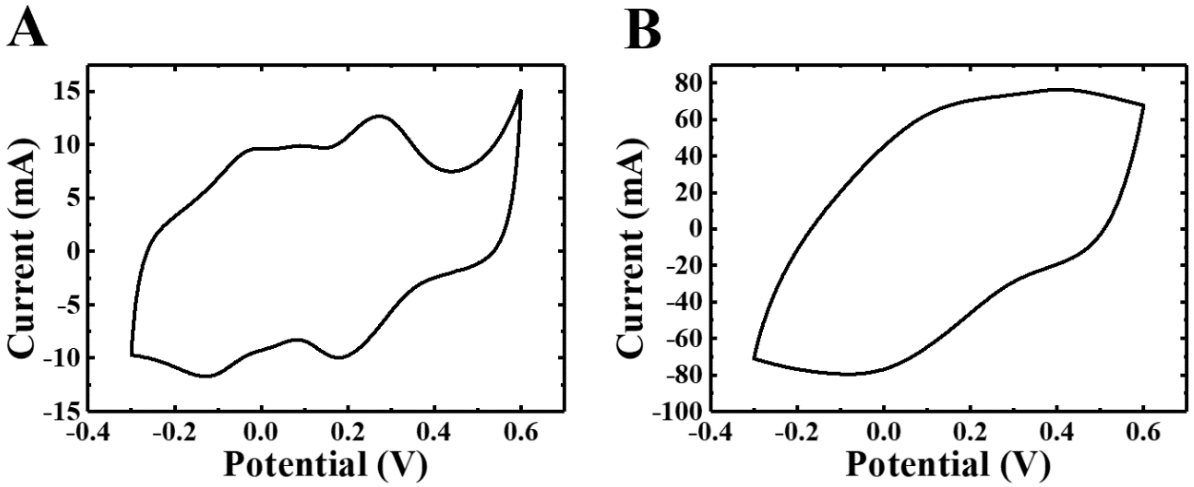

Figure 50. CV curves for E3 at scan rate of **A** 2 mV s^{-1} and **B** 20 mV s^{-1}.

cation species of the electrolyte, which can be correlated to the charge difference between Al^{3+} and Na^{+}. The conductivity and the mobility of the ions are vastly different, as well. These differences would lead to significant changes on how the electrolyte species diffuse in and out of the composite's porous structure at changing frequencies and scan rates.

E3 was also tested in $Al_2(SO_4)_3$ electrolyte, but with a shifted voltage window of -0.3 to +0.6 V instead of -0.5 to +0.4 V. This was done to move away from the sharp redox point seen at -0.5 V in the voltammograms for E2 (Figure 47) and reach higher capacitance values. CV curves

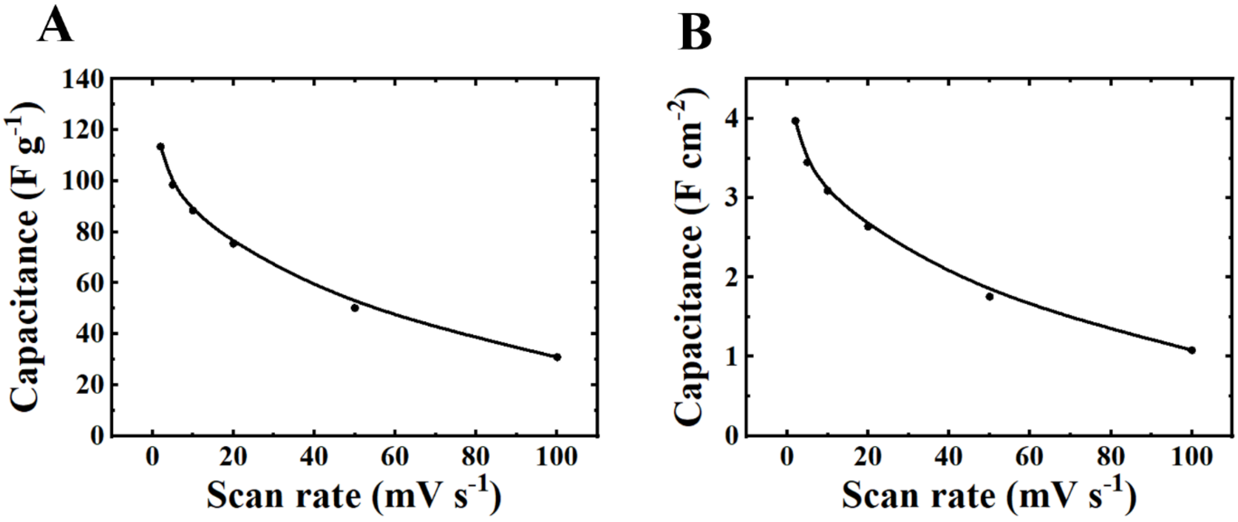

Figure 51. **A** Areal capacitance for E3 and **B** gravimetric capacitance dependence on scan rate.

at 2 and 20 mV s^{-1} for E3 are displayed in Figure 50A and Figure 50B, respectively. Although the redox peak at -0.5 V was eliminated, an unforeseen redox peak was seen at +0.6 V which resulted in the same capacitance values as was seen with E2 – 4 F cm^{-2} (113 F g-1) at a scan rate of 2 mV s.

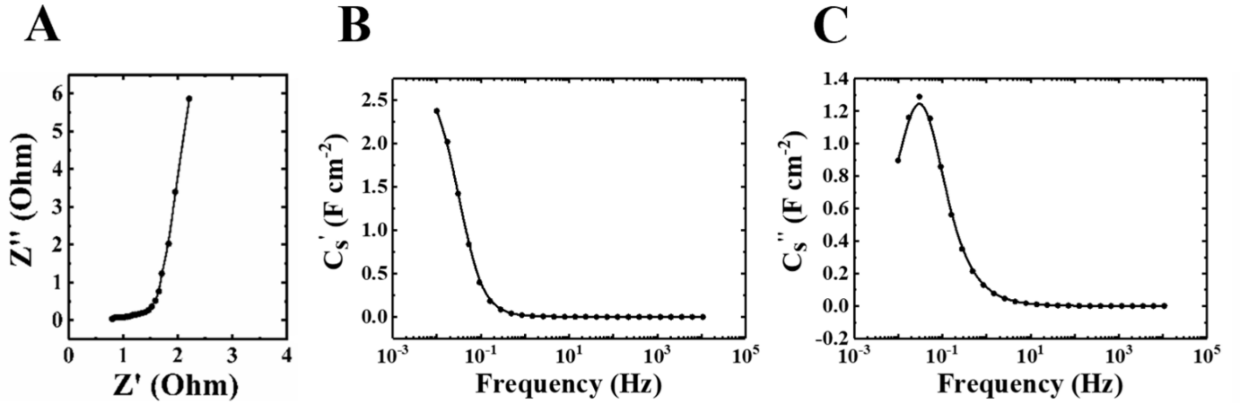

Figure 52. **A** Nyquist plot of complex impedance and frequency dependencies of **B** C_s' and **C** C_s'' calculated from the impedance data of E3.

Plots for the gravimetric and areal capacitance dependence on scan rate are seen in Figure 51A and Figure 51B, respectively. The plots are also nearly identical to what was achieved by E2 in Figure 48.

The Nyquist plot, as well the real and imaginary components of the complex capacitance (Figure 52A, Figure 52B and Figure 52C, respectively) were also nearly identical to the plots recorded for E2.

7.6.3 Conclusion

Three PPy-MWCNT electrodes with 35 mg cm^{-2} mass loading were fabricated using PV as the MWCNT dispersant and SY as the polypyrrole dopant. Employing SY as the polypyrrole dopant for the PPy-MWCNT composite resulted in a retention of 54% and a maximum areal capacitance of 2.4 F cm^{-2} at 2 mV s^{-1}. To study electrolyte effects on this composite the Na_2SO_4 electrolyte was replaced with $Al_2(SO_4)_{3W}$. This resulted in the decrease of the imaginary component of impedance from 10 to 6 ohms, an increase in the maximum areal capacitance from 2.4 to 4 F cm^{-2}, and a decrease in the retention from 54% to 32%. The data collected from this work consolidates the understanding of the molecular structure of dopants and their effect on electrochemical characteristics. The PPy-MWCNT electrodes prepare with SY are promising for future polymer-based SC applications.

8 Conclusions and Future Work

Investigations were conducted with two materials for the development of composites for SC applications. The first material, MnO_2, was used in four approaches: Schiff-base linkage, co-dispersion, LLE, and morphology modification. Various dispersants were used in tandem with each of these approaches, namely: TDB/DHB and FDS/DOPA-HCl for the Schiff-base approach; GC for co-dispersion; UD for LLE; and LG for morphology modification. Each of these techniques avoided the agglomeration problem seen with MnO_2 synthesis because the synthesized MnO_2 particles/nanorod were not dried and re-dispersed into the CNT suspensions to form the respective composites. The dispersants were used to effectively disperse and mix the two constituent materials (MnO_2 and MWCNT) and allow for the fabrication of high mass loading electrodes. Moreover, each of these dispersants demonstrated the provision of relatively high capacitance values and low impedance for the respective electrodes which were fabricated from MnO_2-MWCNT composites. The most unique finding obtained from the MnO_2 segment of this work was the discovery of undecanal to be able to serve as both an extractor and also a receiving solvent for LLE. This simple discovery can enable novel applications in the nanotechnology of not just oxides, but metals, quantum dots, and hydroxides. Furthermore, the work done in the morphology modification technique paved the way to understanding how various organic dispersants interact with the nanorod morphology of MnO_2. For future work, it may be worthwhile to synthesize other morphologies, as this would allow for testing with novel dispersants. This would also aid in understanding what molecular characteristics facilitate enhanced networking of the conducive additive with the MnO_2 morphologies. For example, dispersants with heavier molar masses may allow for effective dispersion of the heavy MnO_2 nanorods while dispersants with lower molar masses may prove ineffective.

The second SC material, PPy, was investigated with the new dopant SY on two different electrolytes. SY was chosen for PPy polymerization because it possessed important molecular characteristics, namely, aromatic rings and sulfonate groups (SY PPY dopant was coupled with PV for the MWCNT dispersant). Electrolyte effects were also studied on the synthesized composites by switching between Na_2SO_4 and $Al_2(SO_4)_3$ electrolytes. $Al_2(SO_4)_3$ electrolyte reduced the capacitive retention by half as compared to Na_2SO_4 electrolyte, but nearly doubled the maximum areal capacitance. The differences in the conductivity and mobility of the electrolyte ions led to significant changes towards how the electrolyte species diffused in and out of the composite's porous structure which yielded different electrochemical performances.

For future work, the next steps would be to fabricate and test fully functional devices with each newly developed composite. This would greatly assist in ascertaining whether the synthesized composites are promising candidates for practical applications. Furthermore, due to the lack of material characterization data it would also be prudent to perform more characterization tests on the synthesized composites. For example, Fourier-transform infrared spectroscopy (FTIR) was not conducted for any of the synthesized composites. This technique would confirm the adsorption of the dispersants onto the respective particles. Therefore, more tests with SEM, TEM, FTIR, and XRD would greatly assist in establishing a groundwork for further comparison of the different colloidal techniques and dispersing agents.

9 References

[1] "Supercapacitor Market by Module Type (Less than 10 Volts Modules, 10-25 Volts Modules, 25-50 Volts Modules, 50-100 Volts Modules, and Above 100 Volts Modules) and Application (Automotive, Industrial, Energy, and Electronics) - Global Opportunities Analysis & Industry Forecast, 2014-2022," *Allied Market Research*. [Online]. Available: https://www.alliedmarketresearch.com/supercapacitor-market.

[2] R. and M. ltd, "Supercapacitor - Global Market Outlook (2017-2026)." [Online]. Available: https://www.researchandmarkets.com/reports/4704074/supercapacitor-global-market-outlook-2017-2026.

[3] M. Huang, F. Li, F. Dong, Y. X. Zhang, and L. L. Zhang, "MnO2-based nanostructures for high-performance supercapacitors," *J. Mater. Chem. A*, vol. 3, no. 43, pp. 21380–21423, Oct. 2015.

[4] Y. Yang, C. Wang, S. Ashraf, and G. G. Wallace, "Polypyrrole doped with redox-active poly(2-methoxyaniline-5-sulfonic acid) for lithium secondary batteries," *RSC Adv.*, vol. 3, no. 16, pp. 5447–5452, Mar. 2013.

[5] Y. Huang *et al.*, "Nanostructured Polypyrrole as a flexible electrode material of supercapacitor," *Nano Energy*, vol. 22, pp. 422–438, Apr. 2016.

[6] "Operation of the Wimhurst Machine." [Online]. Available: http://www.coe.ufrj.br/~acmq/whyhow.html

[7] C. Meng, O. Z Gall, and P. Irazoqui, "A flexible super-capacitive solid-state power supply for miniature implantable medical devices," *Biomed. Microdevices*, vol. 15, pp. 973–983, Jul. 2013.

[8] M. Sharon and M. Sharon, *Carbon Nano Forms and Applications*. McGraw-Hill: New York, Chicago, San Francisco, Lisbon, London, Madrid, Mexico City, Milan, New Delhi, San Juan, Seoul, Singapore, Sydney, Toronto.

[9] B. E. Conway, *Electrochemical Supercapacitors: Scientific Fundamentals and Technological Applications*. Springer US, 1999.

[10] Z. Wu, Y. Zhu, X. Ji, and C. E. Banks, "Transition Metal Oxides as Supercapacitor Materials," in *Nanomaterials in Advanced Batteries and Supercapacitors*, K. I. Ozoemena and S. Chen, Eds. Cham: Springer International Publishing, 2016, pp. 317–344.

[11] S.-C. Pang, M. A. Anderson, and T. W. Chapman, "Novel Electrode Materials for Thin-Film Ultracapacitors: Comparison of Electrochemical Properties of Sol-Gel-Derived and Electrodeposited Manganese Dioxide," *J. Electrochem. Soc.*, vol. 147, no. 2, pp. 444–450, Feb. 2000.

[12] H. Y. Lee and J. B. Goodenough, "Supercapacitor Behavior with KCl Electrolyte," *J. Solid State Chem. Fr.*, vol. 144, pp. 220–223, Apr. 1999.

[13] T. Brousse, M. Toupin, R. Dugas, L. Athouël, O. Crosnier, and D. Bélanger, "Crystalline MnO2 as Possible Alternatives to Amorphous Compounds in Electrochemical Supercapacitors," *J. Electrochem. Soc.*, vol. 153, no. 12, pp. A2171–A2180, Dec. 2006.

[14] S. Devaraj and N. Munichandraiah, "Effect of Crystallographic Structure of MnO $_2$ on Its Electrochemical Capacitance Properties," *J. Phys. Chem. C*, vol. 112, no. 11, pp. 4406–4417, Mar. 2008.

[15] O. Ghodbane, J.-L. Pascal, and F. Favier, "Microstructural effects on charge-storage properties in MnO2-based electrochemical supercapacitors," *ACS Appl. Mater. Interfaces*, vol. 1, no. 5, pp. 1130–1139, May 2009.

[16] M.-S. Wu, "Electrochemical capacitance from manganese oxide nanowire structure synthesized by cyclic voltammetric electrodeposition," *Appl. Phys. Lett.*, vol. 87, no. 15, p. 153102, Oct. 2005.

[17] Z. Pei, M. Xingfa, P. Ding, W. Zhang, Z. Luo, and G. Li, "Study of a QCM Dimethyl Methylphosphonate Sensor Based on a ZnO-Modified Nanowire-Structured Manganese Dioxide Film," *Sensors*, vol. 10, pp. 8275–90, Sep. 2010.

[18] M. Huang *et al.*, "Self-assembly of mesoporous nanotubes assembled from interwoven ultrathin birnessite-type MnO2 nanosheets for asymmetric supercapacitors," *Sci. Rep.*, vol. 4, p. 3878, Jan. 2014.

[19] W. Li *et al.*, "Effect of temperature on the performance of ultrafine MnO2 nanobelt supercapacitors," *J. Mater. Chem. A*, vol. 2, no. 5, pp. 1443–1447, Dec. 2013.

[20] M. Xu, L. Kong, W. Zhou, and H. Li, "Hydrothermal Synthesis and Pseudocapacitance Properties of α-MnO2 Hollow Spheres and Hollow Urchins," *J. Phys. Chem. C*, vol. 111, no. 51, pp. 19141–19147, Dec. 2007.

[21] S. Park, I. Nam, G.-P. Kim, J. W. Han, and J. Yi, "Hybrid MnO2 Film with Agarose Gel for Enhancing the Structural Integrity of Thin Film Supercapacitor Electrodes," *ACS Appl. Mater. Interfaces*, vol. 5, no. 20, pp. 9908–9912, Oct. 2013.

[22] Z. Yu, B. Duong, D. Abbitt, and J. Thomas, "Highly Ordered MnO2 Nanopillars for Enhanced Supercapacitor Performance," *Adv. Mater.*, vol. 25, no. 24, pp. 3302–3306, 2013.

[23] X. Xie, C. Zhang, M.-B. Wu, Y. Tao, W. Lv, and Q.-H. Yang, "Porous MnO2 for use in a high performance supercapacitor: replication of a 3D graphene network as a reactive template," *Chem. Commun.*, vol. 49, no. 94, pp. 11092–11094, Oct. 2013.

[24] A. M. Hashem, H. M. Abuzeid, N. Narayanan, H. Ehrenberg, and C. M. Julien, "Synthesis, structure, magnetic, electrical and electrochemical properties of Al, Cu and Mg doped MnO2," *Mater. Chem. Phys.*, vol. 130, no. 1–2, pp. 33–38, 2011.

[25] Y.-S. Wang, D.-S. Tsai, W.-H. Chung, Y.-S. Syu, and Y.-S. Huang, "Power loss and energy density of the asymmetric ultracapacitor loaded with molybdenum doped manganese oxide," *Electrochimica Acta*, vol. 68, pp. 95–102, Apr. 2012.

[26] R. Poonguzhali, N. Shanmugam, R. Gobi, A. Senthilkumar, R. Shanmugam, and K. Sathishkumar, "Influence of Zn doping on the electrochemical capacitor behavior of MnO2 nanocrystals," *RSC Adv.*, vol. 5, no. 56, pp. 45407–45415, May 2015.

[27] C.-L. Tang *et al.*, "Cobalt-Doped MnO2 Hierarchical Yolk–Shell Spheres with Improved Supercapacitive Performance," *J. Phys. Chem. C*, vol. 119, no. 16, pp. 8465–8471, Apr. 2015.

[28] Y. Li *et al.*, "Hydrothermal deposition of manganese dioxide nanosheets on electrodeposited graphene covered nickel foam as a high-performance electrode for supercapacitors," *J. Power Sources*, vol. 279, pp. 138–145, Apr. 2015.

[29] C. Zhang, F. Meng, and L. Wang, "Controlled synthesis and magnetic properties of bowknot-like CeO2 microstructures by a CTAB-assisted hydrothermal method," *Mater. Lett.*, vol. 119, pp. 1–3, Mar. 2014.

[30] G. Yu *et al.*, "Enhancing the Supercapacitor Performance of Graphene/MnO2 Nanostructured Electrodes by Conductive Wrapping," *Nano Lett.*, vol. 11, no. 10, pp. 4438–4442, Oct. 2011.

[31] Y. Hou, Y. Cheng, T. Hobson, and J. Liu, "Design and Synthesis of Hierarchical MnO2 Nanospheres/Carbon Nanotubes/Conducting Polymer Ternary Composite for High Performance Electrochemical Electrodes," *Nano Lett.*, vol. 10, no. 7, pp. 2727–2733, Jul. 2010.

[32] Q. Meng, K. Cai, Y. Chen, and L. Chen, "Research progress on conducting polymer based supercapacitor electrode materials," *Nano Energy*, vol. 36, pp. 268–285, Jun. 2017.

[33] A. H. Gemeay, H. Nishiyama, S. Kuwabata, and H. Yoneyama, "Chemical Preparation of Manganese Dioxide/Polypyrrole Composites and Their Use as Cathode Active Materials for Rechargeable Lithium Batteries," *J. Electrochem. Soc.*, vol. 142, no. 12, pp. 4190–4195, Dec. 1995.

[34] S. Kuwabata, A. Kishimoto, T. Tanaka, and H. Yoneyama, "Electrochemical Synthesis of Composite Films of Manganese Dioxide and Polypyrrole and Their Properties as an Active Material in Lithium Secondary Batteries," *J. Electrochem. Soc.*, vol. 141, no. 1, pp. 10–15, Jan. 1994.

[35] M. S. Ata and I. Zhitomirsky, "Colloidal methods for the fabrication of carbon nanotube–manganese dioxide and carbon nanotube–polypyrrole composites using bile acids," *J. Colloid Interface Sci.*, vol. 454, no. Complete, pp. 27–34, 2015.

[36] J. Wang, Y. Xu, X. Chen, and X. Sun, "Capacitance properties of single wall carbon nanotube/polypyrrole composite films," *Compos. Sci. Technol.*, vol. 67, no. 14, pp. 2981–2985, 2007.

[37] M. N. Akieh, R.-M. Latonen, S. Lindholm, S. F. Ralph, J. Bobacka, and A. Ivaska, "Electrochemically controlled ion transport across polypyrrole/multi-walled carbon nanotube composite membranes," *Synth. Met.*, vol. 161, no. 17–18, pp. 1906–1914, 2011.

[38] S.-C. Pang and M. A. Anderson, “Novel electrode materials for electrochemical capacitors: Part II. Material characterization of sol-gel-derived and electrodeposited manganese dioxide thin films,” *J. Mater. Res.*, vol. 15, no. 10, pp. 2096–2106, Oct. 2000.

[39] A. Zolfaghari, H. R. Naderi, and H. R. Mortaheb, “Carbon black/manganese dioxide composites synthesized by sonochemistry method for electrochemical supercapacitors,” *J. Electroanal. Chem.*, vol. 697, no. Complete, pp. 60–67, 2013.

[40] D. Zhai *et al.*, “The preparation of graphene decorated with manganese dioxide nanoparticles by electrostatic adsorption for use in supercapacitors,” *Carbon*, vol. 50, no. 14, pp. 5034–5043, 2012.

[41] M. Li, Q. Chen, and H. Zhan, “Ultrathin manganese dioxide nanosheets grown on partially unzipped nitrogen-doped carbon nanotubes for high-performance asymmetric supercapacitors,” *J. Alloys Compd.*, vol. 702, no. Complete, pp. 236–243, 2017.

[42] L. Wang, C. Lin, F. Zhang, and J. Jin, “Phase Transformation Guided Single-Layer β-Co(OH)2 Nanosheets for Pseudocapacitive Electrodes,” *ACS Nano*, vol. 8, no. 4, pp. 3724–3734, Apr. 2014.

[43] E. Raymundo-Piñero, V. Khomenko, E. Frackowiak, and F. Béguin, “Performance of Manganese Oxide/CNTs Composites as Electrode Materials for Electrochemical Capacitors,” *J. Electrochem. Soc.*, vol. 152, no. 1, pp. A229–A235, Jan. 2005.

[44] H. Y. Lee, S. W. Kim, and H. Y. Lee, “Expansion of Active Site Area and Improvement of Kinetic Reversibility in Electrochemical Pseudocapacitor Electrode,” *Electrochem. Solid-State Lett.*, vol. 4, no. 3, pp. A19–A22, Mar. 2001.

[45] E. Kymakis, I. Alexandou, and G. Amaratunga, “Single-Walled Carbon Nanotube-Polymer Composites: Electrical, Optical and Structural Investigation,” *Synth. Met.*, vol. 127, pp. 59–62, Mar. 2002.

[46] Y. Wang, A. Yuan, and X. Wang, “Pseudocapacitive behaviors of nanostructured manganese dioxide/carbon nanotubes composite electrodes in mild aqueous electrolytes: effects of electrolytes and current collectors,” *J. Solid State Electrochem.*, vol. 12, no. 9, pp. 1101–1107, Sep. 2008.

[47] X. Xie and L. Gao, “Characterization of a manganese dioxide/carbon nanotube composite fabricated using an in situ coating method,” *Carbon*, vol. 45, no. 12, pp. 2365–2373, Oct. 2007.

[48] M. O. Danilov and A. V. Melezhyk, “Carbon nanotubes modified with catalyst—Promising material for fuel cells,” *J. Power Sources*, vol. 163, no. 1, pp. 376–381, Dec. 2006.

[49] C. Wallar, D. Luo, R. Poon, and I. Zhitomirsky, “Manganese dioxide–carbon nanotube composite electrodes with high active mass loading for electrochemical supercapacitors,” *J. Mater. Sci.*, vol. 52, no. 7, pp. 3687–3696, Apr. 2017.

[50] Q. M. Yang, V. A. Ettel, J. Babjak, D. K. Charles, and M. A. Mosoiu, “Pasted Ni(OH)[sub 2] Electrodes Using Ni Powders for High-Drain-Rate, Ni-Based Batteries,” *J. Electrochem. Soc.*, vol. 150, no. 4, p. A543, 2003.

[51] C. Portet, P. L. Taberna, P. Simon, and C. Laberty-Robert, "Modification of Al current collector surface by sol–gel deposit for carbon–carbon supercapacitor applications," *Electrochimica Acta*, vol. 49, no. 6, pp. 905–912, Mar. 2004.

[52] J. C. Lytle *et al.*, "The right kind of interior for multifunctional electrode architectures: carbon nanofoam papers with aperiodic submicrometre pore networks interconnected in 3D," *Energy Environ. Sci.*, vol. 4, no. 5, pp. 1913–1925, Apr. 2011.

[53] J. Liu *et al.*, "Co3O4 Nanowire@MnO2 Ultrathin Nanosheet Core/Shell Arrays: A New Class of High-Performance Pseudocapacitive Materials," *Adv. Mater.*, vol. 23, no. 18, pp. 2076–2081, 2011.

[54] J. L. Yin and J. Y. Park, "A nickel foam supported copper core/nickel oxide shell composite for supercapacitor applications," *Microporous Mesoporous Mater.*, vol. 200, no. Complete, pp. 61–67, 2014.

[55] L. Wang, X. Li, T. Guo, X. Yan, and B. K. Tay, "Three-dimensional Ni(OH)2 nanoflakes/graphene/nickel foam electrode with high rate capability for supercapacitor applications," *Int. J. Hydrog. Energy*, vol. 39, no. 15, pp. 7876–7884, 2014.

[56] M. Kundu and L. Liu, "Direct growth of mesoporous MnO2 nanosheet arrays on nickel foam current collectors for high-performance pseudocapacitors," *J. Power Sources*, vol. 243, no. Complete, pp. 676–681, 2013.

[57] J. Li, Q. M. Yang, and I. Zhitomirsky, "Nickel foam-based manganese dioxide–carbon nanotube composite electrodes for electrochemical supercapacitors," *J. Power Sources*, vol. 185, no. 2, pp. 1569–1574, Dec. 2008.

[58] J. Chmiola, C. Largeot, P.-L. Taberna, P. Simon, and Y. Gogotsi, "Monolithic Carbide-Derived Carbon Films for Micro-Supercapacitors," *Science*, vol. 328, no. 5977, pp. 480–483, Apr. 2010.

[59] Y. Gogotsi and P. Simon, "True Performance Metrics in Electrochemical Energy Storage," *Sci. Mag.*, vol. 334, pp. 917–918, Nov. 2011.

[60] C. Zhong, Y. Deng, W. Hu, J. Qiao, L. Zhang, and J. Zhang, "A review of electrolyte materials and compositions for electrochemical supercapacitors," *Chem. Soc. Rev.*, vol. 44, no. 21, pp. 7484–7539, Oct. 2015.

[61] A. G. Pandolfo and A. F. Hollenkamp, "Carbon properties and their role in supercapacitors," *J. Power Sources*, vol. 157, no. 1, pp. 11–27, Jun. 2006.

[62] J. Zhang, *Electrochemical Supercapacitors for Energy Storage and Delivery: Fundamentals and Applications*, 1st ed. 2013.

[63] L. Coury, "Conductance Measurements Part 1: Theory," *Curr. Sep.*, p. 6, 1999.

[64] K. Naoi, S. Ishimoto, J. Miyamoto, and W. Naoi, "Second generation 'nanohybrid supercapacitor': Evolution of capacitive energy storage devices," *Energy Environ. Sci.*, vol. 5, no. 11, pp. 9363–9373, Oct. 2012.

[65] S. Ishimoto, Y. Asakawa, M. Shinya, and K. Naoi, "Degradation Responses of Activated-Carbon-Based EDLCs for Higher Voltage Operation and Their Factors," *J. Electrochem. Soc.*, vol. 156, no. 7, p. A563, 2009.

[66] G. Holland, "Supercapacitor/ Ultracapacitor Strategies 2013-2025," p. 201.

[67] "Here's why Samsung Note 7 phones are catching fire - CNET." [Online]. Available: https://www.cnet.com/news/why-is-samsung-galaxy-note-7-exploding-overheating/.

[68] "Solid-State and Polymer Batteries 2019-2029: Technology, Patents, Forecasts," *IDTechEx*, 16-Oct-2018. [Online]. Available: https://www.idtechex.com/research/reports/solid-state-and-polymer-batteries-2019-2029-technology-patents-forecasts-000641.asp.

[69] N. A. Choudhury, S. Sampath, and A. K. Shukla, "Hydrogel-polymer electrolytes for electrochemical capacitors: an overview," *Energy Environ. Sci.*, vol. 2, no. 1, pp. 55–67, Dec. 2008.

[70] M. Armand, F. Endres, D. R. MacFarlane, H. Ohno, and B. Scrosati, "Ionic-liquid materials for the electrochemical challenges of the future," *Nat. Mater.*, vol. 8, p. 621, Jul. 2009.

[71] C. Arbizzani, M. Biso, D. Cericola, M. Lazzari, F. Soavi, and M. Mastragostino, "Safe, high-energy supercapacitors based on solvent-free ionic liquid electrolytes," *J. Power Sources*, vol. 185, no. 2, pp. 1575–1579, 2008.

[72] B. Weng, R. Shepherd, J. Chen, and G. G. Wallace, "Gemini surfactant doped polypyrrole nanodispersions: an inkjet printable formulation," *J. Mater. Chem.*, vol. 21, no. 6, pp. 1918–1924, Jan. 2011.

[73] C. Wallar, "Colloidal Fabrication of Advanced Oxide Composite Materials for Supercapacitors," McMaster University, Hamilton, Ontario, 2017.

[74] B.-A. Mei, O. Munteshari, J. Lau, B. Dunn, and L. Pilon, "Physical Interpretations of Nyquist Plots for EDLC Electrodes and Devices," *J. Phys. Chem. C*, vol. 122, no. 1, pp. 194–206, Jan. 2018.

[75] "11.6: Imine (Schiff base) formation," *Chemistry LibreTexts*, 02-Oct-2013. [Online]. Available: https://chem.libretexts.org/Bookshelves/Organic_Chemistry/Book%3A_Organic_Chemistry_with_a_Biological_Emphasis_(Soderberg)/11%3A_Nucleophilic_carbonyl_addition_reactions/11.6%3A_Imine_(Schiff_base)_formation

[76] L. Petrone, "Molecular surface chemistry in marine bioadhesion," *Adv. Colloid Interface Sci.*, vol. 195–196, no. Complete, pp. 1–18, 2013.

[77] M. S. Ata, Y. Liu, and I. Zhitomirsky, "A review of new methods of surface chemical modification, dispersion and electrophoretic deposition of metal oxide particles," *RSC Adv.*, vol. 4, no. 43, pp. 22716–22732, 2014.

[78] T. Kar, H. F. Bettinger, S. Scheiner, and A. K. Roy, "Noncovalent π−π Stacking and CH--π Interactions of Aromatics on the Surface of Single-Wall Carbon Nanotubes: An MP2 Study," *J. Phys. Chem. C*, vol. 112, no. 50, pp. 20070–20075, Dec. 2008.

[79] K. Shi and I. Zhitomirsky, "Influence of current collector on capacitive behavior and cycling stability of Tiron doped polypyrrole electrodes," *J. Power Sources*, vol. 240, pp. 42–49, Oct. 2013.

[80] X. Ren and P. G. Pickup, "The origin of the discrepancy between the low frequency AC capacitances and voltammetric capacitances of conducting polymers," *J. Electroanal. Chem.*, vol. 372, no. 1, pp. 289–291, Jul. 1994.

[81] J. Tanguy, N. Mermilliod, and M. Hoclet, "Capacitive Charge and Noncapacitive Charge in Conducting Polymer Electrodes," *J. Electrochem. Soc.*, vol. 134, no. 4, pp. 795–802, Apr. 1987.

[82] B. J. Feldman, P. Burgmayer, and R. W. Murray, "The potential dependence of electrical conductivity and chemical charge storage of poly(pyrrole) films on electrodes," *J. Am. Chem. Soc.*, vol. 107, no. 4, pp. 872–878, Feb. 1985.

[83] M. S. Strano *et al.*, "The role of surfactant adsorption during ultrasonication in the dispersion of single-walled carbon nanotubes," *J. Nanosci. Nanotechnol.*, vol. 3, no. 1–2, pp. 81–86, Apr. 2003.

[84] M. Gubitosi *et al.*, "Characterization of Carbon Nanotube Dispersions in Solutions of Bile Salts and Derivatives Containing Aromatic Substituents," *J. Phys. Chem. B*, vol. 118, no. 4, pp. 1012–1021, Jan. 2014.

[85] W. Cheng and E. Wang, "Size-Dependent Phase Transfer of Gold Nanoparticles from Water into Toluene by Tetraoctylammonium Cations: A Wholly Electrostatic Interaction," *J. Phys. Chem. B*, vol. 108, no. 1, pp. 24–26, Jan. 2004.

[86] H. Yao, O. Momozawa, T. Hamatani, and K. Kimura, "Phase Transfer of Gold Nanoparticles across a Water/Oil Interface by Stoichiometric Ion-Pair Formation on Particle Surfaces," *Bull. Chem. Soc. Jpn.*, vol. 73, no. 12, pp. 2675–2678, Dec. 2000.

[87] T. Zhang, X. Zhao, R. Poon, A. Clifford, R. Mathews, and I. Zhitomirsky, "Synthesis and liquid-liquid extraction of non-agglomerated Al(OH)3 particles for deposition of cellulose matrix composite films," *J. Colloid Interface Sci.*, vol. 508, no. Complete, pp. 49–55, 2017.

[88] N. Gaponik, D. V. Talapin, A. L. Rogach, A. Eychmüller, and H. Weller, "Efficient Phase Transfer of Luminescent Thiol-Capped Nanocrystals: From Water to Nonpolar Organic Solvents," *Nano Lett.*, vol. 2, no. 8, pp. 803–806, Aug. 2002.

[89] R. Tayebee, N. Zamand, A. sadat Hosseini nasr, and M. Kargar Razi, "Theoretical structural study on the adsorption properties of aliphatic aldehydes on ZnO nanoclusters and graphene-like nanosheets systems," *J. Mol. Struct.*, vol. s 1065–1066, pp. 135–142, May 2014.

[90] J. E. Rekoske and M. A. Barteau, "Competition between Acetaldehyde and Crotonaldehyde during Adsorption and Reaction on Anatase and Rutile Titanium Dioxide," *Langmuir*, vol. 15, no. 6, pp. 2061–2070, Mar. 1999.

[91] J. Rasko and J. Kiss, "Adsorption and surface reactions of acetaldehyde on TiO2, CeO2 and Al2O3," *Appl. Catal. Gen.*, vol. 287, no. 2, pp. 252–260, 2005.

[92] K. Huang, M. Lei, R. Zhang, H. J. Yang, and Y. G. Yang, "Low-temperature route to dispersed manganese dioxide nanorods," *Mater. Lett.*, vol. 78, pp. 202–204, 2012.

[93] H.-J. Cui, H.-Z. Huang, M.-L. Fu, B.-L. Yuan, and W. Pearl, "Facile synthesis and catalytic properties of single crystalline β-MnO2 nanorods," *Catal. Commun.*, vol. 12, no. 14, pp. 1339–1343, Aug. 2011.

[94] H.-E. Wang, Z. Lu, D. Qian, S. Fang, and J. Zhang, "Facile synthesis and electrochemical characterization of hierarchical α-MnO2 spheres," *J. Alloys Compd.*, vol. 466, no. 1, pp. 250–257, Oct. 2008.

[95] F. Cheng *et al.*, "Facile Controlled Synthesis of MnO2 Nanostructures of Novel Shapes and Their Application in Batteries," *Inorg. Chem.*, vol. 45, no. 5, pp. 2038–2044, Mar. 2006.

[96] S. Zürcher and T. Graule, "Influence of dispersant structure on the rheological properties of highly-concentrated zirconia dispersions," *J. Eur. Ceram. Soc.*, vol. 25, no. 6, pp. 863–873, Mar. 2005.

[97] T. S. Radoman *et al.*, "Improvement of epoxy resin properties by incorporation of TiO2 nanoparticles surface modified with gallic acid esters," *Mater. Des. 1980-2015*, vol. 62, pp. 158–167, Oct. 2014.

[98] P. Bosch-Jimenez, M. Lira-Cantu, C. Domingo, and J. A. Ayllón, "Solution processable TiO2 nanoparticles capped with lauryl gallate," *Mater. Lett.*, vol. 89, pp. 296–298, 2012.

[99] C. Locatelli, F. B. Filippin-Monteiro, and T. B. Creczynski-Pasa, "Alkyl esters of gallic acid as anticancer agents: A review," *Eur. J. Med. Chem.*, vol. 60, pp. 233–239, Feb. 2013.

[100] S. Ito, Y. Nakagawa, S. Yazawa, Y. Sasaki, and S. Yajima, "Antifungal activity of alkyl gallates against plant pathogenic fungi," *Bioorg. Med. Chem. Lett.*, vol. 24, no. 7, pp. 1812–1814, Apr. 2014.

[101] I. C. Silva *et al.*, "Antibacterial Activity of Alkyl Gallates against Xanthomonas citri subsp. citri," *J. Bacteriol.*, vol. 195, no. 1, pp. 85–94, Jan. 2013.

[102] I. Kubo, N. Masuoka, P. Xiao, and H. Haraguchi, "Antioxidant Activity of Dodecyl Gallate," *J. Agric. Food Chem.*, vol. 50, no. 12, pp. 3533–3539, Jun. 2002.

[103] D. Luo, C. J. Wallar, K. Shi, and I. Zhitomirsky, "Enhanced capacitive performance of MnO2- multiwalled carbon nanotube electrodes, prepared using lauryl gallate dispersant," *Colloids Surf. Physicochem. Eng. Asp.*, vol. 509, pp. 504–511, Nov. 2016.

[104] K. E. Geckeler and K. Volchek, "Removal of Hazardous Substances from Water Using Ultrafiltration in Conjunction with Soluble Polymers," *Environ. Sci. Technol.*, vol. 30, no. 3, pp. 725–734, Feb. 1996.

[105] S. Kobayashi, M. Tokunoh, T. Saegusa, and F. Mashio, "Poly(allylamine). Chelating properties and resins for uranium recovery from seawater," *Macromolecules*, vol. 18, no. 12, pp. 2357–2361, Dec. 1985.

[106] G. R. Mitchell, F. J. Davis, and C. H. Legge, “The effect of dopant molecules on the molecular order of electrically-conducting films of polypyrrole,” *Synth. Met.*, vol. 26, no. 3, pp. 247–257, Nov. 1988.

[107] Y. Zhu and I. Zhitomirsky, “Influence of dopant structure and charge on supercapacitive behavior of polypyrrole electrodes with high mass loading,” *Synth. Met.*, vol. 185–186, no. Complete, pp. 126–132, 2013.

[108] X. Zhang and Bai, “Surface Electric Properties of Polypyrrole in Aqueous Solutions,” *Langmuir*, vol. 19, no. 26, pp. 10703–10709, Dec. 2003.

[109] A. Talaie and G. G. Wallace, “The effect of the counterion on the electrochemical properties of conducting polymers — a study using resistometry,” *Synth. Met.*, vol. 63, no. 2, pp. 83–88, Mar. 1994.